Characterization of impedance and wakefields of accelerator devices in the short bunch limit and beam dynamics effects for the CLIC Damping Rings

Charakterisierung der Impedanz und Wakefields von Teilchenbeschleunigerkomponenten im Regime kurzer Teilchenpakete und Strahldynamikeffekte für die CLIC Dämpfungsringe
Zur Erlangung des akademischen Grades Doktor-Ingenieur (Dr.-Ing.)
genehmigte Dissertation von Andrea Passarelli, M.Sc. aus Neapel / Italien
Tag der Einreichung: 22.01.2019, Tag der Prüfung: 25.03.2019
Darmstadt — D 17

1. Gutachten: Prof. Dr. rer. nat. Oliver Boine-Frankenheim TU Darmstadt
2. Gutachten: Prof. Dr. Ing. Herbert De Gersem TU Darmstadt

TECHNISCHE
UNIVERSITÄT
DARMSTADT

Fachbereich Elektrotechnik
und Informationstechnik
Institut für
Theorie Elektromagnetischer Felder

Characterization of impedance and wakefields of accelerator devices in the short bunch limit and beam dynamics effects for the CLIC Damping Rings
Charakterisierung der Impedanz und Wakefields von Teilchenbeschleunigerkomponenten im Regime kurzer Teilchenpakete und Strahldynamikeffekte für die CLIC Dämpfungsringe

Genehmigte Dissertation von Andrea Passarelli, M.Sc. aus Neapel / Italien

1. Gutachten: Prof. Dr. rer. nat. Oliver Boine-Frankenheim	TU Darmstadt
2. Gutachten: Prof. Dr. Ing. Herbert De Gersem	TU Darmstadt

Tag der Einreichung: 22.01.2019
Tag der Prüfung: 25.03.2019

Darmstadt — D 17

URN: urn:nbn:de:tuda-tuprints-86441
URL: http://tuprints.ulb.tu-darmstadt.de/8644

TECHNISCHE
UNIVERSITÄT
DARMSTADT

Characterization of impedance and wakefields of accelerator devices in the short bunch limit and beam dynamics effects for the CLIC Damping Rings

Dem Fachbereich Elektrotechnik und Informationstechnik
der Technischen Universität Darmstadt

zur Erlangung des akademischen Grades
einer Doktoringenieur (Dr.-Ing.)
vorgelegte Dissertation

von
Andrea Passarelli, M.Sc.
geboren am 07.12.1985 in Neapel

1. Gutachter: Prof. Dr. rer. nat. Oliver Boine-Frankenheim
2. Gutachter: Prof. Dr. Ing. Herbert De Gersem

Tag der Einreichung: 22.01.2019
Tag der mündlichen Prüfung: 25.03.2019

Darmstadt 2019
D17

Erklärung laut Promotionsordnung§9 PromO

§ 8 Abs. 1 lit. c PromO

Ich versichere hiermit, dass die elektronische Version meiner Dissertation mit der schriftlichen Version übereinstimmt.

§ 8 Abs. 1 lit. d PromO

Ich versichere hiermit, dass zu einem vorherigen Zeitpunkt noch keine Promotion versucht wurde. In diesem Fall sind nähere Angaben über Zeitpunkt, Hochschule, Dissertationsthema und Ergebnis dieses Versuchs mitzuteilen.

§ 9 Abs. 1 PromO

Ich versichere hiermit, dass die vorliegende Dissertation selbstständig und nur unter Verwendung der angegebenen Quellen verfasst wurde.

§ 9 Abs. 2 PromO

Die Arbeit hat bisher noch nicht zu Prüfungszwecken gedient.

Darmstadt, den 22.01.2019

Kurzfassung

Der Damping Ring Komplex des Compact LInear Collider (CLIC) soll ultra kleine Emittanzen für die linearen Beschleunigerstrecken produzieren um eine Luminosität von 2×10^{34} cm^2 s^{-1} bei einer Kollisionsenergie von 3 TeV zu erreichen. Aufgrund der hohen Intensität, der kurzen Teilchenpakete und der kleinen Emittanzen wird erwartet, dass Kollektiveffekte die Leistungsfähigkeit der DRs stark beeinträchtigen können und somit die erzielbare Intensität der Positronen- und Elektronenstrahlen limitieren, oder starke Beeinträchtigung der Strahlqualität verursachen. Die Auslegung der Maschine muss schon von Beginn an optimiert werden um zu gewährleisten, dass die Schwellwerte für alle Strahlinstabilitäten mit ausreichend Sicherheitsreserve über der Designintensität liegen. Dafür wird das Impedanzmodell des Damping Ring Komplexes entwickelt und für die Studie der Schwellwerte für Strahlinstabilitäten mit dem Simulationscode PyHEADTAIL verwendet. Zunächst wird ein vereinfachtes Modell der Maschine verwendet, welches dann schrittweise erweitert wird um die Synchrotronstrahlungseffekte und die Impedanz der Vakuumkammern (resistive wall) zu berücksichtigen. Dabei ist es kritisch die Oberflächenimpedanz von dünnen Beschichtungen der Vakuumkammern im Frequenzbereich bis zu mehreren hundert GHz, bis zu denen das Spektrum der Teilchenpakete reicht, richtig zu berücksichtigen. Von speziellem Interesse sind dabei einerseits Non Evaporable Getter (NEG) Beschichtungen die ein kontinuierliches und verteiltes abpumpen ermöglichen, und andererseits amorphous Carbon (a-C) Beschichtungen die verwendet werden um das Bilden von Elektronenwolken in den Vakuumkammern zu unterdrücken.

Der Kern dieser Arbeit besteht in der Entwicklung einer zuverlässigen, praktischen und günstigen Methode für die elektromagnetische Charakterisierung von Beschichtungen im sub-THz Frequenzbereich. Die Methode basiert auf Messungen von elektromagnetischen Wellen, die durch ein Testobjekt bestehend aus einem Wellenleiter und einem auf beiden Seiten mit dem zu untersuchenden Material beschichteten dünnen Plättchen, in der Zeitdomäne. Dies hat folgende Vorteile: homogene Beschichtung mit bekannter Dicke und das Messsystem kann mehrmals verwendet werden um verschiedene Beschichtungsmaterialien zu messen. Die Signalabschwächung durch das Testobjekt ist analytisch berechnet und mit numerischen Simulationen verifiziert. Diese neue Messmethode wird an Plättchen mit NEG-Beschichtung getestet und erlaubt die elektromagnetische Charakterisierung der Oberflächenimpedanz bis hin zu mehreren hundert GHz.

Abstract

The Damping Rings (DRs) complex of the Compact LInear Collider (CLIC) has to provide ultra low emittances to the linear accelerating sections in order to reach a luminosity of 2×10^{34} cm^{2} s^{-1} at the centre of mass energy 3 TeV. Due to the high intensity, short bunches and low transverse emittances, collective effects are expected to seriously affect the performance of the DRs, limiting the electron and positron beam intensity at extraction, or causing an intolerable degradation of the beam quality. The design of the machine has to be optimized already at a very early stage in order to ensure that all the instability thresholds stay above the operational target intensities with sufficient safety margin. To this end, the impedance model of the DRs is developed and used for studying instability thresholds with the PyHEADTAIL code. Starting from a simplified model of the whole machine, the code allows to take into account the radiation damping and quantum excitation effects due to the synchrotron radiation emission and also the resistive wall contribution. The knowledge of the surface impedance up to hundreds of GHz, to which the bunch spectrum extends, is essential for the correct resistive wall impedance modeling of the coatings deposited on the vacuum chambers of the machine. Specifically, Non Evaporable Getter (NEG) is a commonly used coating to allow a distributed and continuous pumping in vacuum chambers and the amorphous Carbon (a-C) is deposited in order to avoid the onset of the Electron Cloud (EC) in the accelerator vacuum chamber.

The core of this thesis consists in the development of a reliable, handy, and inexpensive measurement system for the Electromagnetic Characterization (EMC), in the sub-THz frequency range, of coating materials. The method is based on time domain measurements of an electromagnetic wave passing through a Device Under Test (DUT) made of a waveguide with a thin central slab, where the coating material is deposited on both sides. This device has two main advantages: the deposition homogeneity with predictable thickness and the possibility to reuse the system for further measurements on different coating materials. The assessment of the signal attenuation through the DUT is analytically evaluated and confirmed with numerical simulations. This novel technique is tested on slabs coated with NEG and allows the electromagnetic characterization and the surface impedance evaluation up to hundreds of GHz.

Contents

1 Introduction

1.1 The future colliders

The terascale research on particle interactions is considered the key point for understanding fundamental physical mechanisms, from the electroweak symmetry breaking to the discovery of new possible symmetries, as well as the existence of Dark Matter or in general, to go beyond the Standard Model [1, 2]. The access to terascale physics became reality with LHC experiments. The goal for the next future is to complement the LHC results for having precise measurements of the Higgs boson and potentially new physics discoveries by using a lepton collider in the tera-electron-volt (TeV) energy range [3, 4]. One of the limits of the previous lepton accelerator at CERN, LEP, was the losses due to synchrotron radiation in the bending magnets of the machine. This limitation is avoided in linear colliders. Two opposite linear machines accelerate the particles to their final energy and collide them in a central interaction point. Currently, there are two alternative technologies developed by international collaborations, with significantly different energy reach:

1. The International Linear Collider (ILC) aims to collide beams at an energy of 500 GeV, upgradeable to 1 TeV and it is based on beam acceleration by superconducting RF structures [5, 6].

2. The Compact LInear Collider (CLIC) study is exploring the possibility of extending the energy range of linear colliders into the multi-TeV energy range by developing a novel technology of two-beam acceleration (TBA), providing colliding beams up to 3 TeV [3, 7].

Linear colliders are not the only option for the post-LHC future. The design of a Future Circular Collider (FCC) is another ongoing project. The aim is to build a hadron collider with $80-100$ km circumference and reach 100 TeV.

1.2 The CLIC concept

The Compact Linear Collider (CLIC) is a multi-TeV high-luminosity linear e^+ e^- collider under development at CERN. It is proposed in a staged approach with three centre-of-mass energy stages ranging from a few hundred GeV up to 3 TeV. The first stage is at 380 GeV for providing an accurate model-independent measurements of Higgs couplings to both fermions and bosons [8]. The second stage around 1.5 TeV opens the energy frontier for the discovery of new physics and the third one at 3 TeV further enlarges the CLIC physics potential. New electroweak particles or dark matter are of special interest, as they may be easier to observe at CLIC than at the LHC [7]. This thesis is focused on the 3 TeV design. The layout of this configuration is shown in Fig.1.1.

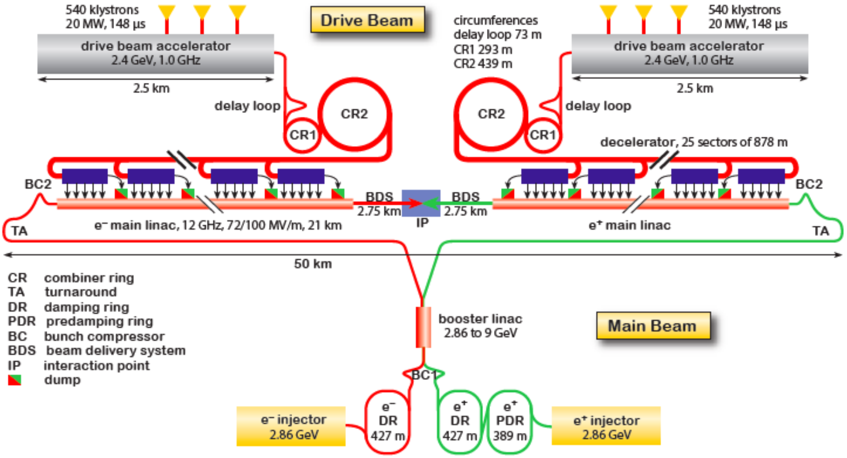

Figure 1.1: CLIC layout at $\sqrt{s}$ = 3TeV.

A laser-driven DC gun provides the polarized electrons for the main beam. A laser-driven RF gun furnishes the primary electrons for positron production. The injector linacs boost the particles up to 2.86 GeV and deflect them into the Damping Rings (DRs) complex. This stage reduces the normalized beam emittances to 500 nm in the horizontal plane and to 5 nm in the vertical one. Furthermore, a common booster linac compresses the beams longitudinally and accelerates them up to 9 GeV. After the beams separation, the turnarounds transport them to the transfer lines. The main linac uses a series of 72 MV/m and 100 MV/m 12 GHz accelerating structures to achieve the final beam energy. The RF power necessary for the main linacs, is generated by the drive beams and then transferred into the main linacs through waveguides. The main beams collide in one Interaction Point (IP) after passing by the Beam Delivery Section (BDS) for a final stage of collimation and focusing. The CLIC parameters at 3 TeV are presented in Table 1.1.

Description	Unit	3 TeV
Repetition frequency	Hz	50
Number of bunches per train		312
Bunch separation	ns	0.5
Beam pulse length	ns	244
Accelerating gradient	MV/m	72/100
Total (peak 1 %) luminosity	$10^{34}cm^{-2}s{-}1$	5.9 (2.0)
Main tunnel length	Km	50.1
Number of particles per bunch	10^{9}	3.7
Bunch length	μm	44
Hor./vert. IP beamsize	nm	40/1
Hor./vert. norm. emitt.	nm	660/20
Estimated Power consumption	MW	589

Table 1.1: CLIC main parameters at 3 TeV.

1.3 The CLIC Damping Rings

The CLIC Damping Rings (DRs) complex aims at bringing the beam emittances down to the values required by the experiments at the highest possible energy and the lowest possible cost.

The main parameter of a collider is the luminosity and it is defined as:

$$L = H_D \frac{N^2}{4\pi\sigma_x\sigma_y} n_b f_r \tag{1.1}$$

where H_D is a factor that takes into account the beam-beam interaction and the change of beta function in the collision region, N is the number of particles per bunch, $\sigma_{x,y}$ are the horizontal and vertical rms beam sizes at the Interaction Point, n_b is the number of bunches per beam and f_r the beam pulse repetition frequency. The beam size is proportional to the emittance and the goal of the DRs is to produce an ultra-low normalized emittances of 500 nm.rad in the horizontal plane and

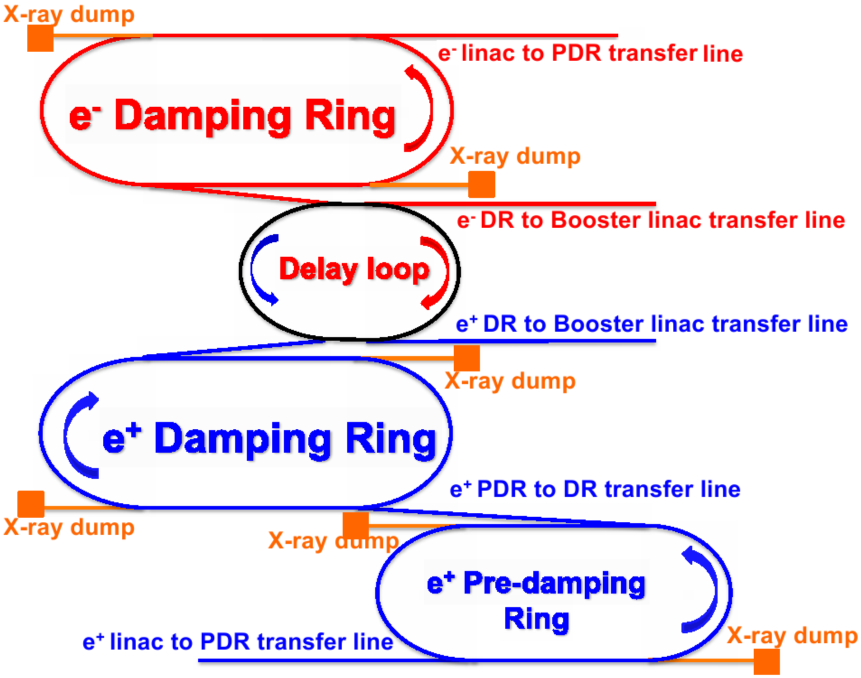

Figure 1.2: The Damping Rings complex.

5 nm.rad in the vertical one with an energy of 2.86 GeV. The DRs complex is shown in Figure 1.2. The large input emittance coming from the positron source requires two stages for the beam damping and therefore a pre-damping ring (PDR) is placed before the main-damping ring. Instead, the progress in the electron sources technologies allow for using of only one stage for the electron ring [9, 10].
The DRs target emittances have been rapidly approached by modern light sources, as can be seen in Figure 1.3.

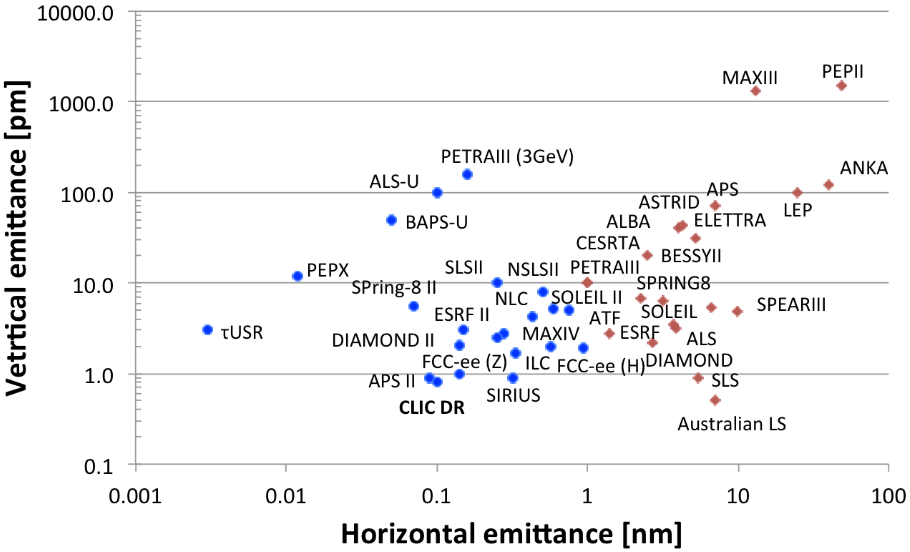

Figure 1.3: Light sources emittance target.

1.4 Overview

The goal of this thesis is to establish the impedance budget of the CLIC damping rings. In particular, the main focus is to develop a new method for the characterization of the coating material in the sub-THz frequency range to improve the impedance modeling of the CLIC DRs components.

Chapter 2 describes the basic theory of synchrotron beam dynamics. It starts with an introduction of linear optics, single particle motion and a short description of the radiation damping and quantum excitation effects. It finishes with the definition of the wake fields, impedance concepts and describes the sources of impedance in the CLIC DRs. Furthermore, the semi-analytical and numerical simulation tools for wakefield and impedance evaluation and a multi-particle tracking suite are detailed.

Chapter 3 contains the studies for the electromagnetic characterization of the coating material in the high frequency range. The characterization is performed using a time domain coherent THz spectrometer. The method is based on the attenuation measurement of the signal passing through a waveguide specifically designed, having a very thin central layer where the coating material is deposited on both sides. The signal attenuation is related to the material conductivity. For this purpose, an analytic model is compared with electromagnetic-field simulation and is used to extrapolate the conductivity of the material from the signal attenuation. The electromagnetic characterization of the Non Evaporable Getter (NEG) coating and the evaluation of its surface impedance is performed up to hundreds of GHz.

Chapter 4 is dedicated to the impedance studies for the CLIC DRs. The transverse impedance is composed of contributions of a broad-band resonator (BBR) and of several resistive wall. The synchrotron radiation damping effect is implemented and the transverse instability threshold behavior is studied for different chromaticity values. In the longitudinal plane, the effect of a BBR and of the synchrotron radiation is also discussed.

The final chapter reports the conclusions of the thesis and the outlook of this study.

2 Beam dynamics and collective effects

This chapter describes the beam dynamics in a lepton (e^+, e^-) circular accelerator, treating both the transverse and longitudinal planes. This includes synchrotron radiation, quantum excitation, wake-fields and impedance with their impact on the beam dynamics through collective effects and describes the sources of impedance in the CLIC DRs. Furthermore, the semi-analytical and numerical simulation tools for wakefield and impedance evaluation and a multi-particle tracking suite are described.

2.1 Transverse and longitudinal single particle dynamics

The motion of particles in circular accelerators is caused by electro-magnetic fields. The transverse single particle dynamics describes the entire system in the ideal case when the particles interact only with the magnetic fields of the magnets but not with the electro-magnetic fields generated by other particles or their interaction with the beam environment. Magnetic dipoles bend the particles to provide complete revolution around the ring and the quadrupole magnets focus the beam so that the particles perform betatron oscillations. While traveling around the ring, ultra-relativistic particles lose energy due to synchrotron radiation. In the longitudinal plane, the energy lost by synchrotron radiation is compensated by a radio-frequency (RF) electric field. The particles longitudinally oscillate and have variations in energy with respect to a reference particle in the center of the bunch. This motion is called synchrotron (longitudinal) oscillations.

The Lorentz force governs the motion of a charged particle in an electromagnetic field $\mathbf{E}$ and $\mathbf{B}$:

$$\frac{d\mathbf{p}}{dt} = \mathbf{F} = e[\mathbf{E} + \mathbf{v} \times \mathbf{B}] \tag{2.1}$$

where $\mathbf{p} = \gamma m \mathbf{v}$ is the momentum, $\mathbf{v} = d\mathbf{r}/dt$ is the velocity, m is the mass, e is the elementary charge and $\gamma = 1/\sqrt{1 - v^2/c^2}$ is the relativistic Lorentz factor [11].

The Frenet-Serret coordinate system $K = (x, y, s)$ is introduced to describe the particle motion around the nominal trajectory. The origin of the coordinate system moves along the beam trajectory. We assume that the particles move parallel to the s-direction $\mathbf{v} = (0, 0, v_s)$ and the magnetic field has only transverse components $\mathbf{B} = (B_x, B_y, 0)$. In the horizontal plane there is a balance between the Lorentz force $F_x = -ev_z B_y$ and the centrifugal force $F_r = mv_s^2/R$ where R is the trajectory curvature radius and m is the particle mass [12, 13]. The balance of the forces leads to:

$$\frac{1}{R(x,y,s)} = \frac{e}{p} B_y(x,y,s) \tag{2.2}$$

Since the beam transverse dimensions are small with respect to the particle trajectory curvature radius, the magnetic field can be expanded in the vicinity of the nominal trajectory. After a multiplication by e/p:

$$\frac{e}{p} B_y(x) = \frac{e}{p} B_{y0} + \frac{e}{p} \frac{dB_y}{dx} x + \frac{1}{2!} \frac{e}{p} \frac{d^2 B_y}{dx^2} x^2 + \ldots = \frac{1}{R} + kx + \frac{1}{2!} m x^2 + \ldots \tag{2.3}$$

The magnetic field is shown as sum of multipoles. The approximation of linear beam optics considers only the two lowest multipoles where $1/R$ corresponds to a constant dipole field providing beam steering and k corresponds to the focusing effect of a quadrupole, for which a magnetic field is provided which is proportional to the transverse displacement from the ideal trajectory. A quadrupole with focusing effect in the horizontal plane is defocusing in the vertical plane. The higher multipoles are either unwanted field errors or introduced for chromatic aberrations or correction of field errors.

2.1.1 Transverse motion

Transverse particle motion around the reference orbit (ideal trajectory fixed by construction) is known as betatron motion. Assuming a particle with a well defined momentum $p = p_0 + \Delta p$, where the momentum deviation Δp is small compared to the nominal momentum p_0, and that the particles are only deflected in the horizontal plane, the magnetic field components are given by:

$$\frac{e}{p_0} B_y = \frac{1}{R} + kx \tag{2.4}$$

and

$$\frac{e}{p_0} B_x = -ky \tag{2.5}$$

The linearized Hill's equation describing the motion of particles in a circular machine is obtained as:

$$x''(s) + \left(\frac{1}{R^2(s)} - k_x(s)\right) x(s) = \frac{1}{R(s)} \frac{\Delta p}{p} \tag{2.6}$$

$$y''(s) + k_y(s) x(s) = 0 \tag{2.7}$$

where $k_{x,y}$ is the quadrupole strength whose sign is chosen arbitrarily. In our case if $k < 0$ the quadrupole is focusing, if $k > 0$ it is defocusing.

The transport of a single particle from a certain point z_0 to another point z can be written in matrix form for linear elements using the general solutions of the homogeneous equations of (2.6) and (2.7):

$$\begin{pmatrix} u(s) \\ u'(s) \end{pmatrix} = M(s|s_0) \begin{pmatrix} u(s_0) \\ u'(s_0) \end{pmatrix} \tag{2.8}$$

where $u(s)$ and $u'(s)$ are either horizontal or vertical position and divergences respectively.

For an off-momentum particle, the solution of the inhomogeneous Eq. (2.6) is a linear superposition of the particular solution and the solution of the homogeneous equation:

$$x = x_\beta(s) + D(s)(\delta p/p_0) \tag{2.9}$$

where $x_\beta(s)$ represents the homogeneous solution of Eq. (2.6), $D(s)$ is named dispersion function and $D(s)(\delta p/p_0)$ is the off-momentum closed orbit.

The transfer matrices in the case of quadrupole and dipole magnets are described in detail in [11]. It is important to note that the transfer matrix can be the product of the transfer matrices in case the particle is passing through any interval made up of sub-intervals. Using these matrices, the linear motion of particles can be tracked through the elements of the accelerator:

$$M(s_2|s_0) = M(s_2|s_1) M(s_1|s_0) \tag{2.10}$$

Applying Floquet's theorem for periodic beam transport sections (like circular accelerators), the solution to the homogeneous Hill's equation can be written as:

$$u(s) = A\omega(s)\cos(\phi(s) - \phi_0) \tag{2.11}$$

where $\omega(s)$ and $\phi(s)$ are periodic functions with a period equal to the circumference of the machine C. Substituting the Eq. (2.11) in Eq. (2.6) and (2.7) we can define the betatron phase advance $\phi(s)$ and the twiss parameters $\alpha(s)$, $\beta(s)$ and $\gamma(s)$. Also the Twiss functions are periodic and are obtained as:

$$\begin{aligned} \alpha(s) &= -\frac{1}{2}\frac{d\beta(s)}{ds} \\ \gamma(s) &= \frac{1+\alpha^2(s)}{\beta(s)} \\ \phi(s) &= \int \frac{ds}{\beta(s)} \end{aligned} \tag{2.12}$$

Generally the transfer matrix M in one period can be expressed as:

$$M_{0\to s} = \begin{pmatrix} \sqrt{\frac{\beta(s)}{\beta_0}}(\cos\phi + \alpha_0 \sin\phi) & \sqrt{\beta(s)\beta_0}\sin\phi \\ \frac{(\alpha_0-\alpha(s))\cos\phi-(1+\alpha_0\alpha(s))\sin\phi}{\sqrt{\beta(s)\beta_0}} & \sqrt{\frac{\beta(s)}{\beta_0}}(\cos\phi - \alpha_0 \sin\phi) \end{pmatrix} \tag{2.13}$$

where α, β and γ are the twiss parameters and $\phi(s) = \int_0^s \frac{ds}{\beta(s)}$ is the phase advance between the positions 0 and s. The evolution of Twiss functions is expressed through:

$$\begin{pmatrix} \beta_s \\ \alpha_s \\ \gamma_s \end{pmatrix} = \begin{pmatrix} M_{11}^2 & -2M_{11}M_{12} & M_{12}^2 \\ -M_{11}M_{21} & M_{11}M_{22}+M_{12}M_{21} & -M_{12}M_{22} \\ M_{21}^2 & -2M_{21}M_{22} & M_{22}^2 \end{pmatrix} \begin{pmatrix} \beta_{s0} \\ \alpha_{s0} \\ \gamma_{s0} \end{pmatrix} \tag{2.14}$$

In the vertical plane similar expressions are valid. In the three planes three independent two-dimensional emittances are defined assuming the ideal case with all the planes fully decoupled.

When the phase advance is equal to 2π, a betatron oscillation is performed. The betatron tune is the number of betatron oscillations in one revolution period and is defined as:

$$Q = \frac{1}{2\pi}\int_0^C \frac{ds}{\beta(s)} \tag{2.15}$$

Emittance

The general solution of the trajectory equation describes the motion of an on-momentum particle in any point of the lattice and it is written for the vertical plane in the form [12]:

$$\begin{aligned} x(s) &= \sqrt{\epsilon_x}\sqrt{\beta_x(s)}\cos(\phi(s)-\phi_0) \\ x''(s) &= -\frac{\sqrt{\epsilon_x}}{\sqrt{\beta_x(s)}}\left[\sin(\phi(s)-\phi_0)+\alpha(s)\cos(\phi(s)-\phi_0)\right] \end{aligned} \tag{2.16}$$

with $\sqrt{\epsilon_x}$ that replaces the amplitude factor A and with $\omega(s) = \sqrt{\beta_x(s)}$ in the equation (2.11). This solution satisfies the equation of an ellipse in the plane $x{-}x'$:

$$\gamma_x x^2 + 2\alpha_x x x' + \beta_x x'^2 = \varepsilon_x \tag{2.17}$$

This expression is called the Courant-Snyder invariant and describes an ellipse with a constant area $\pi\varepsilon_x$, where ε_x is the natural or geometrical “single particle emittance”.

For the entire beam the definition of emittance is statistical. The rms emittance ε_{rms} of the beam is defined as the area (divided by π) of the ellipse containing 39% of the particles. Instead the emittance $\varepsilon_{95\%}$ is defined as the area (divided by π) that contains 95% of the particles. If the distribution of the beam particles in phase space is Gaussian, then $\sqrt{<s^2>} = \sqrt{\beta\varepsilon_{rms}}$ and $\sqrt{6<s^2>} = \sqrt{\beta\varepsilon_{95\%}}$. According to Liouville’s theorem, under the influence of conservative forces, the phase space area enclosed by all particles with a given emittance is constant [14].

Chromaticity

The chromaticity ξ is defined as the ratio between the betatron tune shift ΔQ with respect to the tune Q_0 and the relative momentum deviation Δp with respect to the momentum p_0

$$\frac{\Delta Q}{Q_0} = \xi \frac{\Delta p}{p_0} \tag{2.18}$$

The natural chromaticity is caused by the quadrupole magnets (because the focusing effect of the quadrupole depends on the particle momentum). Chromaticity can be adjusted or corrected by sextupole magnets in regions with non-zero dispersion function.

2.1.2 Longitudinal motion

Radio Frequency (RF) cavities provide the longitudinal electric field to accelerate the particles. The longitudinal RF electric field E_z is applied to the bunched beam and it is expressed as:

$$E_z(t) = E_0 \sin(\phi_{rf}(t) + \phi_s) \tag{2.19}$$

where E_0 is the field amplitude, ϕ_s is the phase angle for a synchronous particle with respect to the RF wave. The synchronous particle has a revolution period T_0 and a momentum p_0 synchronized with the RF wave. This phase is $\phi_{rf} = \omega_{rf} t =$

$h\omega_0 t$, where h is called harmonic number and represents the maximum number of bunches that can be accelerated in the machine. The synchronous particle gains in each turn an amount of energy:

$$\Delta E_s = eV_0 \sin(\phi_s) \tag{2.20}$$

where V_0 is the amplitude of the RF voltage. Non-synchronous particles, with phases $\phi = \phi_s \pm \Delta\phi$, will gain a different amount of energy per turn, equal to:

$$\Delta E_p = eV_0 \sin(\phi) \tag{2.21}$$

The energy gain per turn with respect to the energy gain of the synchronous particle is:

$$(\Delta E)_{\text{turn}} = \Delta E_p - \Delta E_s = eV_0 (\sin\phi - \sin\phi_s) \tag{2.22}$$

Considering slow change of energy with respect to the revolution frequency, the equation of motion for the fractional off-momentum is:

$$\frac{d}{dt}\left(\frac{\Delta p}{p_0}\right) = \frac{\omega_0}{2\pi\beta^2 E_0} eV_0 (\sin\phi - \sin\phi_s) \tag{2.23}$$

where E_0 is the energy of the synchronous particle and β the relativistic factor.

Momentum compaction factor and slip factor

Non-synchronous particles with momentum deviation $\Delta p/p_0$ travel on the dispersion orbit in a different path length than on-momentum particles. The change of the length of the path with respect to the momentum offset is the momentum compaction factor defined as:

$$\alpha_p = \frac{\Delta C/C}{\Delta p/p_0} \tag{2.24}$$

The slippage factor is defined as:

$$\eta \equiv \left(\frac{1}{\gamma^2} - \alpha_p\right) \tag{2.25}$$

The gamma at transition is given by:

$$\gamma_t = \frac{1}{\sqrt{\alpha_p}} \tag{2.26}$$

In machines that work below transition ($\eta < 0$), a particle with higher momentum than the reference particle will have a shorter revolution period and will arrive at a fixed location earlier than the reference particle. Working above transition energy ($\eta > 0$) the behavior is opposite. At $\eta = 0$ the revolution period is independent of the particle's momentum and all particles around the accelerator will travel with equal revolution frequencies.

Like the majority of the electron machines, the CLIC DRs operate above transition with $\gamma \approx 5597$ and $\gamma_t = 1/(1.13 \times 10^{-2}) \approx 88$.

2.2 Synchrotron radiation damping and quantum excitation

When a charged particle is accelerated by an electromagnetic field it will radiate electromagnetic waves. In the general case, the radiation power of an accelerated particle is given by Larmor's formula [12]:

$$P_s = \frac{e^2}{6\pi\varepsilon_0 m_0^2 c^3}\left(\frac{d\mathbf{p}}{dt}\right)^2 \tag{2.27}$$

where e, $\mathbf{p}$ and m_0 are the particle charge, momentum and rest mass; ε_0 is the dielectric permittivity in free space and c is the speed of light. In the case of non-relativistic particles, the emitted radiation may be neglected since it is very weak.

In the case of the CLIC DRs, the particles are ultra-relativistic. In this case, the instantaneous radiated power of this so-called synchrotron radiation is given by Liénard's formula:

$$P_s = \frac{e^2 c}{6\pi\varepsilon_0 (m_0 c^2)^2}\left(\frac{E^4}{\rho}\right) \tag{2.28}$$

The energy radiated, per revolution period from a particle with energy E is:

$$U_0 = \oint P_s dt \equiv \frac{C_\gamma}{2\pi} E^4 I_2 \tag{2.29}$$

where the constant $C_\gamma = \frac{4\pi}{3}\frac{r_0}{(m_0 c^2)^3}$ and I_2 is the second radiation integral $I_2 = \oint \frac{1}{\rho^2} ds$.

The energy lost due to synchrotron radiation reduces the particle momentum in all three planes. The RF field compensate only the energy loss in the longitudinal plane, leading to a damping of the transverse betatron oscillation amplitude.

In general, betatron and synchrotron oscillations are exponentially damped with damping times defined as:

$$\begin{aligned}\tau_x =& \frac{2E_0T_0}{(1-I_4/I_2)U_0}\\ \tau_y =& \frac{2E_0T_0}{U_0}\\ \tau_z =& \frac{2E_0T_0}{(2+I_4/I_2)U_0}\end{aligned} \tag{2.30}$$

where T_0 is the revolution period and $I_4 = \oint \frac{D_x}{\rho}\left(\frac{1}{\rho^2}+2k_1\right)ds$, with D_x the horizontal dispersion and the quadrupole strength $k_1 = \frac{e}{p_0}\frac{\partial B_y}{\partial x}$.

If radiation were a purely classical process, the emittances would damp to a value close to zero. However the radiation is emitted in discrete units (photons), this induces an effect of noise to the beam that increase its emittance. The beam eventually reaches an equilibrium determined by a balance between the radiation damping and the quantum excitation.
The rms equilibrium energy spread in the beam is obtained as:

$$\sigma_{\delta 0}^2 = C_q\gamma^2\frac{I_3}{2I_2+I_4} \tag{2.31}$$

with $C_q = \frac{55}{32\sqrt{2}}\frac{\hbar c}{mc^2}$ and the radiation integral $I_3 = \oint \frac{1}{|\rho^3|}ds$. In circular electron accelerators the bunches are small compared to the bucket area and and thus rms relative energy spread σ_δ and the rms bunch length σ_z [m] are related through:

$$\sigma_{z0} = \sigma_\delta C\sqrt{\frac{\alpha_p E}{2\pi h(aV_0^2-U_0^2)^{1/2}}} \tag{2.32}$$

where α_p is the momentum compaction factor, C is the ring circumference, V_0 is the RF voltage amplitude, h is the harmonic number and U_0 the energy loss per turn defined before.
In the horizontal plane, the equilibrium beam emittance is defined as:

$$\varepsilon_{x0} = C_q\gamma^2\frac{I_5}{I_2-I_4} \tag{2.33}$$

where $I_5 = \oint \frac{\mathcal{H}_x}{|\rho^3|}ds$ with $\mathcal{H}_x = \gamma_x D_x^2 + 2\alpha + xD_xD_{px} + \beta_x D_{px}^2$ is the dispersion invariant in the horizontal plane. Instead, the vertical equilibrium beam emittance is defined as:

$$\varepsilon_{y0} = C_q\gamma^2\frac{\langle \mathcal{H}_y/\left|\rho^3\right|\rangle}{\langle 1/\left|\rho^2\right|\rangle} \tag{2.34}$$

where $\mathcal{H}_y$ is the dispersion invariant in the vertical plane.

2.2.1 Implementation in tracking code

The radiation damping and quantum excitation effect on the beam dynamics in the transverse plane was implemented in the tracking code PyHEADTAIL by resorting on hus formula [15, 16]:

$$u'_{n+1} = u'_n - 2\frac{T_0}{\tau_u}u'_n + 2\sigma_{u'_0}\sqrt{\frac{T_0}{\tau_u}}R \tag{2.35}$$

where n is the turn and the first part of the expression is related to the radiation damping effect and the second one to the quantum excitation effect with τ_u being either the horizontal or the vertical damping time, T_0 is the revolution period. The value $\sigma_{u'_0} = \sqrt{\frac{\varepsilon_{u0}\beta}{\beta_u\gamma}}$ with ε_{u0} is either the horizontal or the vertical equilibrium emittance [m.rad], β_u the average beta function and R is a random number to account for the fluctuations from quantum excitation.
The effect on the longitudinal plane is expressed as momentum spread variation:

$$\left(\frac{\Delta p}{p_0}\right)_{n+1} = \left(\frac{\Delta p}{p_0}\right)_n - 2\frac{T_0}{\tau_s}\left(\frac{\Delta p}{p_0}\right)_n + 2\sigma_\delta\sqrt{\frac{T_0}{\tau_s}}R - \frac{U_0}{m_0c^2\gamma}\beta^2 \tag{2.36}$$

where the first part and the second part of the expression are always related to the radiation damping and quantum excitation effects with τ_s being the longitudinal damping time. The third part of the expression is related to the energy loss, where U_0 is the energy loss per turn expressed in eV and β is the relativistic factor.

2.3 Wake fields and impedance

In this section, we introduce the concept of wake function and beam coupling impedance both in the longitudinal and transverse plane and we also discuss the effect of the wake fields on the beam dynamics.

The particle beam travelling along the accelerator is guided by external electromagnetic fields, but it also electromagnetically interacts with surrounding vacuum chamber. The wake functions are defined in order to describe the interaction between the beam and the surrounding environment. The wake fields allow the description in time domain of the effect of the self-induced fields on the beam and the impedances do the same in frequency domain [17, 18].

This can be illustrated with a simplified model of only two particles: a source particle q_1 and a witness particle q_2. The source particle q_1 travels through an arbitrary device of length L and, by inducing an oscillating field, the witness charge

q_2 at distance z feels a net force (see Fig. 2.1). The integral of this force over the device of length L defines the wake function and its Fourier transform is the device impedance. The velocity of the particles is assumed to be $v = \beta c$, where c is the speed of light and β the relativistic factor [19].

2.3.1 Longitudinal plane

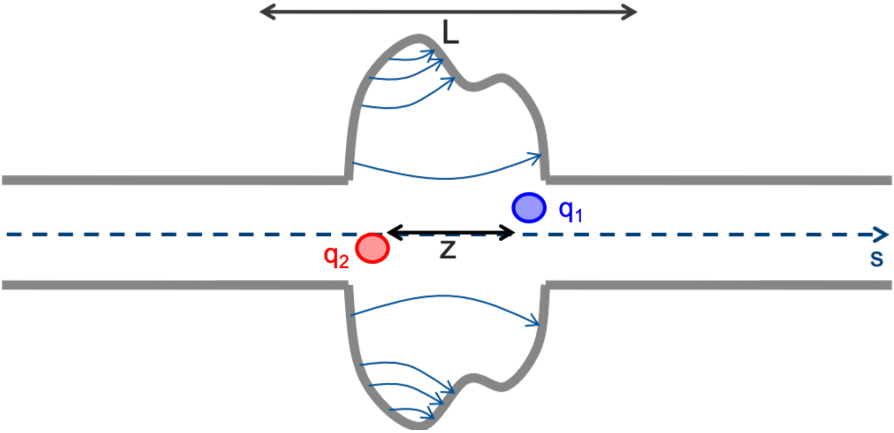

Figure 2.1: Source (q_1) and witness (q_2) particles in a device of arbitrary geometry along the accelerator.

The source particle traveling through an accelerator chamber creates a wake field on the witness particle, situated at a distance z. The longitudinal wake function is defined as the integration along the length L of the Lorentz force on the witness particle q_2, it is written as [20]:

$$W_{\|}(x_2, y_2, x_1, y_1, z)[V/C] = -\frac{1}{q_1 q_2} \int_0^L F_{\|}(x_2, y_2, s, x_1, y_1, z) ds \tag{2.37}$$

where $F_{\|} = qE_s$ is the longitudinal component of Lorentz's force, E_s is the longitudinal component of the electric field induced by the source charge q_1. The transverse offset of source and witness particle with respect to the center of the structure is defined by (x_1, y_1) and (x_2, y_2).

The wake function definition is useful for macroparticle models to describe the driving terms in the single particle equations of motion. The longitudinal beam coupling impedance is defined as follows in the frequency domain [21, 22]:

$$Z_{||}[\Omega] = \int_{-\infty}^{\infty} W_{||}(z) e^{-\frac{j\omega z}{v}} \frac{dz}{v} \tag{2.38}$$

were j is the imaginary unit and $\omega = 2\pi f$ is the angular frequency.

2.3.2 Transverse plane

In structures without top-bottom and/or left-right symmetry or for a symmetric structure but a beam with transverse offset, the source particle induces transverse forces on the witness particle. The transverse wake function is given by:

$$W_{x,y}(x_2, y_2, x_1, y_1, z)[V/C] = -\frac{1}{q_1 q_2} \int_0^L F_{x,y}(x_2, y_2, s, x_1, y_1, z) ds \tag{2.39}$$

where $F_{x,y} = [q(\vec{E} + \vec{v} \times \vec{B})]_{x,y}$ are the transverse components of Lorentz's force. The transverse wake functions can be expanded into a power series in the offset of source and test particle. If we consider only the first order terms and we neglect the coupling between the transverse planes we write:

$$\begin{aligned} W_x &= W_x^{dip} x_1 + W_x^{quad} x_2 \\ W_y &= W_y^{dip} y_1 + W_y^{quad} y_2 \end{aligned} \tag{2.40}$$

where $W_{x,y}^{dip}$ is the horizontal/vertical dipolar (driving) wake function that express the relation to the source offset with respect to the axes of the structure and $W_{x,y}^{quad}$ is the horizontal/vertical quadrupolar (detuning) wake function that express the relation to the witness particle offset. Equation (2.40) is a very good approximation of the transverse wakes for small offsets of both source and test particle.

The transverse beam coupling impedance is defined as the wake function Fourier transform:

$$\begin{aligned} Z_{\perp}^{dip}(\omega)[\Omega/m] &= j \int_{-\infty}^{\infty} W_{\perp}^{dip}(z) e^{-\frac{j\omega z}{v}} \frac{dz}{v} \\ Z_{\perp}^{quad}(\omega)[\Omega/m] &= j \int_{-\infty}^{\infty} W_{\perp}^{quad}(z) e^{-\frac{j\omega z}{v}} \frac{dz}{v} \end{aligned} \tag{2.41}$$

so that:

$$\begin{aligned} Z_x &= Z_x^{dip} x_1 + Z_x^{quad} x_2 \\ Z_y &= Z_y^{dip} y_1 + Z_y^{quad} y_2 \end{aligned} \tag{2.42}$$

The longitudinal and transverse wakes, defined in this chapter, are the responses to a pulse excitation from a single particle: this is the definition of wake function. If the source is a bunch of particles, the resulting wake will be given by the convolution of the wake function with the charge density of the bunch $\lambda(z)$ and is called wake potential. Following the definition of Eq. (2.38), the beam coupling impedance can be evaluated as the ratio of the wake potential Fourier transform and the line density Fourier transform.

2.3.3 Effective impedance

In the following we briefly describe the role of the impedance in the single bunch dynamics. The effective coupling impedance is defined as the sum over the product of the coupling impedance and the normalized spectral density [23, 24]:

$$\left(\frac{Z_{\parallel}}{\omega}\right)_{\text{eff}} = \frac{\sum_{p=-\infty}^{+\infty} \frac{Z_{\parallel}(\omega')}{\omega'} h_l(\omega')}{\sum_{p=-\infty}^{+\infty} h_l(\omega')} \tag{2.43}$$

$$(Z_{\perp})_{\text{eff}} = \frac{\sum_{p=-\infty}^{+\infty} Z_{\perp}(\omega') h_l(\omega' - \omega_{\xi})}{\sum_{p=-\infty}^{+\infty} h_l(\omega' - \omega_{\xi}))} \tag{2.44}$$

where $h_l(\omega)$ is the power spectral density of the mode l, ω_{ξ} is the frequency shift due to the chromaticity effect, defined as $\omega_{\xi} = \frac{\xi \omega_{\beta}}{\eta}$, and $\omega' = p\omega_o + \omega_{\beta} + l\omega_s$, where ω_0 is the revolution angular frequency, ω_{β} the betatron angular frequency, ω_s the synchrotron frequency and l is the azimuthal mode number. In the case of a Gaussian beam the power spectral density is:

$$h_l(\omega) = \left(\frac{\omega\sigma}{c}\right)^{2l} e^{-\frac{\omega^2 \sigma^2}{c^2}} \tag{2.45}$$

where σ is the rms bunch-length.

The effective impedance describes the effect of impedance on beam dynamics and depends on the beam properties. The real and the imaginary parts of $\left(Z_{\parallel}/\omega\right)_{\text{eff}}$ are respectively related to the growth or damping rate and the frequency shift of the mode in consideration. The complex frequency shift can be written as [25]:

$$\Omega^{(l)} - l\omega_s \approx \frac{1}{2\pi} \frac{\Gamma\left(l+\frac{1}{2}\right)}{2^l\,(l-1)!} \frac{N r_0 \eta c^3}{\gamma T_0 \omega_s \sigma^3} i \left(\frac{Z_\parallel}{\omega}\right)_{\text{eff}} \tag{2.46}$$

and:

$$\Omega^{(l)} - \omega_\beta - l\omega_s \approx \frac{1}{4\pi} \frac{\Gamma\left(l+\frac{1}{2}\right)}{2^l l!} \frac{N r_0 c^2}{\gamma T_0 \omega_\beta \sigma} i\,(Z_\perp)_{\text{eff}} \tag{2.47}$$

where N is the number of particles in the bunch, T_0 the revolution period. The above equations show the relation between the imaginary component of the effective impedance and the real coherent tune shift.

2.3.4 Impedance model of a machine

In order to build the impedance model of an accelerator it is necessary to evaluate the impedance (wake) of all the elements and for studying the beam dynamics of the machine, two approaches are possible: in the first one, each wake is separately applied to the beam particles and the beam is transported from one element to the next one with the correct phase advance. Therefore, the impedance model of the machine will contain a database of impedances of the individual accelerator elements but this approach is in general CPU-time-wise unviable. The second approach assumes that all the contributions are a small perturbation to the beam dynamics. Then, all the wakes are summed up and the interaction of the beam with the impedance/wake is then lumped at one location. In this case, the impedance model will contain a global wake/impedance table providing the (weighted) sum of the database elements to be used for beam dynamics. In the longitudinal plane the wake sum is directly used to change the momentum of all the beam particles

$$Z_\parallel(\omega) = \sum_{n=1}^{M} Z_{\parallel n}(\omega) \tag{2.48}$$

In the transverse planes each wake needs to first weighted by the beta function at the location of the wake source and then the weighted sum is divided by an average beta function. The resulting wake is then applied at a location with the average beta function

$$Z_{x,y}(\omega) = \frac{1}{<\beta_{x,y}>} \sum_{n=1}^{M} \left(\beta_{x,y}\right)_n \left(Z_{x,y}\right)_n(\omega) \tag{2.49}$$

The impedance model of an accelerator is important at the early stage of a machine life cycle, to monitor that the global impedance of the machine under design is kept below the budget.

2.4 Impedances and Wake Functions for CLIC DRs model

The total impedance budget of an accelerator is obtained by taking into account all wake fields and impedance sources of vacuum chambers and other machine elements around the machine. The obtained total impedance or the total wake field can then be used in simulations to study the instability thresholds of various collective effects instability mechanisms.

In the case of the CLIC DRs, the task is in fact to optimize the choice of materials and shapes of vacuum chambers and other machine elements such that the instability thresholds are well below the design intensity of the machine.

In general, when the design of the accelerator is not already available and all the elements in the machine are still unknown, the impedance budget of the full machine can be approximated by three main components:

1. A Broad Band Resonator (BBR) to model the global effect of the discontinuities in the beam-pipe and all the devices that exhibit a short-range wakefield.
2. The Resistive Wall (RW) that takes into account the conductivity of the beam pipe of the accelerator.
3. Several narrow band resonators to simulate the effect of objects like cavities. With their long-range wakefield, they may impact the multi-bunch instability thresholds.

In our study, the transverse single bunch instability thresholds are determined by the first two contributions, that are detailed in the following of this section. The effect of the narrow band resonators is not considered because of the complexity to simulate long structure with respect to the wavelength. In the longitudinal plane, is considered the effect of a BBR.

2.4.1 Broad-band resonator

The expression of the transverse wake functions for a broad-band resonator (BBR) are [25]:

$$W_{\perp}(\tau) = \frac{\omega_r^2 R_T}{Q\overline{\omega}_r} e^{\alpha\tau} \sin(\overline{\omega}_r \tau) \tag{2.50}$$

where R_T is the transverse shunt impedance in units of (Ω/m), $\omega_r = 2\pi f_r$ is the cut-off angular frequency of the beam chamber with

$$\overline{\omega}_r = \omega_r \sqrt{1 - \frac{1}{4Q^2}}, \tag{2.51}$$

and

$$\alpha = \frac{\omega}{2Q}. \tag{2.52}$$

The longitudinal wake function is [25]:

$$W_{\|}(\tau) = \begin{cases} 0 & \text{if } z > 0 \\ \alpha R_S & \text{if } z = 0 \\ 2\alpha R_S e^{\alpha\tau}\left(\cos(\overline{\omega}_r \tau) + \dfrac{\alpha}{\overline{\omega}_r}\sin(\overline{\omega}_r \tau)\right) & \text{if } z > 0 \end{cases} \tag{2.53}$$

where R_S is the longitudinal shunt impedance in units of (Ω) and the other parameters are the same as in Eqs. (2.51) and (2.52).

2.4.2 Resistive wall

The "wall" impedances in the case of a cylindrical pipe [26] are:

$$\begin{aligned} Z_{\|}^{\text{wall}} &= \frac{jL\mu_0\omega}{2\pi\beta^2\gamma^2}\alpha_{\text{TM}}(0), \\ Z_x^{\text{wall}} &= \frac{jLZ_0k^2}{4\pi\beta\gamma^4}\left[\alpha_{\text{TM}}(1)x_1 + \alpha_{\text{TM}}(0)x_2\right], \\ Z_y^{\text{wall}} &= \frac{jLZ_0k^2}{4\pi\beta\gamma^4}\left[\alpha_{\text{TM}}(1)y_1 + \alpha_{\text{TM}}(0)y_2\right]. \end{aligned} \tag{2.54}$$

In the case of a flat chamber, the equations are [27]:

$$\begin{aligned} Z_{\|}^{\text{wall}} &= \frac{jL\mu_0\omega}{2\pi\beta^2\gamma^2}\alpha_{00}, \\ Z_x^{\text{wall}} &= \frac{jLZ_0k^2}{4\pi\beta\gamma^4}(\alpha_{02} - \alpha_{00})(x_1 - x_2), \\ Z_y^{\text{wall}} &= \frac{jLZ_0k^2}{4\pi\beta\gamma^4}\left[\frac{2\gamma}{k}\alpha_{01} + 2\alpha_{11}y_1 + (\alpha_{00} + \alpha_{02})y_2\right] \end{aligned} \tag{2.55}$$

where in both cases, L is the length of the element, Z_0 is the characteristic impedance in the free space, β and γ the relativistic factor and $k = \frac{\omega}{\beta c}$. The coefficients α_{mn} and $\alpha_{\mathrm{TM}}(m)$ depend only on the chamber properties and on ω and are detailed in [28]. The transverse offset of source and witness particle with respect to the center of the structure is defined by (x_1, y_1) and (x_2, y_2).

In order to get the wake functions in time domain we need to perform the inverse Fourier transform of the resistive wall impedances. This evaluation is performed by ImpedanceWake2D tool that will be described in Sec. 2.5.

2.5 Simulation tools for impedance and beam dynamics

2.5.1 CST Studio Suite - Dassault Systèmes Simulia

CST Studio Suite by Dassault Systèmes Simulia is a 3D CAD software for the computation of electromagnetic fields. In particular the Wakefield Solver of CST Particle Studio module allows the computation of the wake field and impedance created by a bunch inside a device. The geometrical structure of the device is subdivided into different mesh cells where Maxwell's equations are numerically solved. In this solver, a Gaussian (also different shape for the last release) particle bunch is the source of the EM field inside the device and the trailing particle feels this force. The evaluation of wake potentials as a function of the time delay τ with respect to the passage of the source is performed in time domain and then the beam coupling impedance is calculated in frequency domain by doing the Fourier transform of the wake function and normalizing it to the bunch spectrum. The total number of mesh cells that can be simulated is limited by CPU memory and the processor performance. Therefore, convergence studies by increasing the number of mesh cells are necessary to obtain reliable results. The Frequency Domain solver of CST Microwave Studio module provides the possibility to evaluate the scattering parameters by imposing the mode propagation from a first waveguide port to a second one. This module of the software has been used for the evaluation of the attenuation inside the customized waveguide (see Chapter 3).

2.5.2 The PyHEADTAIL code

PyHEADTAIL [29] is a 6D macroparticle tracking code, written in Python [30]. It is constantly developed and updated by a team of experts and has been benchmarked on real CERN machines for different collective effects [31, 32]. This code is the successor of the well-established HEADTAIL [33] that is written in C. Indeed, in 2013 it was decided to rewrite the HEADTAIL in Python (thus the name PyHEADTAIL) to make it more maintainable, extensible and easier to use also for non-developers.

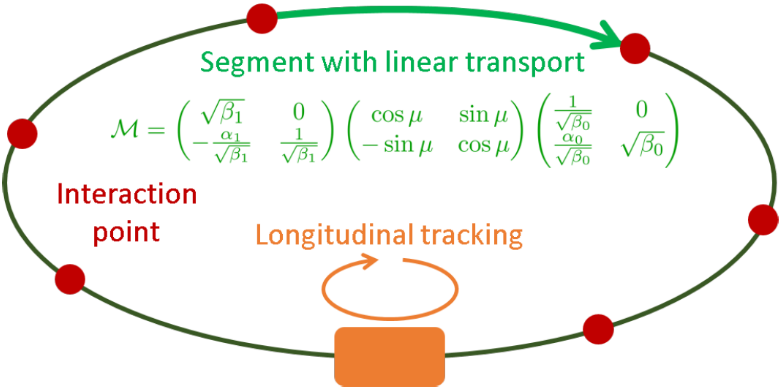

Figure 2.2: Illustration of the numerical model for the simulation of the beam dynamics in a circular accelerator. α and β are the Twiss parameters, μ is the phase advance between the interaction points (red circles).

The goal of the software is to evaluate the beam dynamics of circular particle accelerators in order to model the formation of collective instabilities and to allow the development and consequently, the evaluation of appropriate mitigation techniques to prevent them. Due to the large number of particles in a real bunch (in the order of 10^{11}), PyHEADTAIL represents the bunch as a collection of macro-particles described by a mass, an electric charge, and its generalized coordinates and canonically conjugate momenta with two longitudinal and four transverse dimensions, where each macro-particle represents a certain amount of real physical particles. Typical simulations require between 10^5 and 10^7 macro-particles. The accelerator ring is divided into an arbitrary number of segments. At the beginning and at the end of every segment there is an interaction point where the macro-particles experience collective effects or kicks from a specific accelerator component. Currently the implemented effects at the interaction point are: space-charge, electron-cloud, impedances and damping/feedback systems. The betatron motion between two consecutive interaction points is modeled with linear maps which take into account the Twiss parameters and the dispersion at the start and at the end of the connecting segment as described in this chapter. Non-linear tracking features, such as chromaticity and amplitude detuning, are modeled as a change in the phase advance of each individual macroparticle in the beam. We will consider only the effect of chromaticity. The synchrotron motion is either linear or nonlinear, potentially including particle acceleration and the effects of multiharmonic RF systems. An illustration of the numerical model of the accelerator is shown in Fig. 2.2.

2.5.3 ImpedanceWake2D

The beam coupling impedance can be considered to be composed of two main types: the geometric impedance, due to the geometrical properties of the structure and the resistive-wall impedance. This second contribution is due to the material resistivity properties of the device. ImpedanceWake2D [34] is a code that computes the longitudinal and transverse beam coupling impedances and wake functions in the center of a multilayer axisymmetric or flat structure in the approximation of infinite length in the longitudinal direction [27].

The computation of the beam-coupling impedances and wake functions of a cylindrical multilayer structure is based on Zotter's formalism [35, 36, 37]. For the impedances of a flat structure, the formalism was developed and fully described in [38]. The theories on both the cylindrical and flat cases are summarized in [28]. This code has been used for the evaluation of the resistive wall in the transverse impedance model of the CLIC DRs (see Chapter 4).

3 Electromagnetic characterization of coating materials in the sub-THz region

3.1 Motivation

The use of coating material in modern accelerators and light sources is of fundamental importance in order to avoid undesirable effects on the beam dynamics and to maximize the performance of the machine.

For example, one of the most unwanted effects is an electron cloud; this mechanism starts when photoelectrons, created by the synchrotron radiation photons, hit the beam pipe wall and cause secondary emission or are elastically reflected [39]. The number of electrons grows proportionally to the value of secondary electron yield (SEY) of the surface material. If the SEY is greater than unity the number of electrons grows exponentially and may lead to beam instability and other side effects [40, 41]. Coatings of amorphous carbon (a-C) have been extensively tested [42] and used [43] at the CERN SPS accelerator and in other experiments [44] in order to reduce this SEY.

Another example of coating for the maximization of accelerator performance is their application for achieving ultra-high vacuum in the beam pipe. This reduces the scattering among the beam and gas particles, it reduces the risk of high voltage discharge and improves also the thermal insulation [45]. CERN pioneered NEG thin film coating technology [46], which is nowadays widely used in many other accelerator facilities for a distributed and continuous pumping in vacuum chambers [47].

The electromagnetic characterization (EMC) of coating materials is fundamental to characterize performance limitations of modern particle accelerators and storage rings [48] and to build a reliable impedance model. In fact the surface impedance of the beam pipe depends on the electromagnetic properties of coatings when applied on the inner wall.

This thesis work focuses on the CLIC accelerator and in particular the two damping rings that, with their very short bunches, require a thorough study of the coating surface impedance at very high frequencies (millimeter waves and beyond).

In the radio frequency regime, two different methodologies are used to experimentally estimate the surface impedance: resonant cavity and transmission/reflection measurements [49, 50]. The first one is a very accurate method although it is limited to narrow band and often quite expensive due to the use of customized set of samples in terms of size, shape, etc. [51]. The second technique works in a broadband range and uses coaxial cables or waveguides or free-space, with a frequency band depending on the size of the device and on the available instrumentation. The waveguide method [52] is usually simpler to use with respect to a coaxial cable where sometimes a complicated manufacturing of samples is needed, and does not require electrically large sizes as in the free space case. Waveguides are extensively used up to tens of GHz for electromagnetic characterization of thick (compared to skin depth) or superconducting samples [53, 54].

In the sub-mm-wave and mm-wave regions, the coating material properties are usually determined by using time domain THz reflectometry [55]. The limit of this technique is to allow local measurements only (over a surface determined by the beam size) that becomes cumbersome when large area samples must be investigated. Besides that, in case of multi-layer samples, the intrinsic parameter extraction and from here the impedance value is not so straightforward and is somehow model dependent [56].

THz waveguide spectroscopy is a valid alternative approach for materials that require a strong wave-matter interaction [57]. Until now, this technique has been used to characterize thin samples deposited either on dielectric substrates or directly in the waveguide [58, 59].

Recently, a characterization in the frequency domain of different NEG samples deposited on the lateral walls of a calibrated millimeter waveguide has been carried out by using two port VNA measurements [60, 61]. However, this approach has some relevant drawbacks:

1. the non-homogeneous deposition with unpredictable thickness and relevant peel-off and blistering;
2. the impossibility to reuse the system for further measurements on different coating materials;
3. the difficulty to extend the technique to larger area coating and at higher frequencies.

This thesis work describes a novel measurement method for the EMC of materials used for the coating of accelerator beam pipes, aimed to overcome the inconveniences reported in the previous works. The solution proposed is to put a calibrated waveguide with integrated horn antennas in the optical path of a THz spectrometer and to separate the signal guiding system in two parts: one fixed (a circular or diagonal waveguide with pyramidal horns), and one removable (a thin slab) where the coating is deposited. This choice allows to measure large area coating deposited on metallic plates as in the case of accelerators, where averaged quantities are needed.

In the following the waveguide design and the THz setup are described, as well as the analytical method used for the extraction of the material electromagnetic response, and the measurements performed on high quality NEG samples in order to validate the method. This approach may represent a first step to develop a reliable, handy and inexpensive system for measuring the surface impedance of coating materials in the very high frequency region.

3.2 Method

The proposed method is based on time domain measurements of electromagnetic wave attenuation inside specifically designed waveguides (see Figs. 3.1 and 3.2), with a thin central copper slab where the material under test is deposited on both sides. Two horn antennas are integrated on both sides of each device in order to optimize the signal collection and detection. Each Device Under Test (DUT), described in detail in Sec. 3.2.1, is placed in the optical path of a THz spectrometer, as described in Sec. 3.2.3. The conductivity of the coated material is obtained from the evaluation of the attenuation of the signal transmitted through the device with the coated slab in comparison with a reference signal obtained with an uncoated slab. By knowing the coating thickness from X-ray fluorescence measurements, the surface impedance is then inferred.

It is assumed that the measured electric field signals passing through the device have the following expressions:

$$E_{\mathrm{t}}^{\mathrm{cu}}(f) = K(f)e^{-\alpha^{\mathrm{cu}}(f)} \tag{3.1}$$

$$E_{\mathrm{t}}^{\mathrm{coat}}(f) = K(f)e^{-\alpha^{\mathrm{coat}}(f)} \tag{3.2}$$

where α^{cu} and α^{coat} are the attenuation per unit length for the reference copper slab and the copper slab with coating material respectively and $K(f)$ is the excitation coefficient.

By expressing their ratio in dB:

$$\left[\frac{E_{\mathrm{t}}^{\mathrm{cu}}(f)}{E_{\mathrm{t}}^{\mathrm{coat}}(f)}\right]_{dB} = \left[\alpha^{\mathrm{coat}}(f) - \alpha^{\mathrm{cu}}(f)\right] 20\log_{10} e \tag{3.3}$$

one can retrieve the attenuation given by the coating material only, getting rid of the unknown excitation coefficient. As described later, the result of the measurement is then compared with the analytical evaluation of the mode attenuation in the DUTs. The reliability of the analytical tool is tested by comparing it with numerical simulations performed using a commercial electromagnetic tool (CST Microwave Studio) [62]. The DUTs used for the experiment and the coating process on the slab are described in detail later (see Sec. 3.2.1).

The work presented here focuses on the characterization of the NEG coating. The obtained results will be compared with the one carried out by using a frequency domain approach (on different NEG samples) which utilize Vector Network Analyzer (VNA) two ports measurements of the signal transmitted through a calibrated millimeter waveguide, as explained in detail in [60] and [61].

3.2.1 The Devices Under Test

Three different devices are used for the experiments. The dimensions and the material are reported in Table 3.1. For the pyramidal horns, the maximum and minimum sides along their length are indicated.

Material	Iron	Stainless Steel	Copper
Waveguide	Circular	Diagonal	Diagonal
Length [mm]	42	62	62
Side/radius [mm]	0.9	1.1	1.1
Transition	Pyramidal	Pyramidal	Pyramidal
Length [mm]	39	39	39
Side [mm]	$6 \rightarrow 0.9\sqrt{2}$	$6 \rightarrow 1.1$	$6 \rightarrow 1.1$
Total Length [mm]	120	140	140

Table 3.1: Technical specifications of devices under test.

The shape of the first DUT is shown in Fig. 3.1 and the other two DUTs are shown in Fig. 3.2.

The iron DUT is composed of a circular waveguide connected to two pyramidal horn antennas. The stainless steel and the copper DUTs consist of a diagonal waveguide (square waveguide rotated over 45°) connected to two pyramidal horn antennas with the same length and external aperture size of the first DUT. The horn antennas on all the three devices are used in order to enhance the electromagnetic signal collection and radiation [63]. These geometries have been chosen because of their low mechanical complexity, in terms of milling and drilling. The external

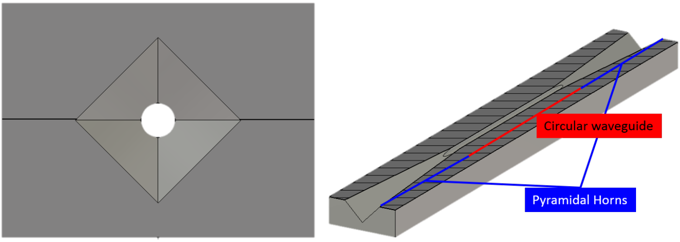

Figure 3.1: DUT: circular waveguide and two pyramidal horns. *Left:* Front view. *Right:* Perspective view of longitudinal cut.

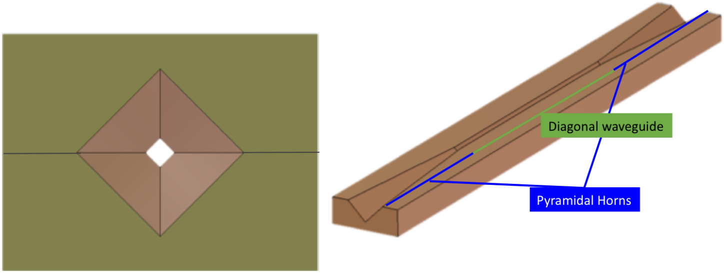

Figure 3.2: DUT: diagonal waveguide and two pyramidal horns. *Left:* Front view. *Right:* Perspective view of longitudinal cut.

shape of the first DUT is a parallelepiped of $16 \times 12 \times 120$ mm^3, the other two devices are 20 mm longer but with the same transverse dimensions.

The coating process of the slabs that are placed in the DUTs is reported in Sec. 3.4.1.

3.2.2 Modes propagating in the DUTs

The analytical model presented in this thesis is built considering the loss contribution given by a single mode propagating inside the DUTs. For the specific case of the Iron DUT, in order to analytically model its horn-to-waveguide transition, we need to locate a plane orthogonal to the longitudinal axis where the pyramidal horn ends and the cylindrical waveguide starts. The distance l_1 of this cross section from the apex of each ellipse is assumed to be two times the distance l_2 to the ellipse cusps (see Fig. 3.3). With this choice the transition contribution to the overall losses can be considered negligible [64].

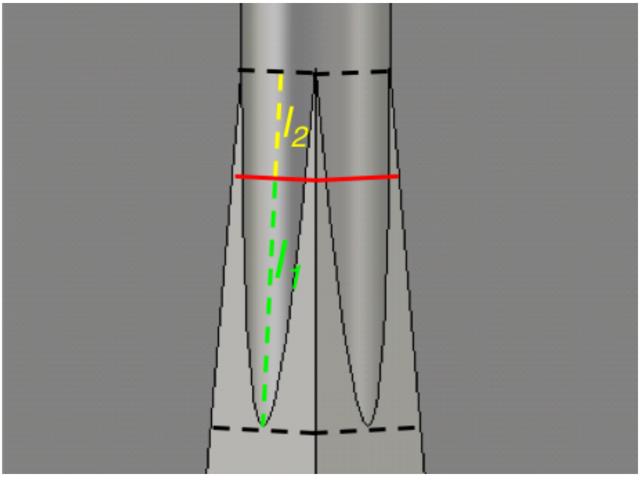

Figure 3.3: Magnified top view of the transition between the pyramidal horn and the cylindrical waveguide. The red line indicates the cross section where the horn antenna ends and the cylindrical waveguide starts in the analytical model. *a* and *b* are the distances of the cross section from the apex and the cusp respectively of each ellipse.

The presence of a slab placed in the median plane together with the incident wave conformation (quasi-plane wave) select the modes that can propagate inside the waveguide and extend the frequency range of a single mode propagation with respect to the case without central slab. In fact, the electric field must be orthogonal and continuous (top-bottom) to the slab surface. Furthermore, left-right symmetries have to be satisfied. In other words this means that the projection of the incident plane wave on the mode must be non-zero.

The first allowed mode in the cylindrical waveguide of the iron DUT is the TE$_{1,1}$ as shown in Fig. 3.4 [65]. In order to evaluate the second mode that propagates inside the waveguide we express the TE modes in cylindrical coordinates $(r,\ \theta)$ as [66]:

$$\begin{aligned}\mathbf{e}^{TE}_{n,m} =& \frac{1}{r}\frac{\sqrt{\varepsilon_n}}{\sqrt{\pi}}\frac{nJ_n\left(\frac{r\chi'_{n,m}}{a}\right)}{J_n\left(\chi'_{n,m}\right)\sqrt{\chi'^2_{n,m}-n^2}}\hat{r}\begin{cases}\sin(n\theta)\\ -\cos(n\theta)\end{cases}\\ &+\frac{\sqrt{\varepsilon_n}}{\sqrt{\pi}}\frac{J'_n\left(\frac{r\chi'_{n,m}}{a}\right)\chi'_{n,m}}{aJ_n\left(\chi'_{n,m}\right)\sqrt{\chi'^2_{n,m}-n^2}}\hat{\theta}\begin{cases}\cos(n\theta)\\ \sin(n\theta)\end{cases}\end{aligned}\tag{3.4}$$

and the TM modes in cylindrical coordinates as:

$$\begin{aligned}\mathbf{e}^{TM}_{n,m} =& -\frac{\sqrt{\varepsilon_n}}{\sqrt{\pi}}\frac{J'_n\left(\frac{r\chi_{n,m}}{a}\right)}{aJ_{n+1}\left(\chi_{n,m}\right)}\hat{r}\begin{cases}\cos(n\theta)\\ \sin(n\theta)\end{cases}\\ &+\frac{1}{r}\frac{\sqrt{\varepsilon_n}}{\sqrt{\pi}}\frac{nJ_n\left(\frac{r\chi_{n,m}}{a}\right)}{J_n\left(\chi_{n,m}\right)\chi_{n,m}}\hat{\theta}\begin{cases}\sin(n\theta)\\ -\cos(n\theta)\end{cases}\end{aligned}\tag{3.5}$$

where a is the radius of the waveguide. J_n and J'_n are the n-order Bessel function and its derivative respectively. The quantity $\chi'_{n,n}$ is the n-th non-vanishing root of the equation:

$$J'_n(x) = 0$$

The incident field is a plane wave, which in cylindrical coordinates is expressed as:

$$\mathbf{E}_{inc} = E_{inc}\sin\theta\ \hat{r} + E_{inc}\cos\theta\ \hat{\theta}\tag{3.6}$$

We project the incident field on the generic mode $\mathbf{e}^{TE}_{n,m}$ and integrate on the surface of the waveguide entrance:

$$\int_0^{2\pi}\int_0^a \mathbf{E}_{inc}\cdot\mathbf{e}^{TE}_{n,m}\, r\, dr\, d\theta\tag{3.7}$$

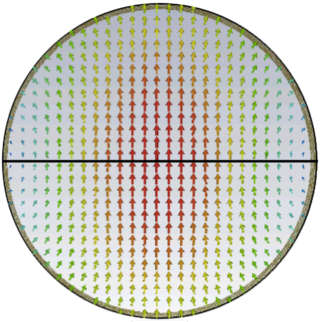

Figure 3.4: First mode propagating inside the cylindrical waveguide with a slab placed in the center.

This integral is non-zero only in the case of $n = 1$. For the TM mode, the projection is:

$$\int_0^{2\pi}\int_0^a \mathbf{E}_{inc}\cdot\mathbf{e}_{n,m}^{TM}\, r\, dr\, d\theta \tag{3.8}$$

In the specific case, when $n = 1$, the integral is:

$$\int_0^{2\pi}\int_0^a \mathbf{E}_{inc}\cdot\mathbf{e}_{1,m}^{TM}\, r\, dr\, d\theta = -E_{inc}\frac{\sqrt{2\pi}}{J_2\left(\chi_{1,m}\right)}\frac{1}{a}\int_0^a J_0\left(\frac{r\chi_{1,m}}{a}\right) r\, dr = 0 \tag{3.9}$$

and no TM modes can propagate inside the device. After this evaluation we can assert that the second mode propagating inside the circular waveguide with a central slab placed in the center is the TE$_{1,2}$. Therefore, the allowed bandwidth for the first mode propagation only is defined by the cut-off frequencies of $f_{\mathrm{TE}_{1,1}} = 97.6$ GHz and $f_{\mathrm{TE}_{1,2}} = 282.6$ GHz for the waveguide with radius 0.9 mm.

The model of the complete DUT has also to take into account the presence of the two integrated antennas for signal collection and detection. Since the semi-aperture of each pyramidal horn is $< 5^\circ$ we may consider the modes as they propagate in a locally uniform square waveguide and take the relevant lower modes. The first two modes, having the same cut-off frequency, are two degenerate modes. If their excitation coefficient has the same amplitude, their sum will exhibit an electric field everywhere orthogonal to the horizontal diagonal, where we are going to put the slab, as shown in Fig. 3.5.

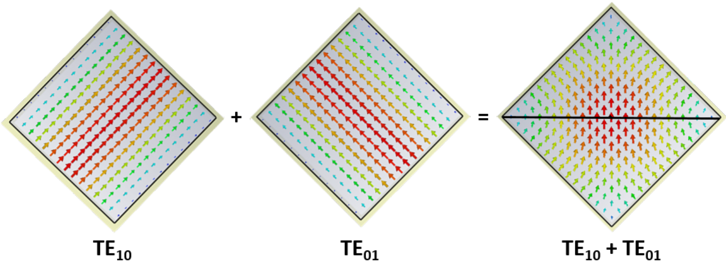

Figure 3.5: Electric field of the first two degenerate modes inside a square waveguide and sum (right) of the first two modes propagating when a slab is placed in the center.

Doing the same considerations we did for the cylindrical iron waveguide and considering a minimum side of $0.9\sqrt{2}$ mm (see Table 3.1), the first two modes allowed to pass have a cut off frequency of $f_{\mathrm{TE}_{1,0}} = f_{\mathrm{TE}_{0,1}} = 117.8$ GHz. The other two modes allowed to pass start their propagation from $f_{\mathrm{TE}_{2,1}} = f_{\mathrm{TE}_{1,2}} = 263.3$ GHz.

Therefore, taking into account the propagation in both the transitions and the circular waveguide, the overall usable frequency window for a single mode propagating inside the iron DUT ranges from 118 GHz to 283 GHz.

Regarding the other two DUTs, we have to study the single mode propagation inside the diagonal waveguide and the two pyramidal transitions. As we said before, the first mode that can propagate inside these DUTs, with a central slab posed in it, is the sum of the $TE_{1,0}$ and $TE_{0,1}$ and the second mode that respects the boundary conditions and the symmetry is the sum of $TE_{2,1}$ and $TE_{1,2}$.
For the stainless steel and the copper DUTs, with an internal side of the diagonal waveguide of 1.1 mm, the usable frequency window for a single mode propagation ranges from 135 GHz to 300 GHz. A summary of the usable frequency ranges for the different DUTs is in 3.2.

DUT	Iron	Stainless Steel	Copper
Frequency window [GHz]	$118-283$	$135-300$	$135-300$

Table 3.2: First mode propagation frequency window inside the DUTs.

3.2.3 Sub-THz system

Sub-THz measurements are carried out using a Time Domain Spectrometer (TDS) operating in transmission mode. The setup is based on a commercial THz-TDS system (TERA K15 by MENLO systems) customized for the waveguide characterization. The system is driven by a femtosecond fiber laser @1560 nm with an optical power of < 100 mW and a pulse duration < 90 fs. In the standard configuration, the laser output splits into two beams in pump-probe mode. Fiber-coupled photoconductive antenna modules are utilized for both electric field signal emission and detection. A fast opto-mechanical line with a maximum scanning range of approximately 300 ps is used to control the time delay between the pump and the probe beam. Signal detection is performed by a lock-in amplifier that drives the pulse generation at about 90 KHz and integrate the output voltage over an interval of 100 ms. Pulse waveforms are sampled by 2048 data-points in 150 fs intervals of optical delay (step size $\sim 30\ \mu$m). Each scan requires about 10 min of measurement time.

The THz TDS system has a set of symmetric optics with respect to the center line between the transmitter and the receiver. In particular, TPX (polymethylpentene) lenses are used to collimate the short $(1 - 2$ ps) linearly polarized pulse on the waveguide. This results in a Gaussian-like beam with a waist of approximately 8 mm and a quasi-plane wave phase front. The coupling efficiency between the free space signal and the input and output horns is then mechanically optimized by maximizing the signal transmitted through the DUT. A sketch of the optical configuration is shown in Fig. 3.6.

For an accurate control over the target positioning, the waveguide is placed on a kinematic mount coupled with a micrometric goniometer. The base part of the waveguide is fixed onto the kinematic mount and the metal slabs are replaced by removing the top part of the waveguide structure only. To minimize any possible optical gap in between the top and the base plate, the waveguide is firmly tightened with a rigid clamp. To block any unwanted THz radiation from the emitter antenna, the area around the waveguide entrance is shielded with a metal sheet with an extrude cut at the center. Fig. 3.7 shows the THz time domain signals obtained in free space and in the DUT, with the input beam polarized parallel to the waveguide slab. In the latter case, the ps-scale input pulse is broadened to more than 50 ps and strongly reshaped by the reflections inside the waveguide. The stretching of the transmitted signal, compared with the free space input pulse, is due to the strongly dispersive character of the waveguide, that acts as a delay line [67].

Frequency dependent transmission curves are obtained through the application of a standard Fast Fourier Transform (FFT) algorithm. In the experiment, the max-

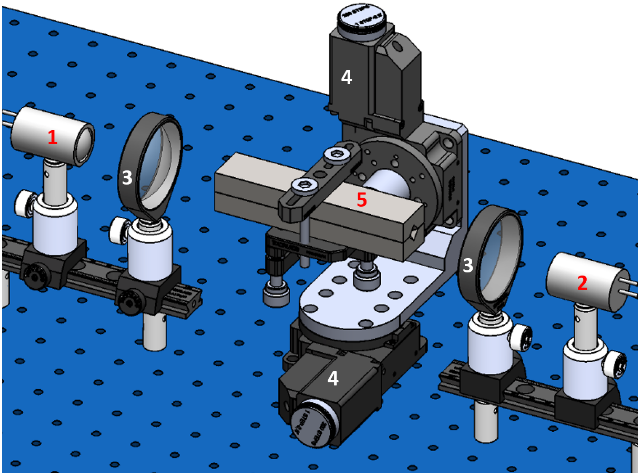

Figure 3.6: Sketch of the opto-mechanical setup utilized for the measurements: 1) Emitter, 2) Detector, 3) TPX collimating lenses, 4) Micrometric alignment systems, 5) DUT (waveguide).

imum frequency resolution is about 4 GHz, limited by the scanning range of the delay line only. The picture of the Sub-THz system with the DUT placed in the optical path is shown in Fig. 3.8.

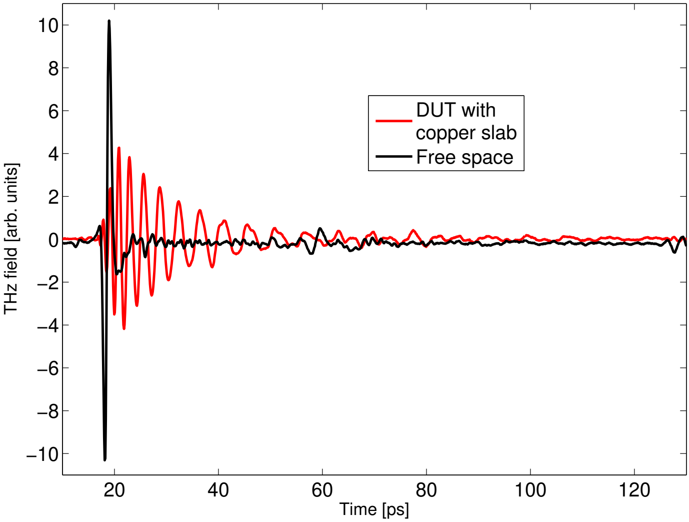

Figure 3.7: THz time domain signal propagation in free space (black curve) and in the DUT with a copper slab without coating (red curve).

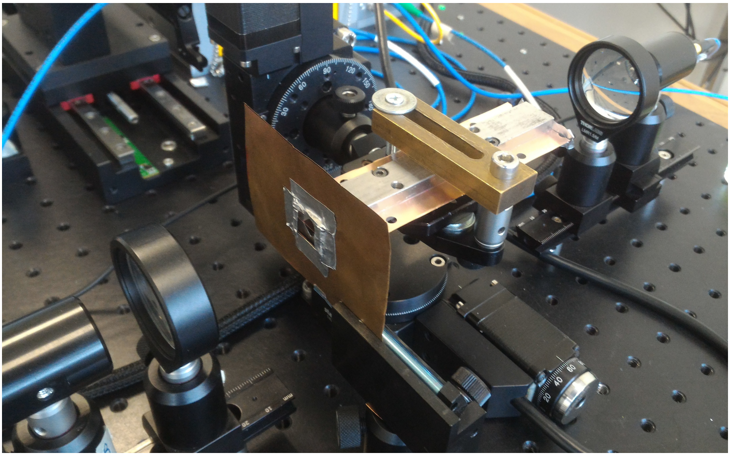

Figure 3.8: Sub-THz system with the iron DUT and copper slab placed in the optical path.

3.2.4 Higher order modes

In order to understand if there is any effect on the signal produced by the excitation of higher order modes, we evaluate the ratio between the field amplitude coefficients of the first and second order modes as a function of the beam spot size. As described in the section before, the beam has a Gaussian-like shape with a waist of approximately 8 mm.

The expression of the first (sum $TE_{1,0}$ and $TE_{0,1}$) mode in propagation at the entrance of the horn is:

$$\mathbf{e}^{\mathbf{TE}}_{\mathbf{1,0\,\&\,0,1}} = \frac{\sqrt{2}}{a}\cos\left(\frac{\pi}{a}y\right)i_x + \frac{\sqrt{2}}{a}\cos\left(\frac{\pi}{a}x\right)i_y \tag{3.10}$$

where a is the side of the waveguide and the electric field representation is in Fig. 3.4. We describe the incident field as a Gaussian in both transverse planes:

$$\mathbf{E}_{inc} = e^{-\frac{x^2+y^2}{2\sigma^2}}\left(i_x + i_y\right) \tag{3.11}$$

and we integrate their scalar product along the surface, normalizing to the total power carried out by the beam. The integral is:

$$\int_{-\frac{a}{2}}^{\frac{a}{2}}\int_{-\frac{a}{2}}^{\frac{a}{2}} \mathbf{E}_{inc}\mathbf{e}^{\mathbf{TE}}_{\mathbf{1,0\,\&\,0,1}}dxdy \tag{3.12}$$

The second (sum $TE_{2,1}$ and $TE_{1,2}$) mode in propagation at the entrance of the horn is:

$$\begin{aligned}\mathbf{e}^{\mathbf{TE}}_{\mathbf{2,1\,\&\,1,2}} = &\left[\frac{\sqrt{4}}{a\sqrt{5}}\cos\left(\frac{\pi}{a}x\right)\sin\left(2\frac{\pi}{a}y\right) - \frac{\sqrt{2}}{a\sqrt{5}}\sin\left(\frac{\pi}{a}y\right)\sin\left(2\frac{\pi}{a}x\right)\right]i_x + \\ &+\left[\frac{\sqrt{4}}{a\sqrt{5}}\cos\left(\frac{\pi}{a}y\right)\sin\left(2\frac{\pi}{a}x\right) - \frac{\sqrt{2}}{a\sqrt{5}}\sin\left(\frac{\pi}{a}x\right)\sin\left(2\frac{\pi}{a}y\right)\right]i_y\end{aligned} \tag{3.13}$$

where the electric field of the second mode in propagation is represented in Fig. 3.9. Also in this case we integrate the scalar product of (3.11) and (3.13) along the surface, normalizing to the total power carried out by the beam. The integral in this case is:

$$\int_{-\frac{a}{2}}^{\frac{a}{2}}\int_{-\frac{a}{2}}^{\frac{a}{2}} \mathbf{E}_{inc}\mathbf{e}^{\mathbf{TE}}_{\mathbf{2,1\,\&\,1,2}}dxdy \tag{3.14}$$

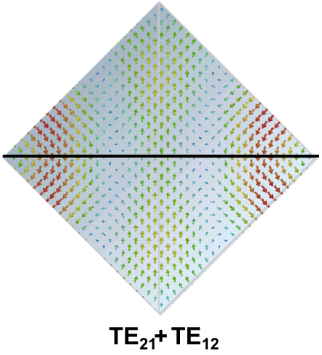

Figure 3.9: Electric field of the sum of the second two modes propagating when a slab is placed in the center.

In Fig. 3.10 there is the plot of the ratio (in dB) between the first and the second mode expansion coefficients as a function of the beam spot size (2σ). Within the experimental error, one can see that for a Gaussian-like beam with a waist of approximately 8 mm, as described in Sec. 3.2.3, this ratio turns out to be around 30 dB, definitively excluding any effect on the attenuation produced by the excitation of higher order modes.

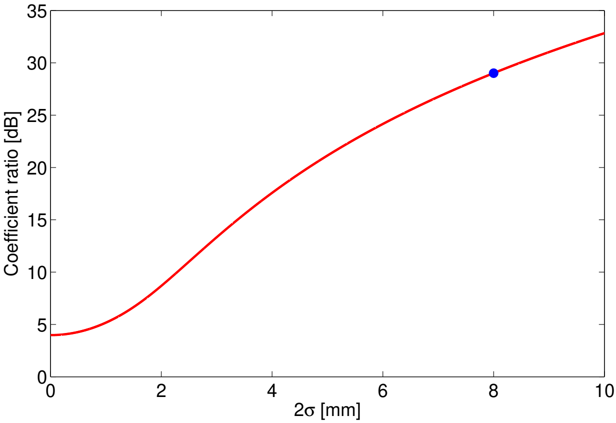

Figure 3.10: Ratio between the first and the second mode expansion coefficients as a function of the beam spot size (2σ).

This means that under our experimental conditions, we can safely assume that we work in a single mode regime and that the mode conversion at the entrance of the horn antennas may be neglected.

3.3 Signal attenuation - analytical method

The procedure consists in the evaluation of the relative signal attenuation as a function of frequency parametrized with the conductivity of the coating for each component of all the studied DUTs. The best fit of the experimental measurements with analytical curves allows to evaluate the conductivity of the material and to infer the surface impedance, if the thickness of the coating is known. The general definition of the attenuation along the waveguide walls and the estimation of the contribution in the particular case of a slab inside all the three different DUTs is detailed below.

3.3.1 General formulation

In this section we provide the general definition of attenuation in a guiding system and evaluate it in the specific case of every component of the DUTs used for the measurements. The definition of the attenuation constant is expressed by the formula [66, 68]:

$$\alpha(z) = -\frac{1}{2P}\frac{dP}{dz} \tag{3.15}$$

where P is the total power flow at z and $-dP$ is the power dissipated in a section of waveguide of length dz.
From Eq. (3.15) it follows that the attenuation constant due to losses on the walls of a generic waveguide is:

$$\alpha(z) = -\frac{1}{2}\frac{Re(Z_S(z))\int |H_{\mathrm{tan}}|^2\, ds}{Re(Z(z))\iint |H_{\mathrm{t}}|^2\, dS} \tag{3.16}$$

where Z_S is the equivalent surface impedance and Z is the characteristic impedance of the propagating mode. H_{tan} and H_{t} are the nondissipative values of the magnetic field tangential to the guide periphery and transverse to the guide cross section, respectively. The line integral with respect to ds extends over the guide periphery, and the surface integral with respect to dS extends over the guide cross section.

We consider the propagation of the sole $\mathrm{TE}_{1,1}$ mode in the cylindrical waveguide. The attenuation of this single mode in a generic cylindrical waveguide is:

$$A_{\mathrm{cyl}} = \frac{1}{2}\frac{Re(Z_S)}{Re(Z_{1,1})}\frac{\int_l \left|n \times H_{1,1}\right|^2 dl}{\left|I_{1,1}\right|^2} \tag{3.17}$$

where $Z_{i,j}$ is the i,j mode impedance and $I_{i,j}$ is the relevant excitation current. To evaluate the attenuation both in the diagonal waveguide and in the pyramidal transitions we consider the sum of two modes $\mathrm{TE}_{1,0}$ and $\mathrm{TE}_{0,1}$; the formula in this case is:

$$A_{\mathrm{diag}} = A_{\mathrm{pyr}} = \frac{1}{2}Re(Z_S)\frac{\int_l \left|n \times (H_{1,0} + H_{0,1})\right|^2 dl}{Re(Z_{1,0})\left|I_{1,0}\right|^2 + Re(Z_{0,1})\left|I_{0,1}\right|^2} \tag{3.18}$$

The field components used in Eq. (3.17) for the cylindrical waveguide, where only the mode $\mathrm{TE}_{1,1}$ propagates, are:

$$H_{r_{1,1}} = H_{r_{1,1}}(r,0) = I_{1,1}\sqrt{\frac{2}{\pi}}\frac{\chi'_{1,1}}{a_0\sqrt{\chi'^2_{1,1}-1}}\frac{J'_1(\frac{\chi'_{1,1}r}{a_0})}{J_1(\chi'_{1,1})} \tag{3.19}$$

$$H_{z_{1,1}} = H_{z_{1,1}}(r,0) = -j\frac{k_{t_{1,1}}}{k_{z_{1,1}}}I_{1,1}\sqrt{\frac{2}{\pi}}\frac{\chi'_{1,1}}{a_0\sqrt{\chi'^2_{1,1}-1}}\frac{J_1(\frac{\chi'_{1,1}r}{a_0})}{J_1(\chi'_{1,1})} \tag{3.20}$$

where a_0 is the radius of the cylindrical waveguide. The field components used in Eq. (3.18) for the diagonal waveguide and the pyramidal transitions are:

$$H_{x_{1,0}} = I_{1,0}\frac{\sqrt{2}}{a}\cos\left(\frac{\pi}{a}x\right) \tag{3.21}$$

$$H_{y_{1,0}} = I_{1,0}\frac{\sqrt{2}}{a}\cos\left(\frac{\pi}{a}y\right) \tag{3.22}$$

where a is the side of the diagonal waveguide. Furthermore, according to Leontovich approximation, the wave inside the coating behaves as a locally plane wave parallel to the surface. It is well known that the plane wave equations become completely similar to the equation of a transmission line. Therefore, in the case of coating material, the expression of Z_S which has to be inserted in Eqs. (3.17) and (3.18), is [69] is:

$$Z_S = Z_{\text{coat}} \frac{Z_{\text{cu}} + jZ_{\text{coat}} \tan(k_{\text{coat}} d)}{Z_{\text{coat}} + jZ_{\text{cu}} \tan(k_{\text{coat}} d)} \tag{3.23}$$

where d is the coating thickness. When $d = 0$ there is no coating and $Z_S = Z_{\text{cu}}$, the characteristic impedance of the copper. It has the form identical to the impedance seen at the entrance of a transmission line loaded by the surface impedance of the second medium Z_{cu} at a distance d. In Fig. 3.11 there is the representation of the impedance transportation along the transmission line.

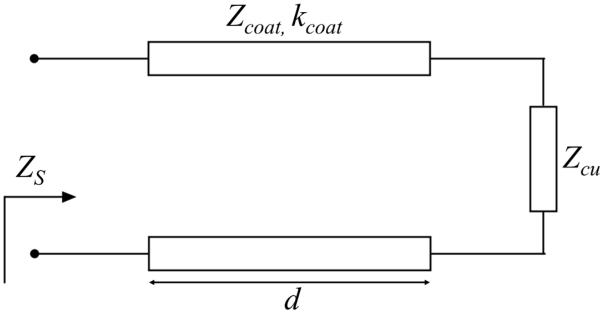

Figure 3.11: Impedance transportation along the transmission line.

The characteristic impedance in the Leontovich approximation for a metallic case ($\epsilon'' \gg \epsilon'$) is described by the formula [66]:

$$Z = (1+j)\sqrt{\frac{\omega\mu}{2\sigma}} = \frac{1+j}{\sigma\delta} \tag{3.24}$$

and the propagation constant in the same condition is:

$$k = (1-j)\sqrt{\frac{\sigma\omega\mu}{2}} = \frac{1-j}{\delta}, \tag{3.25}$$

where δ is the skin-depth defined as:

$$\delta = \sqrt{\frac{2}{\sigma\omega\mu}} \tag{3.26}$$

and where μ is the total permeability, σ the material conductivity and $\omega = 2\pi f$. As stated in Eq. (3.3), the procedure consists in the measurement and in the analytical/numerical evaluation of the relative attenuation defined as:

$$RA \triangleq A^{\text{coat}} - A^{\text{cu}}. \tag{3.27}$$

With the above definition we do not need to evaluate the attenuation on the walls but only the attenuation on the slabs placed in the center of the DUTs.

3.3.2 Estimation on the slab in the cylindrical waveguide

The first mode in the cylindrical waveguide with a slab placed in the center is the $TE_{1,1}$ and it is shown in Fig. 3.4. The constant of attenuation on the slab is:

$$\begin{aligned}
\alpha_{\text{cyl}} =& 4Re(Z_S)\frac{\chi'_{1,1}k_{z_{1,1}}}{\pi a_0 Z_0 k_0(\chi'^2_{1,1}-1)J_1^2(\chi'_{1,1})} \\
&\left[\frac{k^2_{t_{1,1}}}{k^2_{z_{1,1}}}\int_o^{\chi'_{1,1}}|J_1(u)|^2 du + \int_o^{\chi'_{1,1}}|J'_1(u)|^2 du\right] = \\
&4Re(Z_S)\frac{\chi'_{1,1}k_{z_{1,1}}}{\pi a_0 Z_0 k_0(\chi'^2_{1,1}-1)J_1^2(\chi'_{1,1})} \\
&\left[\frac{k^2_{t_{1,1}}}{k^2_{z_{1,1}}}\frac{\chi'^3_{1,1}}{12}\,{}_2F_3\left(\frac{3}{2},\frac{3}{2};2,\frac{5}{2},3;-\chi'^2_{1,1}\right)+\right. \\
&+J_0(\chi'_{1,1})\left(J_1(\chi'_{1,1})-\frac{1}{2}J_0(\chi'_{1,1})\chi'_{1,1}\right)+ \\
&+\frac{\chi'_{1,1}}{4}\,{}_2F_3\left(\frac{1}{2},\frac{1}{2};1,1,\frac{3}{2};-\chi'^2_{1,1}\right)+ \\
&+\frac{\chi'^3_{1,1}}{12}\,{}_2F_3\left(\frac{3}{2},\frac{3}{2};1,\frac{5}{2},3;-\chi'^2_{1,1}\right)+ \\
&\left.+\frac{\chi'^5_{1,1}}{1280}\,{}_2F_3\left(\frac{5}{2},\frac{5}{2};5,\frac{7}{2},5;-\chi'^2_{1,1}\right)\right]
\end{aligned} \tag{3.28}$$

were Z_0 is the characteristic impedance in the free space, a_0 is the radius of the waveguide. J_1 and J'_1 are the first order Bessel function and its derivative respectively and ${}_2F_3(\alpha,\beta;\gamma,\delta,\epsilon;z)$ is a Generalized Hypergeometric function. The quantity $\chi'_{1,1}$ is the first non-vanishing root of the equation:

$$J'_1(x) = 0$$

and

$$k_0 = \frac{\omega}{c}; \quad k_{t_{1,1}} = \frac{\chi'_{1,1}}{a_0}; \quad k_{z_{1,1}} = \sqrt{k_0^2 - k_{t_{1,1}}^2}.$$

The total attenuation along the slab of length l_g is described by the formula:

$$A_{\mathrm{cyl}} = \int_0^{l_g} \alpha_{\mathrm{cyl}} dz = \alpha_{\mathrm{cyl}} l_g \tag{3.29}$$

where l_g is the length of the waveguide.
The relative attenuation (see Eq. (3.27)) for the cylindrical waveguide is defined as:

$$RA_{\mathrm{cyl}} \triangleq A_{\mathrm{cyl}}^{\mathrm{coat}} - A_{\mathrm{cyl}}^{\mathrm{cu}}. \tag{3.30}$$

Using the Frequency solver of the CST suite [62] and resorting to the Coating Tool to perform simulations on coated layers, we managed to evaluate the difference between the analytical formula Eq. (3.30) and the electromagnetic full wave simulations for various thicknesses of the NEG coating in the cylindrical waveguide. Frequency Domain simulations have been performed by imposing the first mode propagation and comparing the scattering parameter (S_{21}) to evaluate the attenuation. We used an estimated NEG conductivity value of $\sigma_{\mathrm{coat}} = 3.5\ 10^5$ S/m, as reported in [60]. In order to avoid a conspicuous number of meshes to simulate the slab in the center of the device we performed simulation considering only one side of the structure as shown in Fig. 3.12. As shown in Fig. 3.13, the agreement between the results of Eq. (3.30) and CST tool is excellent and confirms the validity of the analytical calculations.

3.3.3 Estimation on the slab in the diagonal waveguide

The attenuation on the foil posed on the center of the diagonal waveguide is due to the sum of two modes, as explained in Sec. 3.2.2. The foil forces the propagation of the sum of the first two modes due to the boundary conditions on the metallic foil as can be seen in Fig. 3.5.
The attenuation on both sides of the slab in the diagonal waveguide is:

$$\alpha_{diag} = \sqrt{2}\frac{Re(Z_S)k_{z_{\mathrm{sum}}}}{aZ_0k_0}\left[1 + \frac{2k_{t_{\mathrm{sum}}}^2}{k_{z_{\mathrm{sum}}}^2}\right] \tag{3.31}$$

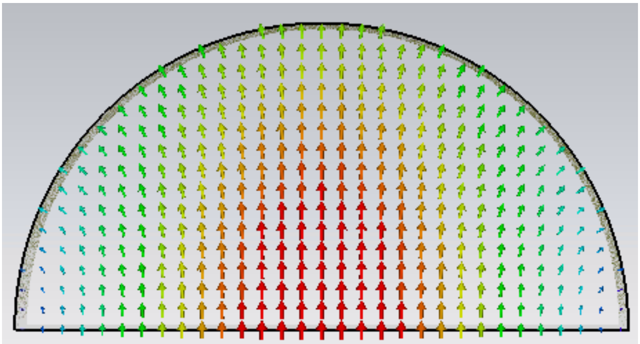

Figure 3.12: Electric field representation of the first mode propagating inside the simulated cylindrical structure.

where a is the side of the waveguide and

$$k_{t_{\mathrm{sum}}} = \frac{\pi}{a}; \quad k_{z_{\mathrm{sum}}} = \sqrt{k_0^2 - k_{t_{\mathrm{sum}}}^2}$$

The total attenuation along the slab of length l_g is described by the formula:

$$A_{\mathrm{diag}} = \int_0^{l_g} \alpha_{\mathrm{diag}} dz = \alpha_{\mathrm{diag}} l_g \tag{3.32}$$

where l_g is the length of the waveguide.
We evaluate the relative attenuation (see Eq. (3.27)) for the diagonal waveguide as:

$$RA_{\mathrm{diag}} \triangleq A_{\mathrm{diag}}^{\mathrm{coat}} - A_{\mathrm{diag}}^{\mathrm{cu}}. \tag{3.33}$$

and we check our analytical tool by evaluating the agreement between the numerical evaluation of CST and our formula for various coating thickness with a NEG conductivity value of $\sigma_{\mathrm{coat}} = 3.5 \times 10^5$ S/m.
The comparison between our analytical evaluation in Eq. (3.33), and CST Frequency Domain simulation, performed as already described in the previous section, is shown in Fig. 3.14 for a waveguide with a side of 1.1 mm. Also in this case, the agreement is very good.

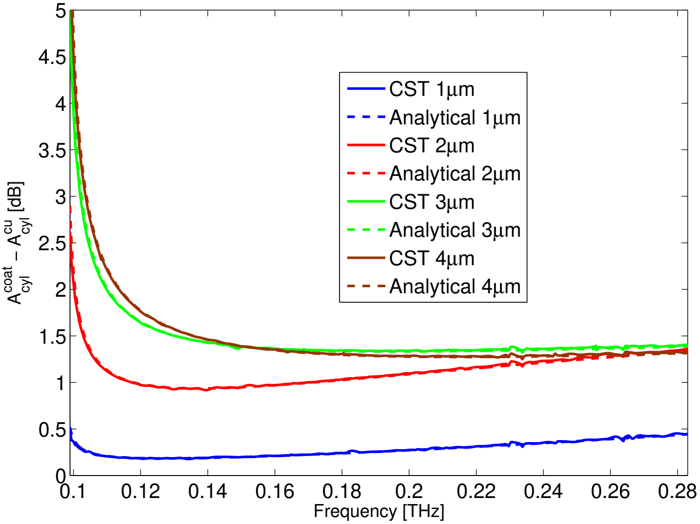

Figure 3.13: Cylindrical waveguide: relative attenuation of the first mode on the slab for different coating thickness with $\sigma_{\text{coat}} = 3.5 \times 10^5$ S/m. Comparison between analytical formulas and CST Frequency Domain simulations.

3.3.4 Estimation on the slab in the pyramidal transition

The slab placed in the center of the pyramidal transition forces the propagation of the first two degenerate modes to sum because of the boundary conditions on the metallic slab (see Fig. 3.5) as in the case of the diagonal waveguide reported before. Differently from the contribution given by the cylindrical and diagonal sections, the attenuation on the slab in the two (input and output) transitions is not a constant, since the side is changing along the waveguide. The total attenuation per unit length is:

$$\alpha_{\text{pyr}}(z) = \sqrt{2}\frac{Re(Z_S)k_{z_{\text{sum}}}(z)}{a(z)Z_0k_0}\left[1 + \frac{2k^2_{t_{\text{sum}}}(z)}{k^2_{z_{\text{sum}}}(z)}\right] \tag{3.34}$$

where

$$k_{t_{\text{sum}}}(z) = \frac{\pi}{a(z)}; \quad k_{z_{\text{sum}}}(z) = \sqrt{k_0^2 - k^2_{t_{\text{sum}}}(z)}$$

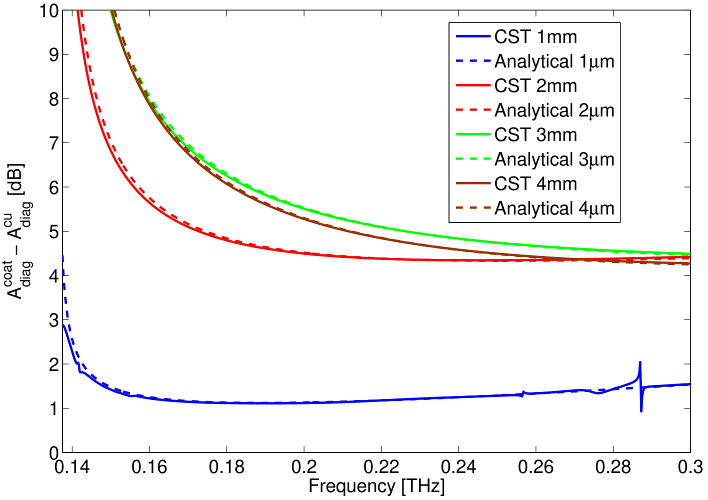

Figure 3.14: Diagonal waveguide: relative attenuation of the sum of the first two modes on the slab for different coating thickness with $\sigma_{\text{coat}} = 3.5 \times 10^5$ S/m. Comparison between analytical formulas and CST Frequency Domain simulations.

and

$$a(z) = b + zd = b + \frac{z(B-b)}{l_t}$$

expresses how the side of the waveguide changes along the transition. l_t is the longitudinal length of the transition, b and B are the side dimension of the exit and entrance of the pyramidal horn transition.

The attenuation of two modes on the pyramidal walls is given by:

$$\begin{aligned} A_{\text{pyr}} = 2\int_0^{l_t} \alpha_{\text{pyr}}(z)dz = \sqrt{2}\frac{Re(Z_s)}{Z_0} \\ \left\{ -\frac{1}{2d}\log\left[\frac{\sqrt{1-\left(\frac{\pi}{k_0 B}\right)^2}-1}{\sqrt{1-\left(\frac{\pi}{k_0 B}\right)^2}+1}\frac{\sqrt{1-\left(\frac{\pi}{k_0 a}\right)^2}+1}{\sqrt{1-\left(\frac{\pi}{k_0 a}\right)^2}-1}\right] + \right. \\ \left. +\frac{2}{d}\left[\sqrt{\left(\frac{\pi}{k_0 B}\right)^2} - \sqrt{\left(\frac{\pi}{k_0 a}\right)^2}\right]\right\} \end{aligned} \tag{3.35}$$

As for the waveguides, we evaluate the relative attenuation (see (3.27)) for the pyramidal transition as:

$$RA_{\text{pyr}} \triangleq A_{\text{pyr}}^{\text{coat}} - A_{\text{pyr}}^{\text{cu}}. \tag{3.36}$$

The comparison between this analytical evaluation and the CST Frequency Domain solver is shown in Fig. 3.15 for $\sigma_{\text{coat}} = 3.5 \times 10^5$ S/m and with the smaller side of the transition of $0.9\sqrt{2}$ mm. Again the agreement is very good.

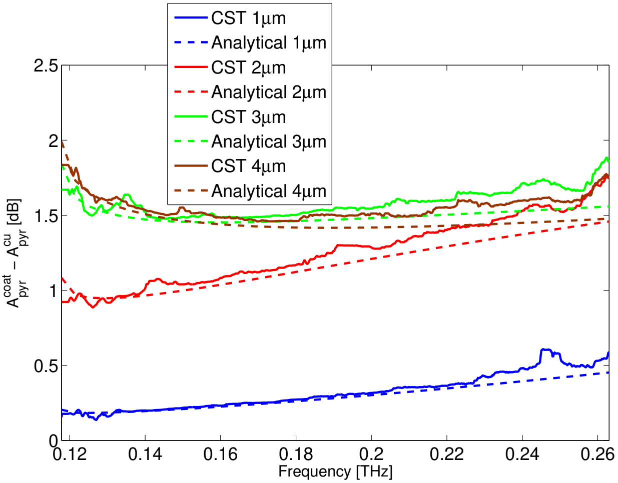

Figure 3.15: Pyramidal transitions: relative attenuation of the sum of the first two modes on the slab for different coating thickness with $\sigma_{\text{coat}} = 3.5 \times 10^5$ S/m. Comparison between analytical formulas and CST Frequency Domain simulations.

3.3.5 Estimation on the slab in the DUTs

The total relative attenuation along the entire DUTs is analytically evaluated as the sum of Eqs. (3.30) and (3.36) for the iron DUT and as sum of Eqs. (3.33) and (3.36) for the copper and stainless steel DUT. As described in Sec. 3.2.2, we neglect the contribution to losses given by further modes in the transition between the pyramidal horns and the cylindrical waveguide in the iron DUT. Therefore, the comparison with CST simulations on the overall assembled structure for various coating thicknesses ($\sigma_{\text{coat}} = 3.5 \times 10^5$ S/m) is an effective way to test the validity of this assumption and to test also the other two DUTs. The very good agreement shown in Figs. 3.16 and 3.17, confirms the possibility of neglecting any mode conversion inside the horn or along the transition in the analytical model for all the three DUTs.

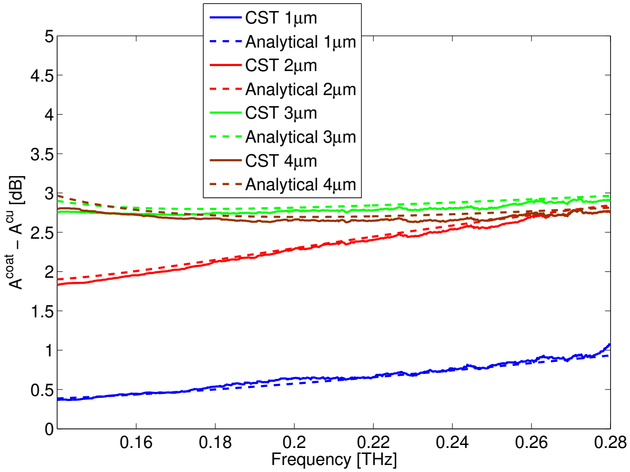

Figure 3.16: Complete iron DUT: relative attenuation of propagating mode on the slab for different coating thicknesses with $\sigma_{\text{coat}} = 3.5 \times 10^5$ S/m. Comparison between analytical formulas (dashed line) and CST Frequency Domain simulations (solid line).

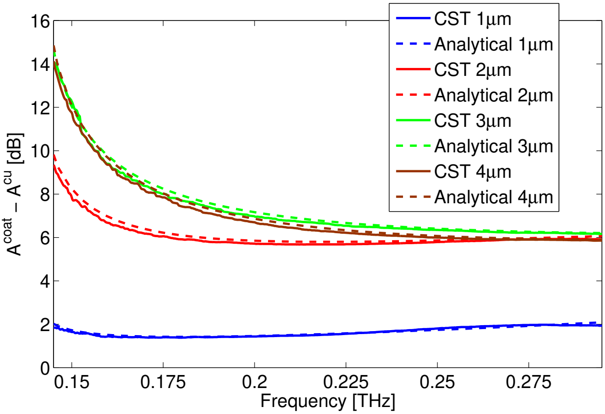

Figure 3.17: Complete copper DUT: relative attenuation of propagating mode on the slab for different coating thicknesses with $\sigma_{\text{coat}} = 3.5 \times 10^5$ S/m. Comparison between analytical formulas (dashed line) and CST Frequency Domain simulations (solid line).

3.4 Measurement results

The measurements have been performed with the three different devices described in Table 3.1 with the coated slab described in Sec. 3.4.1. The work on the iron DUT is also reported in Ref. [70]. Due to the small dimension of all the three devices and due to their peculiar shape, because each one consists of two shells placed one on top of the other, the importance of the compliance with requested machine tolerances is highlighted in detail in this section.

3.4.1 Coating process

Four slabs in total have been coated, two of them have the same length of the first DUT (120 mm) and the other two with the same length of the other two DUTs (140 mm). All four slabs are 50 μm thick. During the deposition process the slabs are fixed in an aluminum frame in order to prevent deformation (see Fig. 3.18).

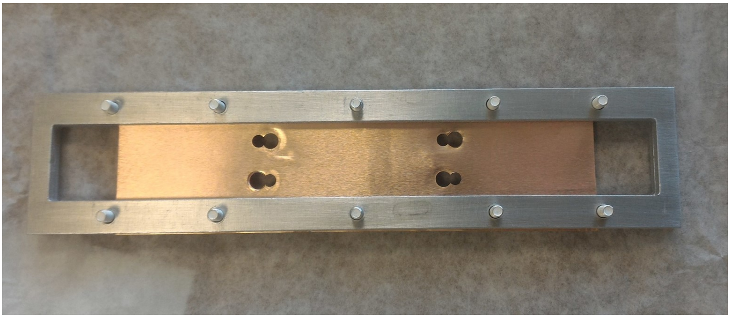

Figure 3.18: Picture of the longitudinal copper slab framed for the NEG deposition.

The NEG growth process was performed at the CERN deposition facilities on both sides of all the four copper slabs by using a DC magnetron sputtering technique [42]. The cathode of Titanium, Zirconium and Vanadium (TiZrV cathode) was at a distance of 200 mm from the substrate, the sputtering process gas was Krypton and the working pressure was about 7×10^{-4} mbar. The coating process parameters are listed in Table 3.3.

The evaluation of thickness and composition of the coating deposition have been performed by X-ray fluorescence (XRF) measurements along the median line of the slab, which will coincide with the waveguide axis. The values of thickness and composition are shown in Figs. 3.19, 3.20, 3.21 and 3.22. The first two figures are related to the two 120 mm long slabs, the second two are related to one of the

Slab	tension	current	avg. power	time
1^{st} 120 mm	284 V	750 mA	212 W	46.5 h
2^{nd} 120 mm	283 V	750 mA	205 W	45.5 h
1^{st} 140 mm	318 V	750 mA	238 W	39 h
2^{nd} 140 mm	294 V	750 mA	225 W	45.5 h

Table 3.3: Coating process parameters.

two 140 mm long slabs (the detailed values of one coated slab are not available). The mean value of the thickness of the coating used in our experiment is 3.96 μm and 3.68 μm for the 120 mm slabs and 4.26 and 3.80 for the ones of 140 mm length. The evaluated average percentage of Titanium, Zirconium and Vanadium in the coating is 31 %, 36.5 % and 32.5 % for the first sample and 30.5 %, 37 % and 32.5 % for the second one of 120 mm and 31.3 %, 37 % and 31.7 % for the first sample of the 140 mm slab..

Attempts of Amorphous Carbon (a-C) coating have been also performed on small square samples of copper (40×40 mm^2 with a thickness of 50 μm). The thickness needed to have an evident signal attenuation on a-C is 5 μm on both sides without affecting the planarity of the sample. Figures 3.23 and 3.24 show the problems encountered on the coated samples. The deposited a-C layer induces a residual stress on the copper slab. In fact, in case of coating on one side only, the copper slab starts to bend. Instead when the coating is performed on both sides, the stress on both sides causes peel off and creates blister. These imperfections do not allow to have an a-C sample available for the measurement. The goal for the future is to fine tune the process parameters in order to reach the desired thickness that is one order of magnitude higher than the usually required thickness for coating of vacuum chambers.

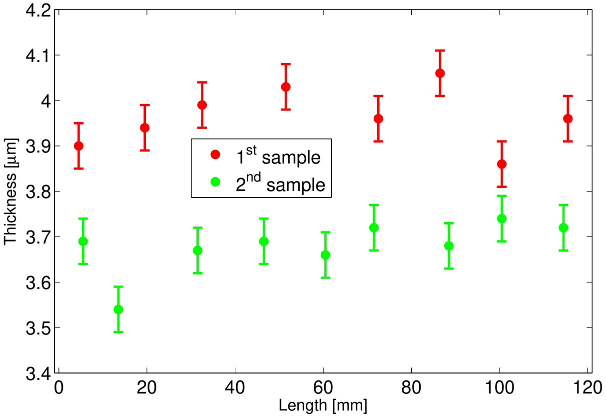

Figure 3.19: Measurements of the NEG coating thickness on the two copper slabs of 120 mm.

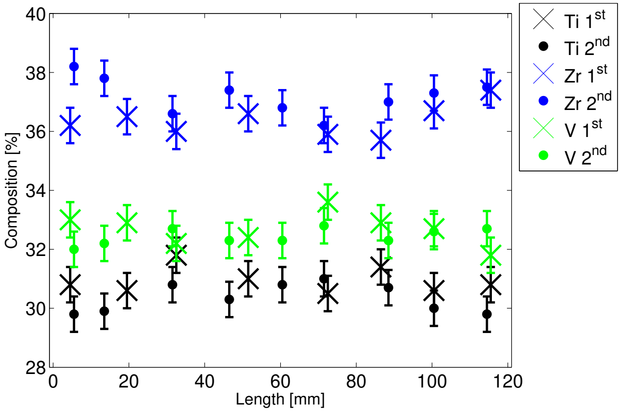

Figure 3.20: Measurements of the NEG coating composition on the two copper slabs of 120 mm.

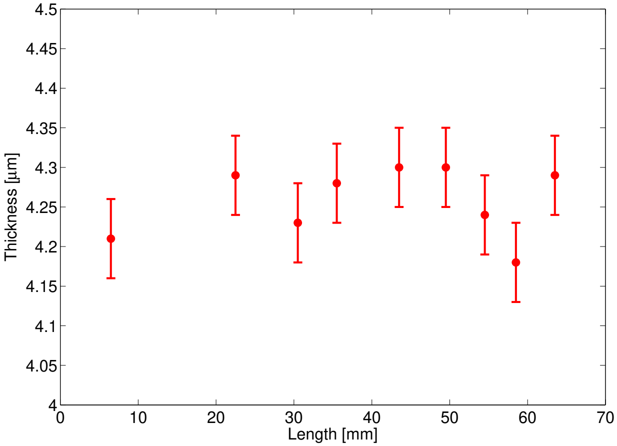

Figure 3.21: Measurement of the NEG coating thickness along the half of one of the two copper slabs of 140 mm. The measurement is performed along half slab.

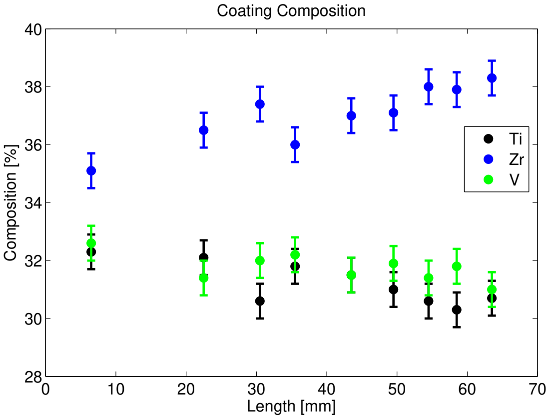

Figure 3.22: Measurement of the NEG coating composition along one of the two copper slabs of 140 mm. The measurement is performed along half slab.

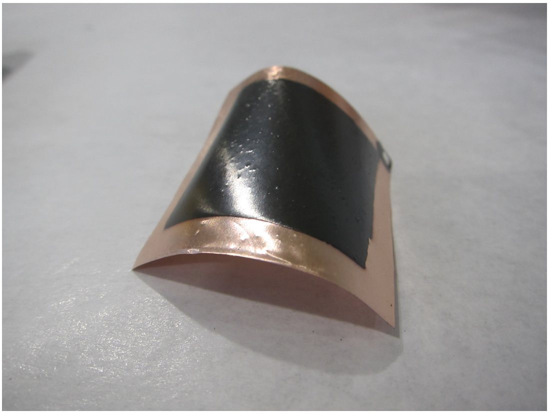

Figure 3.23: Amorphous Carbon coating on one side of copper sample. The sample shows a mechanical stress.

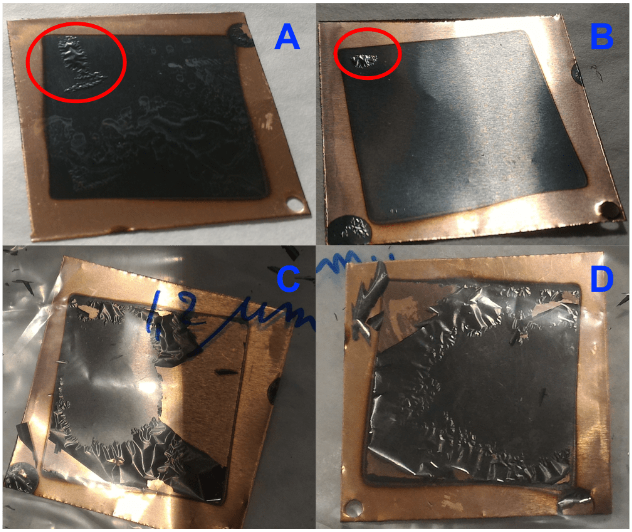

Figure 3.24: Amorphous Carbon coating on both sides of a copper sample. *A* and *B* are both sides after the coating process, circled in red there are the seeds of the peel off. *C* and *D* are the same sides after one month, the peel off is evident.

3.4.2 Iron DUT (cylindrical waveguide + pyramidal transitions)

As first step, we tested the quality of the manufactured iron DUT by rotating it 90° with respect to the direction of the source electric field of the time domain spectrometer. This test is performed without the central slab and it is useful to check the symmetry of the DUT and eventual losses caused by undesired space between the two shells.
In Fig. 3.25 the two time domain signals passing through the DUT in both configurations with respect to the polarization of the electric field are shown. The two signals are almost superimposed, confirming the good quality of the manufacturing in terms of top-bottom and left-right symmetry. The small difference in amplitude of the two signals is caused by the losses due to the current flowing in the space between the two shells. We may consider these losses negligible with respect to the power flowing inside the structure.

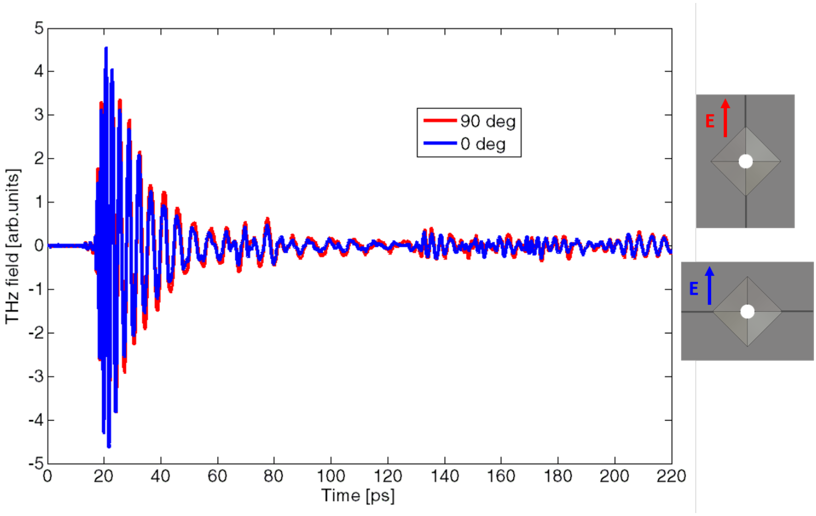

Figure 3.25: Time domain measurements on the iron DUT without the central slab to check the symmetry of the waveguide by rotating it of 90° with respect to the direction of the source electric field of the time domain spectrometer.

After the quality test on the device, we started the measurements on two different copper slabs coated with NEG having 3.96 μm and 3.68 μm average thickness, already described in Sec. 3.2.1 (see Fig. 3.19) and a bare copper slab that is used as reference. We performed five different measurements for all three samples, by replacing the slab each time, in order to reduce the unavoidable uncertainty given by the measurement procedure. After data averaging, the related error is reduced, nevertheless it is much larger than the statistical fluctuations coming from the TDS performance (laser stability, mechanical vibrations, environment noise, etc.).

The mean amplitude spectrum derived by the DFT analysis is shown for each sample in Fig. 3.26 in the frequency range of our interest (118 - 283 GHz). The data show that the attenuation on the two NEG coated samples (blue and green dots) is constantly larger than on the copper slab (red dots). Moreover, losses tend to increase with higher frequency, likely indicating a reduction of the skin depth to values smaller than the coating thickness. Furthermore, at the lowest frequencies the noise distorts the signal and can introduce artificial phase discontinuities, making the phase unwrapping difficult and producing artifacts in the data spectrum [71]. For this reason, we discard the data below 160 GHz, and in the following all results are presented in the frequency range 160 - 283 GHz. The experimental results are then compared with the analytical model based on the theory described in Sec. 3.3 as function of the coating conductivity. The extended formula of the relative attenuation for the iron DUT is given by the sum of the

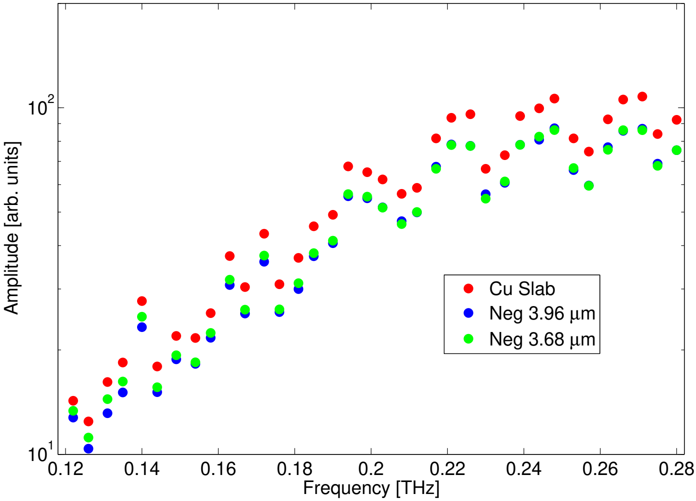

Figure 3.26: Frequency spectrum showing the averaged amplitude data for the three samples: copper slab (red dots), NEG coated slab 3.96 μm (blue dots) and NEG coated slab 3.68 μm (green dots).

relative attenuation along the cylindrical waveguide and one on the two pyramidal transitions. The complete formula is:

$$RA_{\text{iron DUT}} = RA_{\text{cyl}} + 2RA_{\text{pyr}} \tag{3.37}$$

resorting to Eqs. (3.30) and (3.36).

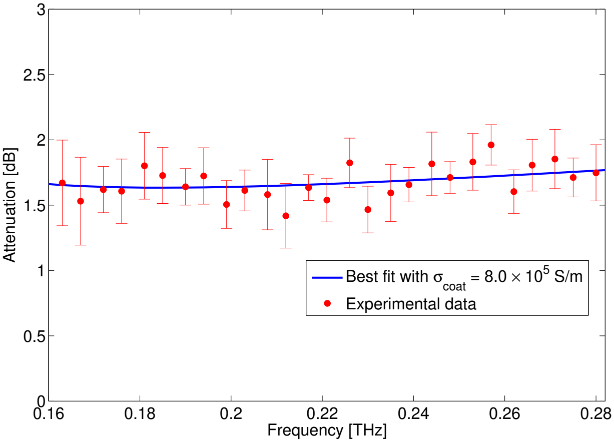

Figure 3.27: Attenuation on the NEG coated slab of 3.96 μm: averaged experimental data (red dots) and best fit curve (blue). The value of reduced $\chi^2 = 0.40$.

In Fig. 3.27, the measurements for the 3.96 μm coating are shown. From the best fit with the analytical formula, we get the value $\sigma_{\text{coat}} = (8.0 \pm 0.4) \times 10^5$ S/m and a value of 0.40 for the reduced χ^2 [72]. Similarly, in Fig. 3.28 the same measurements are shown for the 3.68 μm coating. In this case, the estimated value of σ_{coat} is $(8.2 \pm 0.6) \times 10^5$ S/m and reduced χ^2 is equal to 0.36.

The uncertainties on the conductivity values are evaluated with respect to the average attenuation measured with a confidence interval of 95 %.

As expected, given the similar thickness, the two NEG coatings show the same value for the estimated conductivity, within the error determined by the fitting procedure. It is worthwhile to note that this value is also in good agreement with previous results obtained for the same alloy measured using the frequency domain approach [60].

In order to evaluate the effect of the sample roughness on the estimation of NEG conductivity we performed an estimation on effective conductivity following the formula in [73]. Considering the values of estimated average roughness for similar samples with the same coating process [60, 74], we assume for our samples a roughness average value of 0.2 μm, which gives a maximum reduction in conductivity of the order of 7%. This value lies within the measurement error band in our frequency range. Nevertheless, it is worthwhile to observe that the roughness cannot be neglected at higher frequencies.

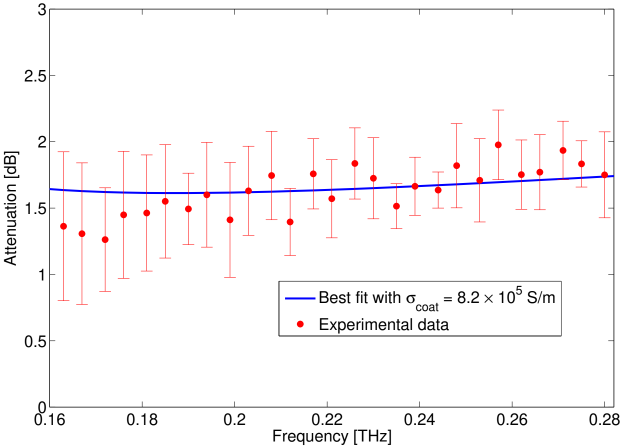

Figure 3.28: Attenuation on the NEG coated slab of 3.68 μm: averaged experimental data (red dots) and best fit curve (blue). The value of reduced $\chi^2 = 0.36$.

In Figs. 3.29 and 3.30, the evaluation of the real part of the surface impedance as function of the frequency is shown, see Eq. (3.23). The real part goes from 0.85 to 1.25 Ω for the slab of 3.96 μm and from 0.75 to 1.25 Ω for the slab of 3.68 μm in the same frequency range.

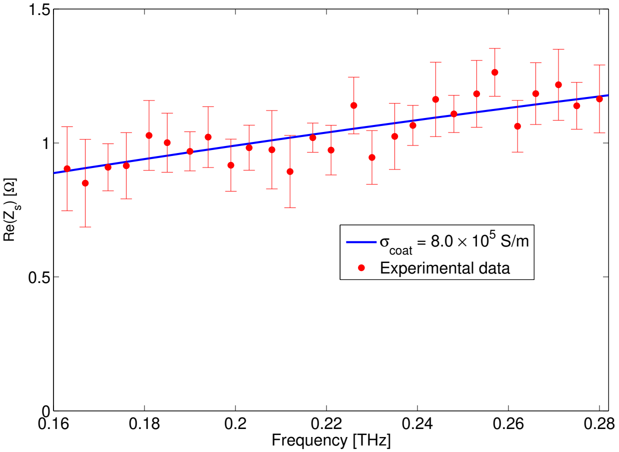

Figure 3.29: Surface impedance estimation of the 3.96 μm NEG coated slab: from averaged experimental data (red dots) and from best fit curve conductivity (blue).

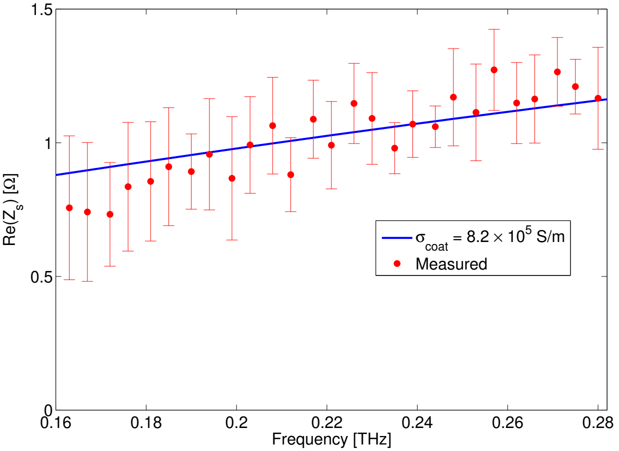

Figure 3.30: Surface impedance estimation of the 3.68 μm NEG coated slab: from averaged experimental data (red dots) and from best fit curve conductivity (blue).

3.4.3 Stainless steel DUT (diagonal waveguide + pyramidal transitions)

Also in this case, we checked the symmetry and the quality of this guiding system by rotating it 90° with respect to the direction of the source electric field.
The evaluation of the real part of the surface impedance as function of the frequency is shown in Fig. 3.31. The two time domain signals are completely different and this is a clear indication of geometrical asymmetries and/or losses in the space between the two shells of the device due to problems in the planarity of the structure. The ’0 deg’ signal (blue curve), that is the one that is used to characterize the coating on the slab, shows a modulation that is totally unexpected and it is probably due to the undesired multiple reflection along the internal path of the guiding system.

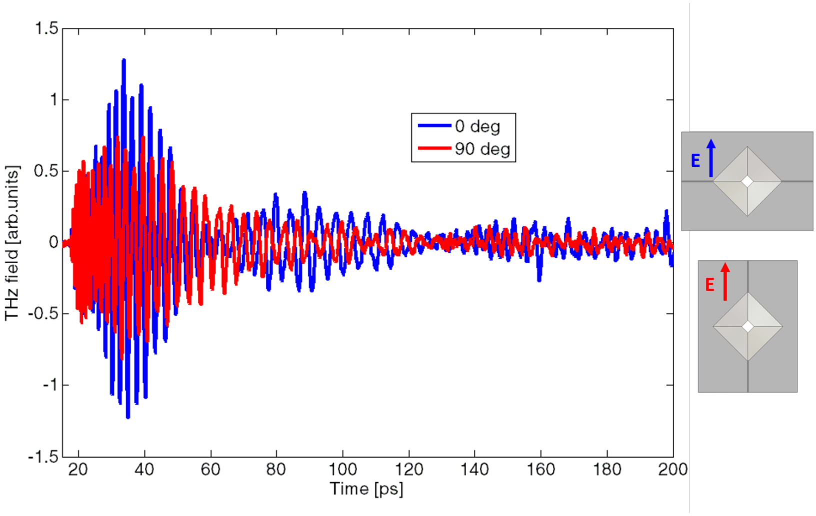

Figure 3.31: Time domain measurements on the stainless steel DUT without the central slab to check the symmetry of the waveguide by rotating it of 90° with respect to the direction of the source electric field.

Metrological measurements have been performed in the CERN Metrology Laboratory and the results confirm that the device does not respect the requested tolerances. In fact, as shown in Fig. 3.32, the profile of the shape and the planarity of the shell does not respect the requested tolerances of 20 μm in any measured point. Only one half of one shell is shown for exemplification, the other parts of the device have similar results. This means that the guiding system is smaller than

requested.
The real concern is for the assembled device, for which a tolerance of 100 μm was requested. In Fig. 3.33, it is clear that also these tolerances were not respected in the manufacturing of this device. Only one side of the device is shown, the other side shows similar results, this means that when the guiding system is assembled it is not top-bottom symmetric and this will affect the measurements. These results show the importance of the compliance with requested machine tolerances. We decided not to perform measurements on NEG coated slabs with this device.

To evaluate the influence of some defects on the device behaviour, we simulated them on the diagonal waveguide. The first defect is a gap between the two shells. A gap of only 5 μm leads to a signal attenuation between 15 and 10 dB (see Figs. 3.34 and 3.35). The second defect is an error on the angle aperture of the waveguide of 5°. This error leads to a shift in frequency of the two modes in propagation of 20 GHz (see Figs. 3.36, 3.37 and 3.38). This shift in frequency may create an interference between the two modes and a wrong reception of the signal on the other side of the device.

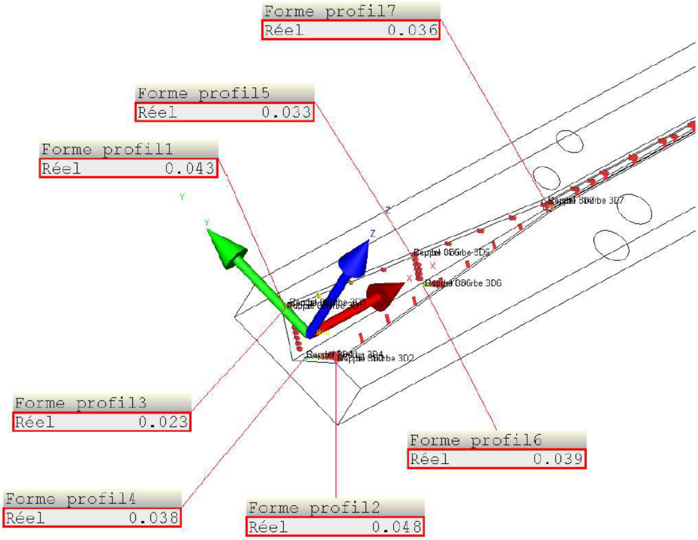

Figure 3.32: Results of the metrological measurements performed on a half shell of the stainless steel DUT. Only one half of one shell is shown for exemplification. The requested tolerance is 20 μm.

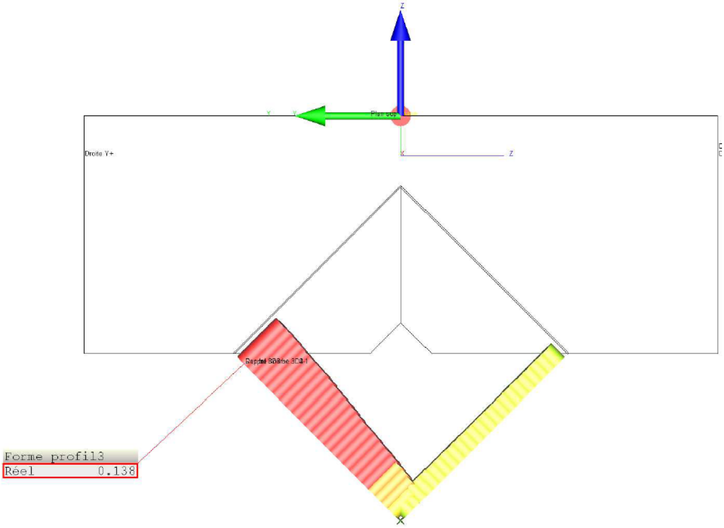

Figure 3.33: Results of the metrological measurements performed on the assembled stainless steel DUT. Only one side of the device is shown for exemplification. The requested tolerance is 100 μm.

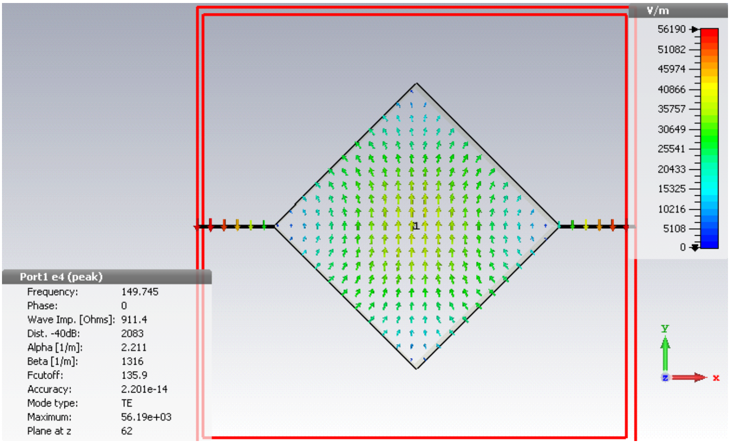

Port1 e4 (peak)
Frequency: 149.745
Phase: 0
Wave Imp. [Ohms]: 911.4
Dist. -40dB: 2083
Alpha [1/m]: 2.211
Beta [1/m]: 1316
Fcutoff: 135.9
Accuracy: 2.201e-14
Mode type: TE
Maximum: 56.19e+03
Plane at z 62

Figure 3.34: Mode passing through the diagonal waveguide 62 mm long with a gap of 10 μm between the two shells.

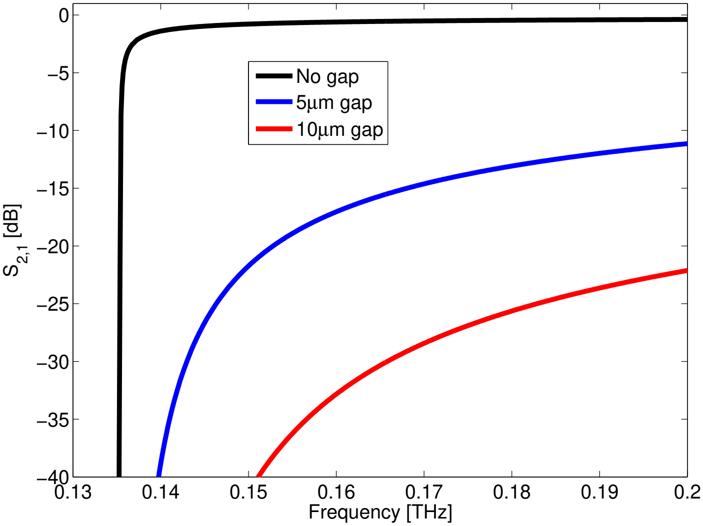

Figure 3.35: Simulated $S_{2,1}$ parameter for diagonal waveguides 62 mm long. The first one (black curve) without gap between the two shells, the second one (blue curve) with a gap of 5 μm and the third one (red curve) with a 10 μm gap.

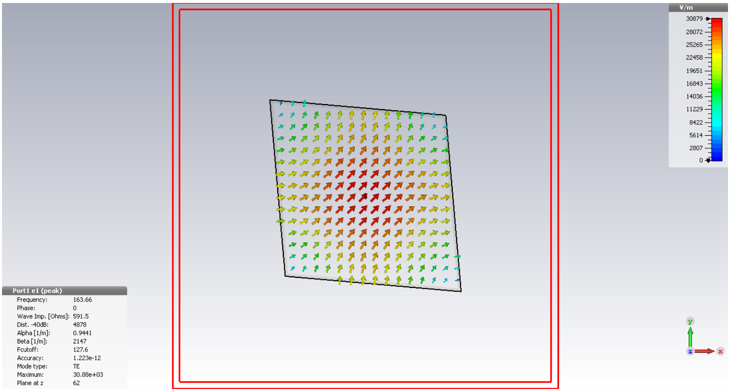

```
Port1 e1 (peak)
Frequency:            163.66
Phase:                0
Wave Imp. [Ohms]:     591.5
Dist. -40dB:          4878
Alpha [1/m]:          0.9441
Beta [1/m]:           2147
Fcutoff:              127.6
Accuracy:             1.223e-12
Mode type:            TE
Maximum:              30.88e+03
Plane at z            62
```

Figure 3.36: First mode in propagation for diagonal waveguides 62 mm long with an error of $5°$ on the angle of the aperture.

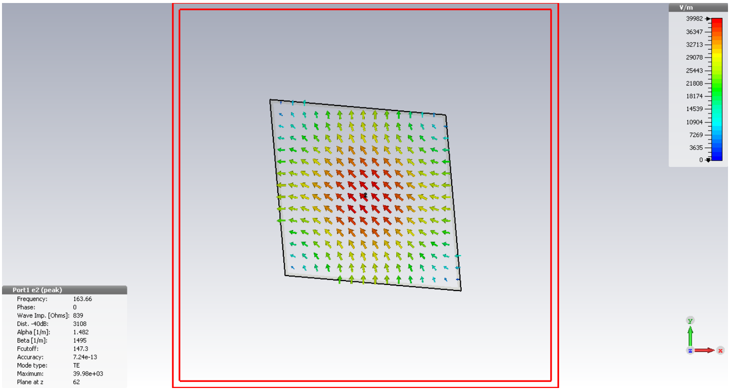

```
Port1 e2 (peak)
Frequency:          163.66
Phase:              0
Wave Imp. [Ohms]:   839
Dist. -40dB:        3108
Alpha [1/m]:        1.482
Beta [1/m]:         1495
Fcutoff:            147.3
Accuracy:           7.24e-13
Mode type:          TE
Maximum:            39.98e+03
Plane at z          62
```

Figure 3.37: Second mode in propagation for diagonal waveguides 62 mm long with an error of 5° on the angle of the aperture.

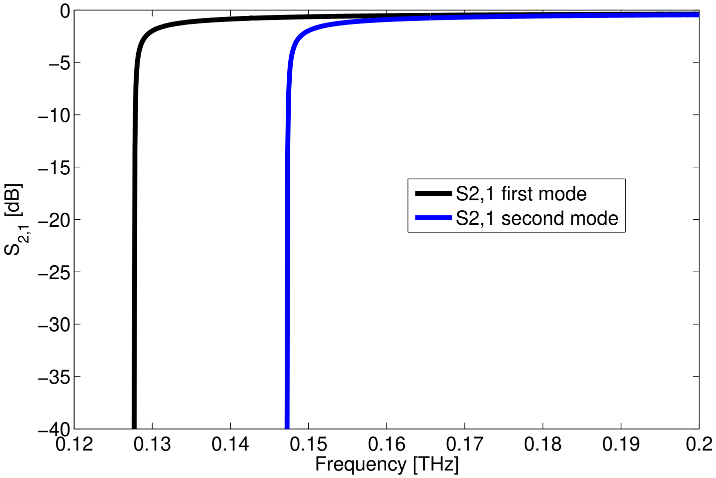

Figure 3.38: Simulated $S_{2,1}$ parameter for diagonal waveguides 62 mm long. The black curve is the first mode in propagation, the blue curve is the second mode in propagation for an error of 5° on the angle of the aperture.

3.4.4 Copper DUT (diagonal waveguide + pyramidal transitions)

We tested the symmetry and the overall quality also for this device. After the first trial, the signal passing trough the DUT without the central slab was not enough to perform reliable measurements. In order to improve the transmitted signal we decided to enhance the planarity of the two shells by sanding the two contact planar surfaces. In Fig. 3.39 the results of the time domain signals after this treatment in both configurations show a good similarity. The '0 deg' signal (blue curve), that is the one that will be used with the coated slabs, shows an amplitude attenuation with respect to the '90 deg' signal (red curve) and this is probably due to a non-perfect contact between the two shells that still exists causing propagation loss in the guiding system.

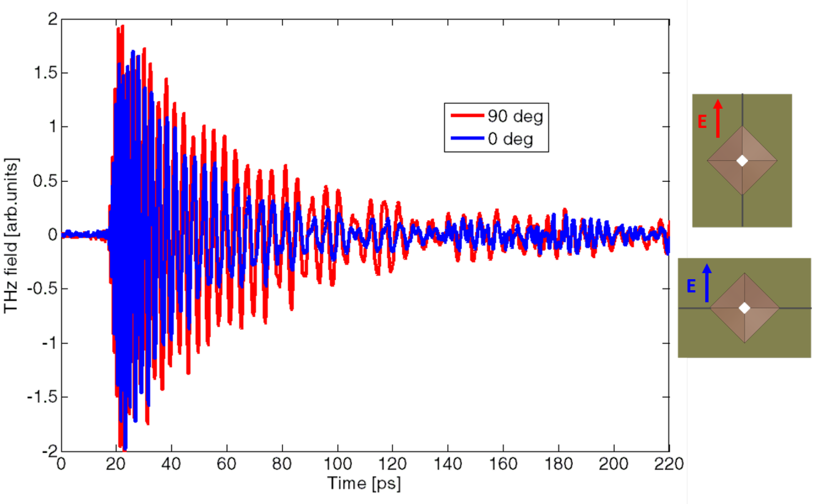

Figure 3.39: Time domain measurements on the copper DUT without the central slab to check the symmetry of the waveguide by rotating it of 90° with respect to the direction of the source electric field.

We measured the conductivity value on two different copper slabs coated with NEG having 4.26 μm and 3.80 μm average thickness (see Fig. 3.21) and a bare copper slab. The procedure is the same performed for the iron DUT and reported in Sec. 3.4.2. For this set we performed two different measurements by replacing the slab each time.

The mean amplitude spectrum derived by the DFT analysis is shown for each sample in Fig. 3.40 in the frequency range of our interest (135 to 300 GHz). Also in this case, the attenuation on the two NEG coated samples (blue and green dots) is constantly larger than on the copper slab (red dots) and the losses tend to increase with higher frequency. We discarded the data below 200 GHz to avoid the noise distortion and artifacts in the data spectrum; in the following all results are presented in the range 200 - 300 GHz.

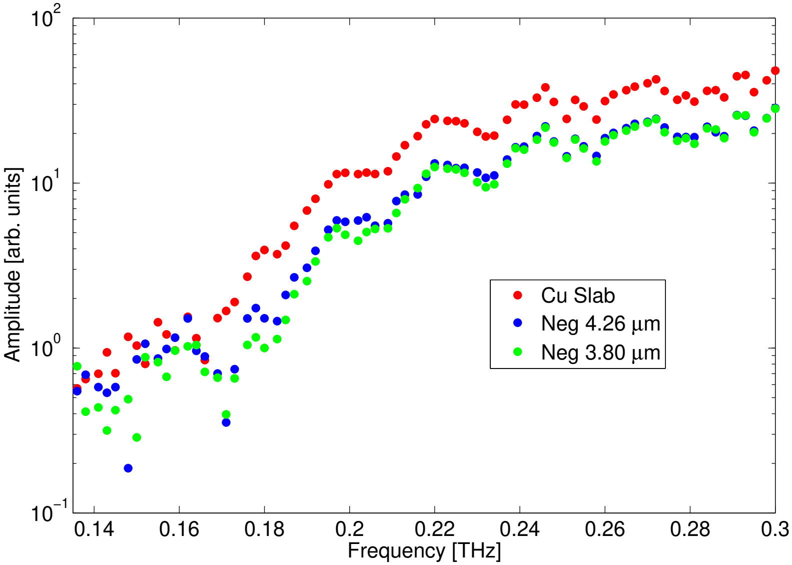

Figure 3.40: Frequency spectrum showing the averaged amplitude data for the three samples: copper slab (red dots), NEG coated slab 4.26 μm (blue dots) and NEG coated slab 3.80 μm (green dots).

The experimental results are compared with the analytical model as function of the coating conductivity. The extended formula of the relative attenuation for the copper DUT is:

$$RA_{\text{cu DUT}} = RA_{\text{diag}} + 2RA_{\text{pyr}} \tag{3.38}$$

resorting to Eqs. (3.33) and (3.36).

In Fig. 3.41, the measurement results for the 4.26 μm coating are shown. From the best fit of the analytical formula, we get the value $\sigma_{\text{coat}} = (4.9 \pm 0.5) \times 10^5$ S/m

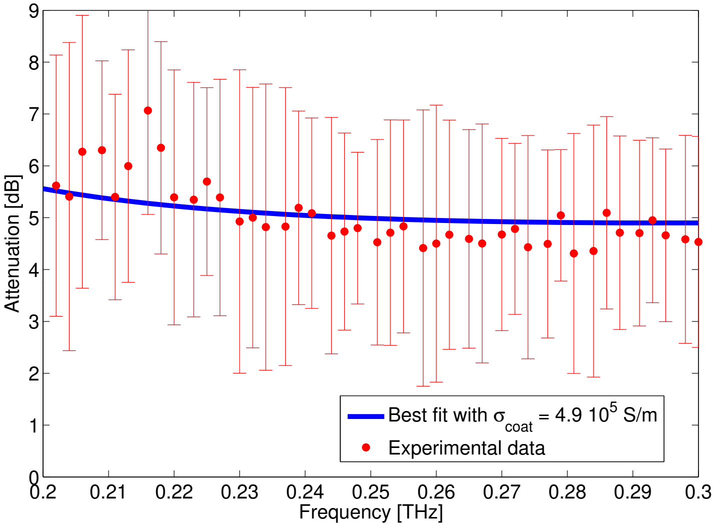

Figure 3.41: Attenuation on the NEG coated slab of 4.26 μm: averaged experimental data (red dots) and best fit curve (blue). The value of reduced $\chi^2 = 0.06$.

and a value of 0.06 for the reduced χ^2. Similarly, in Fig. 3.42 the same results are shown for the 3.80 μm coating. In this case, the estimated value of σ_{coat} is $(4.3 \pm 0.5) \times\ 10^5$ S/m and reduced χ^2 is equal to 0.50. As in the case of the iron DUT, the uncertainties are evaluated with respect to the average attenuation measured with a confidence interval of 95 %. The error bar is large because only two measurements were performed.

The values of estimated conductivity obtained by using the copper DUT is different from the one estimated with iron DUT (see Sec. 3.4.2). This reason of this discrepancy and which value of conductivity will be used to evaluate the effect of the coating on beam dynamics is explained in detail in Sec. 3.5.

3.5 Conclusion on the experimental results

In Sec. 3.4 we described the measurements performed with the three different devices described in detail in Table 3.1 in order to evaluate the EM properties of NEG.

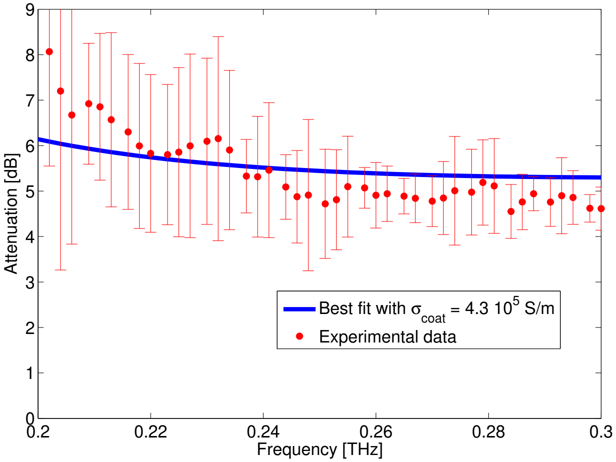

Figure 3.42: Attenuation on the NEG coated slab of 3.80 μm: averaged experimental data (red dots) and best fit curve (blue). The value of reduced $\chi^2 = 0.50$.

The measurements on stainless steel waveguide (sec. 3.4.3) shows the importance of the compliance with requested machine tolerances. We did not manage to perform reliable measurements on that waveguide. Anyway, we did measurements on the iron DUT (sec. 3.4.2) and on the copper DUT (sec. 3.4.4). The values of conductivity obtained by using the the two devices is different. This discrepancy is due to the discrepancy between the real geometry of the DUT and the one assumed in the analytical evaluation. In fact, the cylindrical central part of the iron DUT is drilled while the two shells are joint. Whereas, the diagonal part of the copper DUT is manufactured by milling each shell one at a time. The drilling allows a better precision compared to the milling procedure in terms of tolerances and alignment between the two shells. That is why we rely on the measurements performed with the iron DUT (drilled cylindrical waveguide), which leads to a conductivity of about $\sigma_{coat} = 8 \times 10^5$ S/m. Due to technical issues with the application of thick a-C coatings described above, no measurements could be performed with a-C coated slabs. However, the method developed here can be equally applied once a-C coatings with such thickness become available.

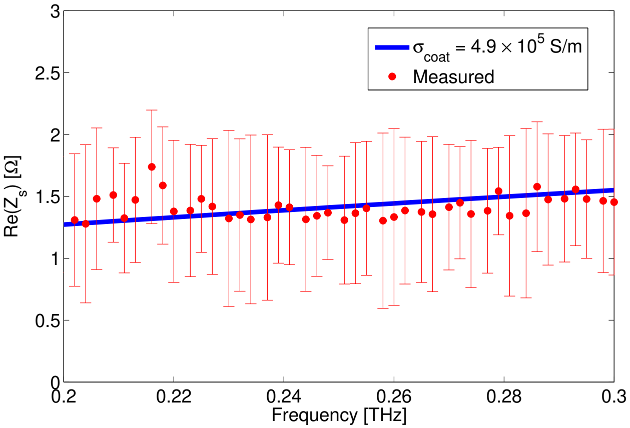

Figure 3.43: Surface impedance estimation of the 4.26 μm NEG coated slab: from averaged experimental data (red dots) and from best fit curve conductivity (blue).

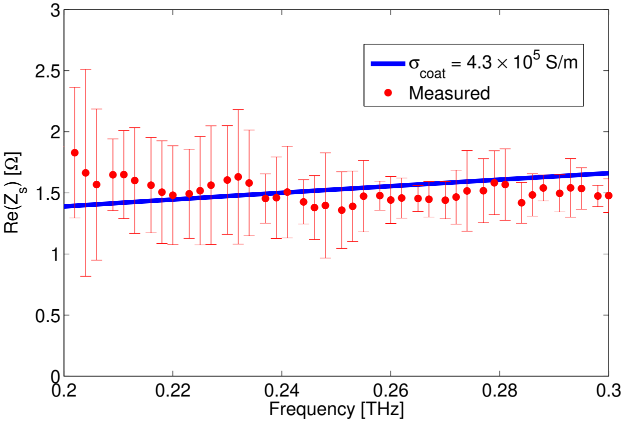

Figure 3.44: Surface impedance estimation of the 3.80 μm NEG coated slab: from averaged experimental data (red dots) and from best fit curve conductivity (blue).

4 CLIC DRs impedance budget

4.1 Introduction

This study allows to evaluate the single bunch effects with PyHEADTAIL simulations (see Sec. 2.5.2). For the transverse plane, in a first step the impact of the BBR resonator part is studied for different values of chromaticity. Then the effect of the synchrotron radiation damping and the quantum excitation is considered as explained in Sec. 2.2.1. The next step includes the RW component in order to model the contribution of the wigglers, the arcs and the rest of the FODO cell by exploiting the NEG coating electromagnetic characterization of Chapter 3. In the longitudinal plane, the effect of a BBR and of the synchrotron radiation is also discussed.

Since the CLIC DR bunch properties exhibit very small transverse emittances, the numerical simulations were performed without taking amplitude detuning into account. Similarly, since the bunch length is very short compared to the RF bucket, a linearized restoring force is considered in the longitudinal plane. Also the effects of space charge and electron-cloud are neglected. In Table 4.1 the CLIC DR parameters for RF frequency of 1 GHz used in the PyHEADTAIL simulations are reported [9, 10, 75].

4.2 Transverse impedance budget

As stated in Sec. 1.3, the role of the CLIC DRs is to produce the required ultra-low emittance at a high bunch intensity with a fast repetition time, satisfying the luminosity requirements of the final experiment. In this section, we evaluate the available transverse impedance budget in order to ensure safe machine operation with the designed bunch current. The final model cannot be considered complete because it does not take into account elements like strip-line kickers, RF-cavities and devices for beam instrumentation and diagnostic because of the difficulty to simulate such complex geometries at high frequencies.

Parameter	Symbol	Value
Energy	E	2.86 GeV
Machine Circumference	$C = 2\pi R_0$	427.5 m
Number of electrons/bunch	N_b	4.1×10^9
R.m.s. emittances	$\epsilon_{x,y}$	456.0/4.8 nm
Tunes	$Q_{x,y}$	48.35/10.40
Average beta functions	$< \beta_{x,y} >$	3.475/9.233 m
Bunch length	$\sigma_z = (c\sigma_t)$	1.8 mm (6 ps)
Momentum spread	σ_δ	1.07×10^{-3}
Synchrotron tune	Q_s	0.0057
Momentum compaction factor	α	1.27×10^{-4}
RF voltage	V	5.1 MV
Harmonic number	n_{rf}	1456
Damping times	$\tau_{x,y,s}$	2, 2, 1 ms
Energy loss per turn	U_0	3.98 MeV

Table 4.1: CLIC DR parameters used in simulations [76].

4.2.1 Broad-band resonator

The first step is to assume the whole ring modeled as a broad-band resonator (BBR). The expression of the transverse wake functions are stated in (2.50).

A series of PyHEADTAIL simulations were performed with different transverse shunt impedance and resonator frequency values, in order to evaluate the instability threshold. A strong head-tail instability, also named Transverse Mode Coupling Instability (TMCI), may affect the CLIC DR bunch and cause rapid beam loss if the transverse impedance is too high [25]. In case of a round beam and axisymmetric geometry for a short or very long bunch there is a criterion to evaluate the TMCI threshold [77, 78]:

$$\frac{\omega_r/2\pi < \beta_{x,y} > R_T N_b e}{3.75 Q E/e} < \begin{cases} \dfrac{Q_s}{\omega_r \sigma_t}, & \text{if } \omega_r \sigma_t \leq 1 \\ \sqrt{2} Q Q_s (\omega_r \sigma_t)^2, & \text{if } \omega_r \sigma_t \gg 1 \end{cases} \tag{4.1}$$

Plugging the parameters of Table 4.1 in Eq. (4.1), the CLIC DR bunch is in the regime of short bunch (first case) when $f_r \leq 26.53$ GHz. The impedance budget is estimated in simulation by considering the Q factor equal to 1 and scanning the resonator frequency from 0 to 30 GHz and the transverse shunt impedance from 0 to 30 MΩ/m.

The comparison between the instability threshold evaluated with Eq. (4.1) in the short bunch regime with the results of PyHEADTAIL simulations is shown in Fig. 4.1. The black vertical line indicates the limit of the short bunch regime region. The difference in the impedance thresholds in the two planes is explained by the difference in the average beta values over the DR used in this simulation for the broad-band resonator. It is noteworthy that the good agreement confirms the validity of the simulation tool.

In the following the cut-off frequency of the beam pipe ($f_r = 5$ GHz) is considered as resonator frequency and Q is assumed to be 1, while the transverse shunt impedance R_T will be the scanned parameter. This allows the calculation of the available transverse impedance budget that ensures safe operation with the designed bunch current with machine parameters reported in Table 4.1.

The PyHEADTAIL code provides the evolution of the bunch centroid over several turns for different transverse shunt impedance values. The values of R_T are scanned from 0 up to 20 MΩ/m with a step of 0.5 MΩ/m. In the top of Figure 4.2, the centroid horizontal position is plotted as a function of time for different values of the transverse shunt impedance R_T. The beam starts to be unstable in the horizontal plane for values higher than $R_T = 17.5$ MΩ/m. The vertical centroid is plotted in the bottom part of Fig. 4.2, in this plane the beam becomes clearly unstable at $R_T = 7$ MΩ/m.

The calculation of the growth rate (inverse of the rise time) is needed along with the comparison with the damping time (given in Table 4.1). If the growth rate is higher than the inverse of the damping time (0.5 ms^{-1} in both transverse planes), the damping mechanism is not able to suppress the instability. Top part of Fig. 4.3 shows the growth rate in the horizontal plane. For a value of shunt impedance of 17.5 MΩ/m the growth rate is lower than 0.5 ms^{-1}, so that the damping mechanism is able to suppress the instability. On the other hand the value of growth rate for $R_T = 18$ MΩ/m is higher than the damping threshold. Bottom part of Fig. 4.3 shows the vertical plane, where the instability occurs for $R_T = 7$ MΩ/m.

The behavior of the transverse modes is analyzed in the frequency domain by applying the Sussix algorithm [79, 80]. The spectrum of the bunch modes is obtained by applying this frequency analysis to the coherent bunch motion for each value of the transverse shunt impedance. The relative tune shift $(Q_{x,y} - Q_{x,y,0})/Q_s$ with respect to the zero-current tune $Q_{x,y,0}$ is normalized to the synchrotron tune Q_s to identify each of the bunch azimuthal modes. The lines in the bunch centroid spectrum represent the coherent oscillation frequencies of the bunch.

The tune shift is plotted as a function of the transverse shunt impedance in Fig. 4.4 for both planes. Modes 0 and −1 are observed to shift with increased R_T and couple for impedance values of about 18 MΩ/m and 7 MΩ/m in the horizontal and vertical plane respectively, causing a TMCI. As already said, the difference in the impedance thresholds in the two planes is explained by the difference in the average beta values $< \beta_{x,y} >$ over the DR used in the simulation for the BBR.

Up to now, the study was performed for zero chromaticity ($\xi_{x,y} = 0$). The chromaticity is expected to raise the TMCI threshold because it causes tune spread and locks the coherent modes to their low intensity values, making mode coupling potentially appear at higher impedance values. Simulations were performed for different positive and negative chromaticity values.

In Fig. 4.5, it is observed that in the case of slightly positive chromaticity ($\xi = 0.01$), modes ±1 get excited whereas mode 0 is damped. This shows that, as expected, the TMCI threshold is shifted to higher shunt impedance values, however a headtail instability is encountered. For negative chromaticity, shown in Fig. 4.6, the mode 0 becomes unstable.

The growth rate for different values of chromaticity is shown in Fig. 4.7 for the horizontal and vertical planes. The values of $\xi_{x,y}$ in simulation are varied from -0.1 up to 0.1 with a step of 0.01. As a first approximation, the damping rates were subtracted from the growth rates in the plot in order to account for the effect of synchrotron radiation (the synchrotron radiation effect is not yet included in the PyHEADTAIL simulations at this stage). For the sake of clarity, the results for the available impedance budget are stated in Table 4.2 for some values of chromaticity. The instability thresholds are even lower for slightly positive or negative chromaticity compared to the thresholds obtained for zero chromaticity. Therefore, the goal would be to operate the machine at zero chromaticity. However, in order to have some margin for operational conditions with non-perfect chromaticity correction, lower impedance budget has to be considered. The allowed impedance budget is therefore around 4.0 MΩ/m in both planes.

$\xi_{x,y}$	Threshold in x $[M\Omega/m]$	Threshold in y $[M\Omega/m]$
0	18.0	7.0
0.01	8.5	6.0
0.05	3.5	3.0
0.1	6.0	2.0
−0.01	5.0	5.5
−0.05	1.5	2.0
−0.1	1.5	1.0

Table 4.2: Instability thresholds for various positive and negative chromaticity values.

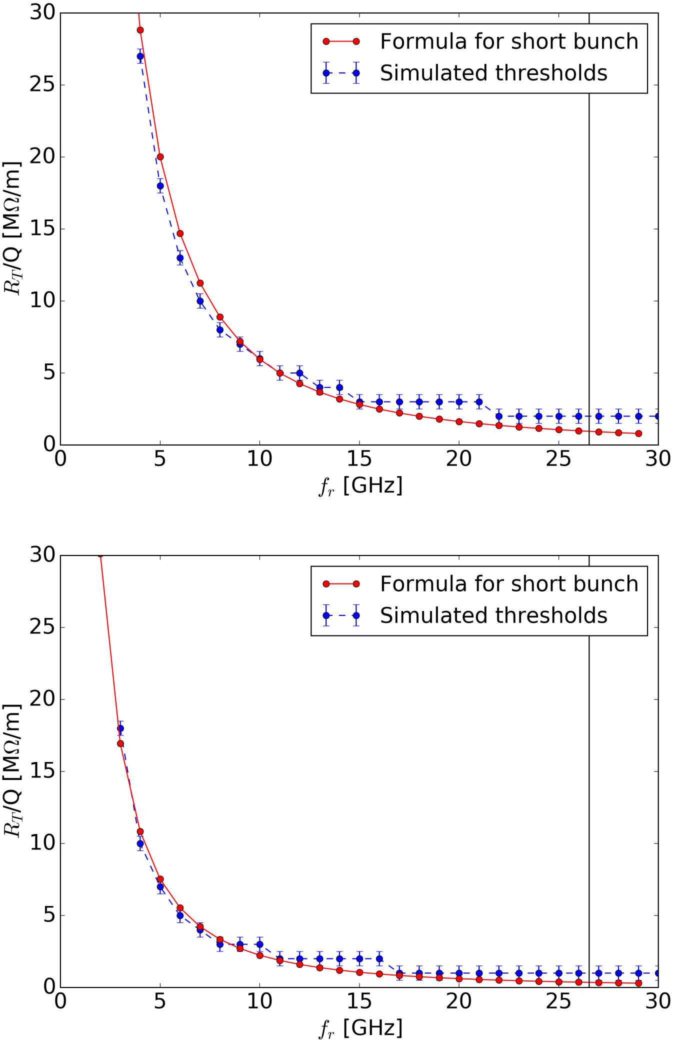

Figure 4.1: Threshold R_T/Q as function of the broad band resonator frequency f_r, as resulting from PyHEADTAIL simulations (blue points) in the horizontal (top) and vertical (bottom) planes. The theoretical line from Zotter's formula (red line) is also plotted.

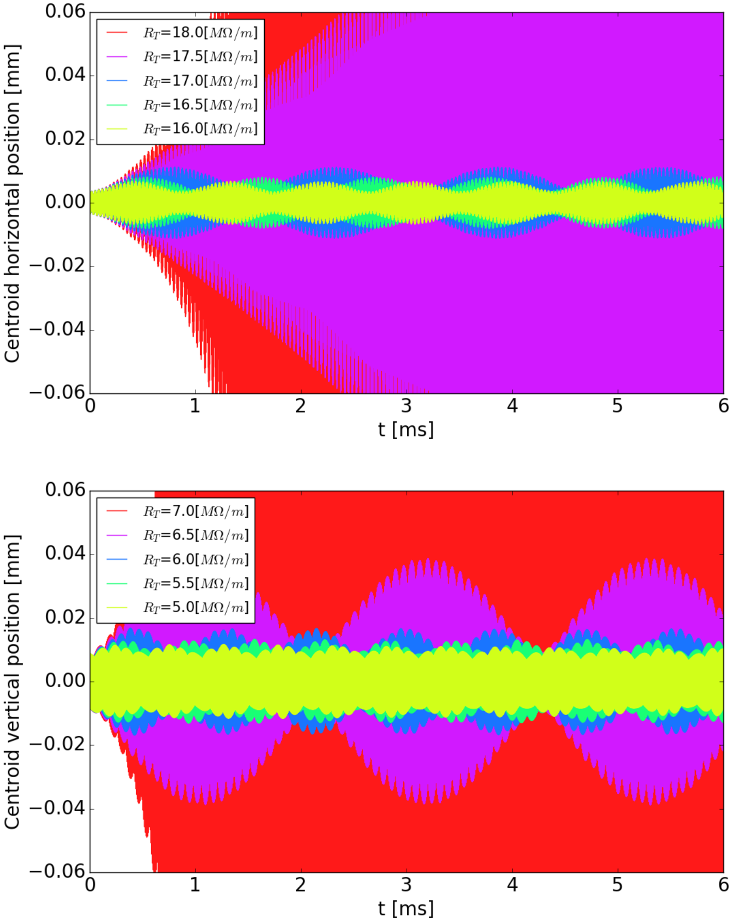

Figure 4.2: PyHEADTAIL simulated coherent horizontal (top) and vertical (bottom) motion of the bunch centroid as a function for different values of the transverse shunt impedance.

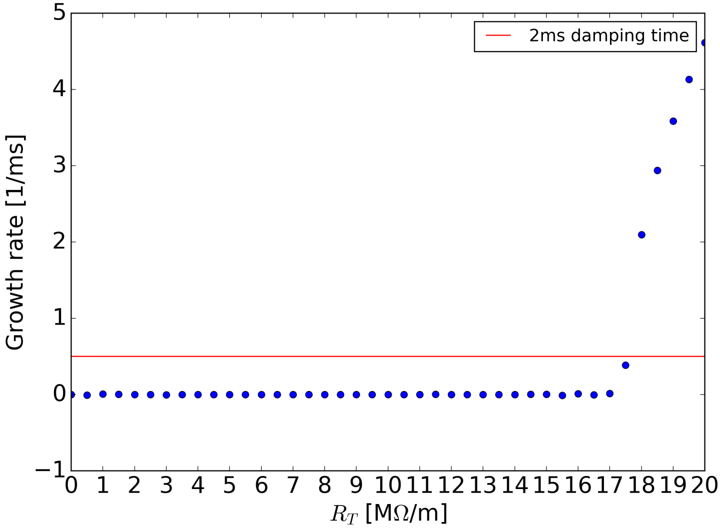

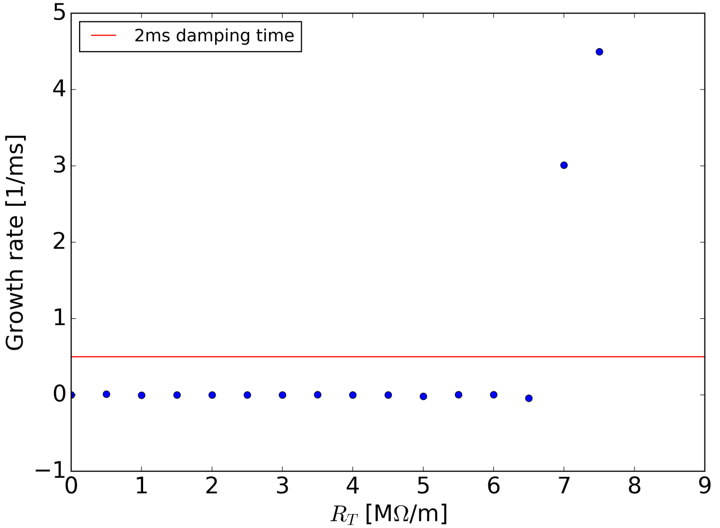

Figure 4.3: Growth rate in the horizontal (top) and vertical (bottom) planes. The damping time from synchrotron radiation (not taken into account in these simulations) is indicated by the red line.

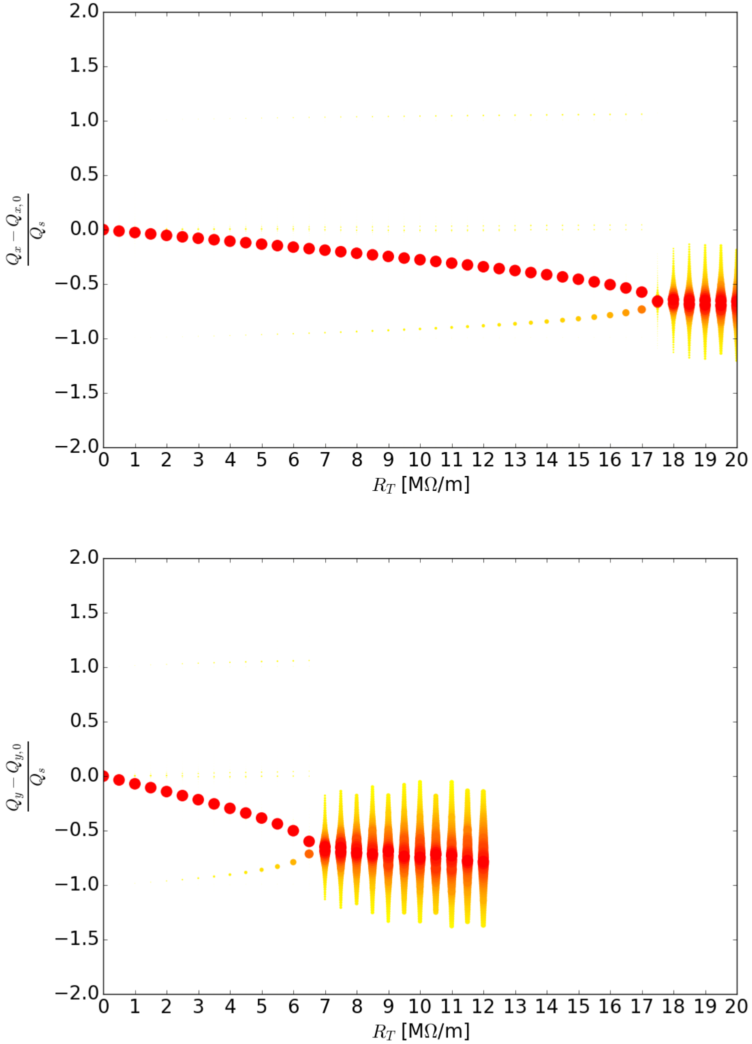

Figure 4.4: Mode spectrum of the horizontal (top) and vertical (bottom) coherent motion as function of the transverse shunt impedance (the size of the marker indicates the spectral power in the FFT).

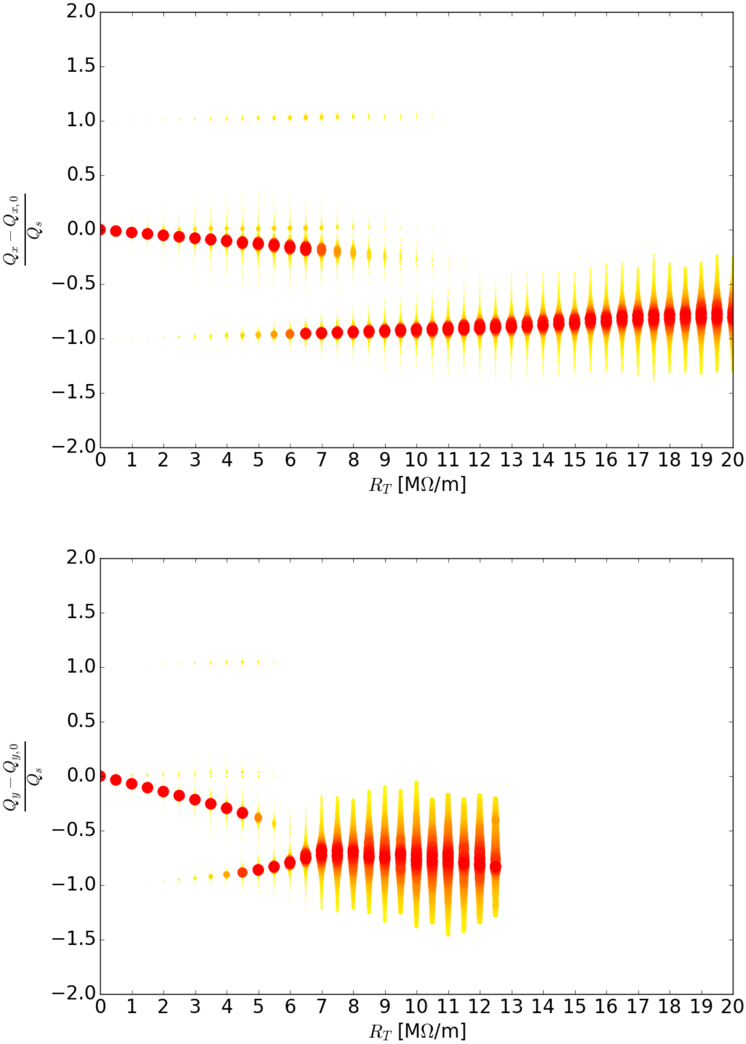

Figure 4.5: Mode spectrum of the horizontal (top) and vertical (bottom) coherent motion as function of the transverse shunt impedance for $\xi_x = 0.01$ (the size of the marker indicates the spectral power in the FFT).

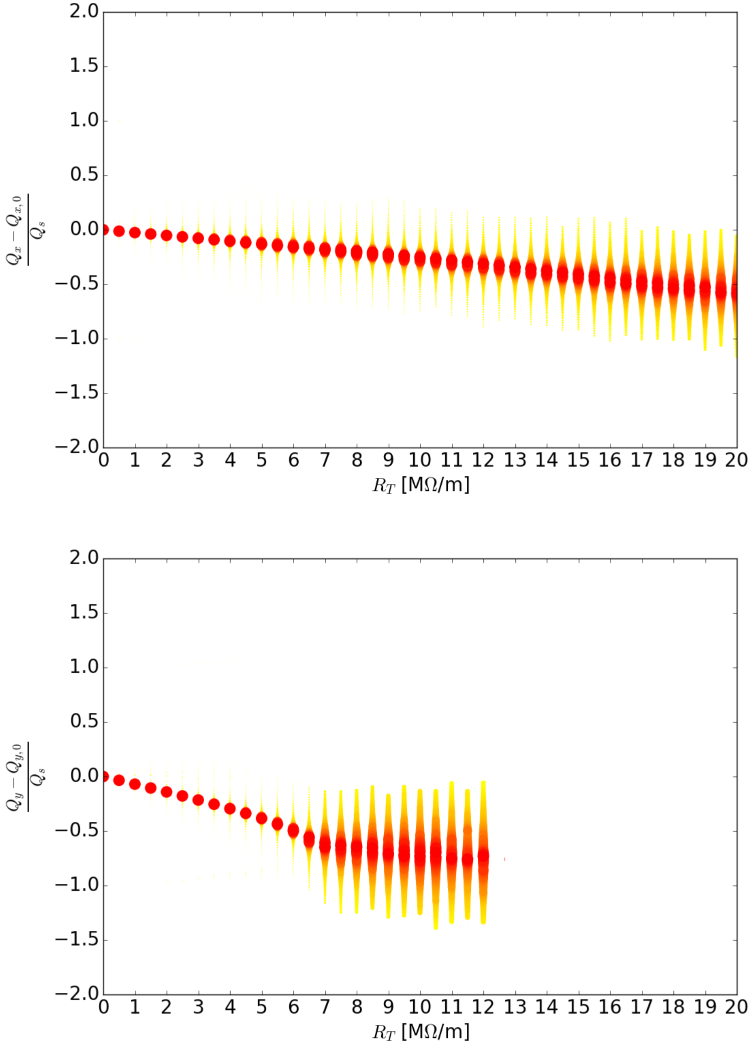

Figure 4.6: Mode spectrum of the horizontal (top) and vertical (bottom) coherent motion as function of the transverse shunt impedance for $\xi_x = -0.01$ (the size of the marker indicates the spectral power in the FFT).

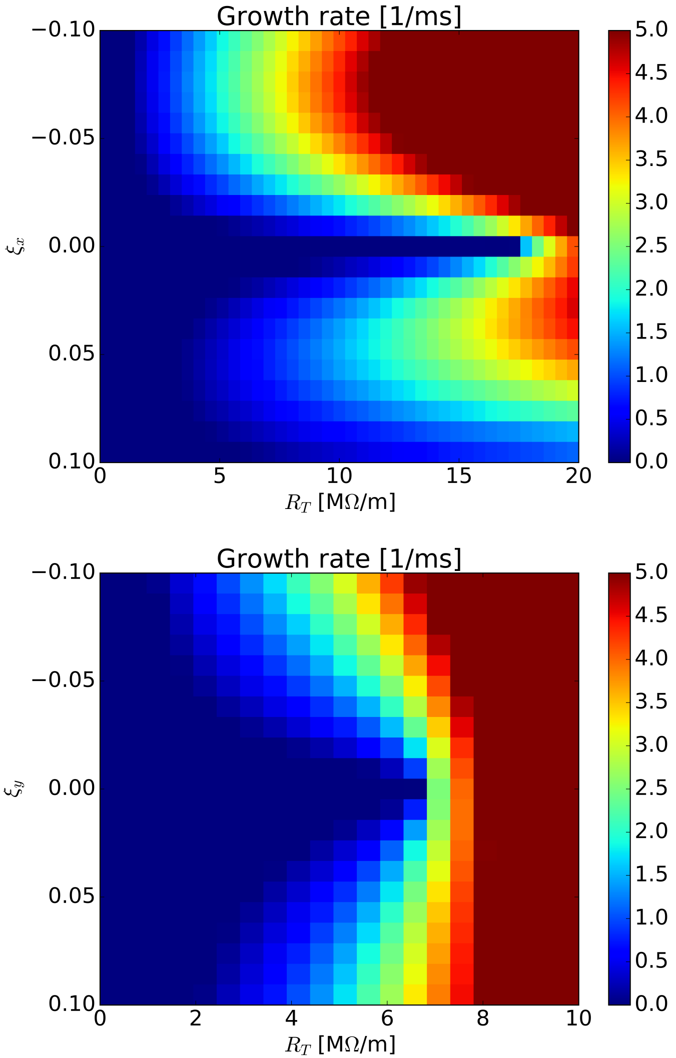

Figure 4.7: Growth rate in the horizontal (top) and vertical (bottom) planes for various values of chromaticity. The values shown are obtained after subtraction of the synchrotron radiation damping rate of $0.5\ ms^{-1}$ as a function of the BBR shunt impedance.

4.2.2 Synchrotron radiation effects

As already described in Sec. 2.2, when a particle emits radiation, the effect of transverse synchrotron radiation damping and quantum excitation have to be taken into account in the equation of motion (Eq. (2.35)). Figure 4.8 shows the effect of the synchrotron radiation on the centroid positions and normalized emittances in both planes resulting from PyHEADTAIL simulations. The agreement between the expected values of damping times and equilibrium emittances (reported in Table 4.1) and the ones evaluated by simulating the beam passing through the machine including synchrotron radiation is very good. It is important to underline that an initial kick to the beam has been given in order to highlight the synchrotron radiation effects.

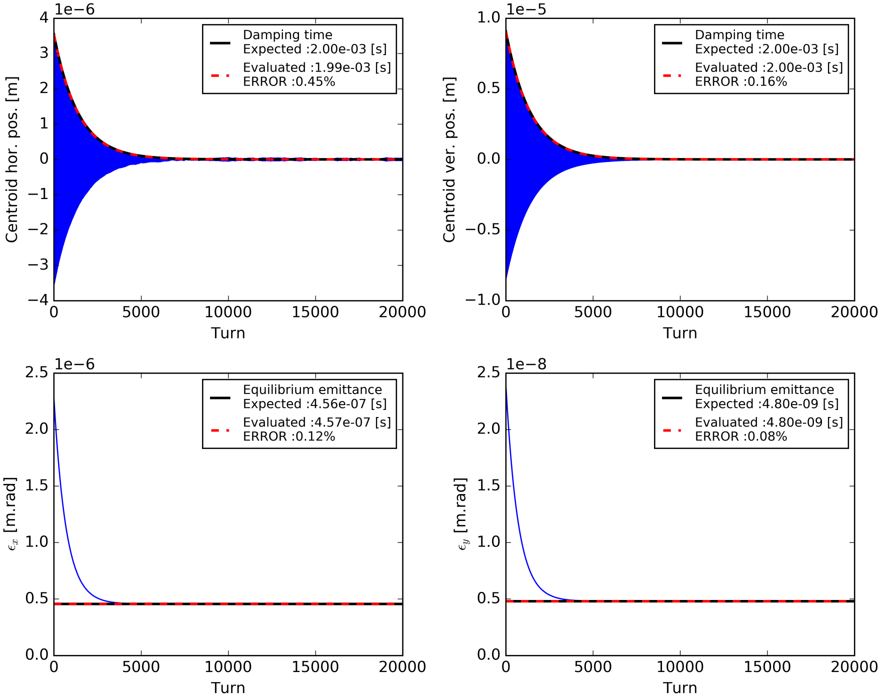

Figure 4.8: Coherent horizontal and vertical motion of the bunch centroid and normalized emittances as a function of simulated turns. The synchrotron radiation effects are shown and compared with expected values.

The effect of the synchrotron radiation has been added to the simulation model with the BBR impedance and the growth rate is shown in Fig. 4.9 for different values of chromaticity, both positive and negative. As in the case without synchrotron radiation effect, the values of $\xi_{x,y}$ are varied from -0.1 up to 0.1 with a step of 0.01. The plotted values can be compared to the ones shown in Fig. 4.7 (where the effect of synchrotron radiation was included as approximation by simply subtracting the radiation damping rate from the instability growth rate). The results for the available impedance budget are stated in Table 4.3 for some values of chromaticity and directly comparable with Table 4.2. The criterion to evaluate the instability threshold used in the section before is confirmed valid for negative and zero chromaticity, but not for positive chromaticity. This means that the criterion is valid when it is applied on mode 0 but not on modes ± 1. Synchrotron radiation improves transverse stability for positive chromaticity. If the machine operates with slightly positive chromaticity, the impedance budget is estimated to be in the order of 7.0 MΩ/m considering the effects of synchrotron radiation.

$\xi_{x,y}$	Threshold in x $[M\Omega/m]$	Threshold in y $[M\Omega/m]$
0	17.0	6.5
0.01	18.5	7.5
0.05	10.0	7.0
0.1	15.5	5.5
−0.01	6.5	5.5
−0.05	1.5	2.5
−0.1	1.5	1.5

Table 4.3: Available impedance budget for various positive and negative chromaticity values with the effect of synchrotron radiation included in the simulation.

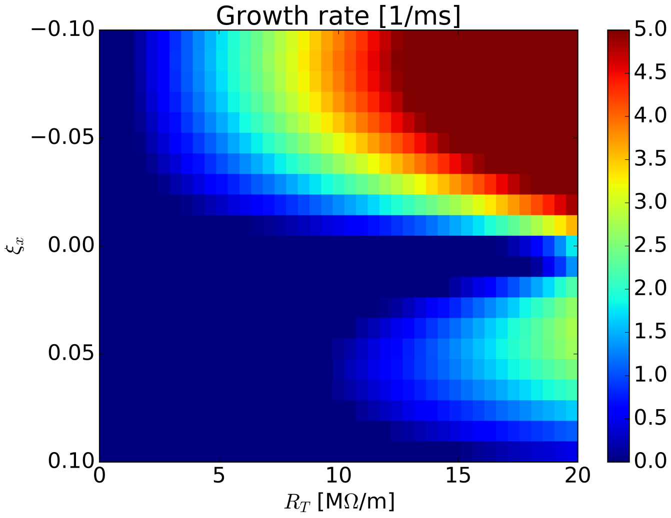

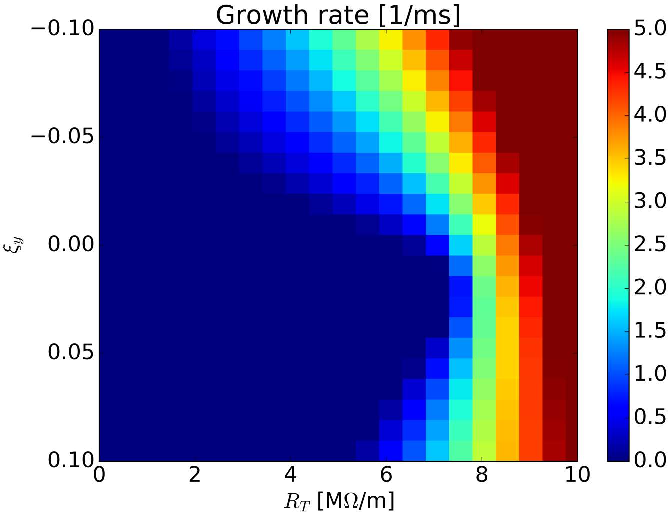

Figure 4.9: Growth rate in the horizontal (top) and vertical (bottom) planes for various values of chromaticity as a function of the BBR shunt impedance. Considering the synchrotron radiation effect.

4.2.3 Resistive wall

The resistive wall (RW) impedance of the machine vacuum chambers is another contributor in the CLIC DR model. As already written in Chapter 3, it is a common strategy for suppressing some undesired collective effects to use coating materials like the Amorphous Carbon (a-C) for the e-cloud mitigation [42, 81, 82] or the Non-Evaporated Getter (NEG) to reach the ultra-high vacuum condition in the chambers [83, 84]. The impact of coatings on the impedance budget has to be evaluated. For the design study of the CLIC DR lattice, the wake functions of the resistive wall impedance for three different contributions were calculated resorting to Eqs. (2.54) and (2.55) using the ImpedanceWake2D tool already described in Sec. 2.5.

The lattice used for this study is described in detail in [85]. In total there are 13 FODO cells in each of the two straight section with two wigglers per cell, thus the first component is made of the 52 wigglers of 2.5 T peak field with 6 mm half gap, flat geometry [86, 87] and $<\beta_x> = 4.200$ m, $<\beta_y> = 9.839$ m. The second component consists of 270.2 m of the arcs with a beam pipe of 9 mm of radius, round geometry [88] and $<\beta_x> = 2.976$ m, $<\beta_y> = 8.829$ m. The rest of the FODO cell is considered as a separate third contributor with a round geometry of the chamber and a radius of 9 mm and $<\beta_x> = 5.665$ m, $<\beta_y> = 8.582$ m. The three components are simulated as a two-layer structure made of Stainless Steel ($\sigma_{DC} = 1.45 \times 10^6$ S/m) and coated with 1 μm of a-C or 2 μm of NEG. The value of NEG conductivity is the one evaluated with the method described in Chapter 3 and its value is $\sigma_{coat} = 8 \times 10^5$ S/m, the conductivity used of the a-C is a conservative value of $\sigma_{DC} = 1 \times 10^3$ S/m. Regarding the thickness, in CERN machines it usually varies between $1-2$ μm for NEG and $0.5-1$ μm for a-C. We decided to simulate the worst case scenario for both two situations.

The RW effect together with the synchrotron radiation and the BBR has been simulated and the growth rate is shown in Fig. 4.10 for NEG coatings and in Fig. 4.11 for a-C coatings scanning different values of chromaticity, both positive and negative. The results for the available impedance budget remaining for the shunt impedance of the BBR are summarized in Table 4.4 for some values of chromaticity for both type of coatings.

As expected, the RW impedance reduces the transverse stability threshold in both planes and for all the chromaticity configurations. The effect of 2 μm of NEG is similar to the one with 1 μm of a-C. The final result is that, since the machine will work with a certainly slightly positive chromaticity, the impedance budget is estimated to be in the order of 2.5 MΩ/m limited by the vertical plane stability. Chapter 3 is devoted to the development of a new method for the electromagnetic characterization of coating materials in the frequency range of our interest (sub-THz). In particular, the NEG characterization is performed and the results are useful for a correct estimation of the instability threshold.

	NEG coating		a-C coating	
$\xi_{x,y}$	Thresh. x $[M\Omega/m]$	Thresh. y $[M\Omega/m]$	Thresh. x $[M\Omega/m]$	Thresh. y $[M\Omega/m]$
0	13.5	2.5	13.5	2.5
0.01	15.5	3,0	15.0	2.5
0.05	8.0	2.5	8.0	2.5
0.1	14.0	2.5	14.0	2.5
−0.01	4.5	2.0	4.5	2.5
−0.05	0.0	0.0	0.0	0.0
−0.1	0.0	0.0	0.0	0.0

Table 4.4: Available impedance budget for the BBR contribution for various positive and negative chromaticity values considering the RW effect both with NEG and a-C coatings.

4.3 Longitudinal impedance budget

In this section, the available impedance budget in the longitudinal plane is evaluated in order to ensure stable machine operation with the design parameters. First the longitudinal stability is studied in presence of a broad band impedance. In a second step the effect of synchrotron radiation is taken into account.

4.3.1 Broad-band resonator

As first step we assume the whole ring modeled as a broad-band resonator (BBR). The expression of the longitudinal wake function is stated in Eq. (2.53). The Boussard criterion (expected to be more correct for long bunches or coasting beam) can be used to roughly estimate the instability threshold when the impedance of a machine is simplified by considering a broad band resonator. This criterion for longitudinal microwave instability (or turbulent bunch lengthening) is given by the expression [25]:

$$|R_s| < 1.7\ln(2)Z_0\frac{|\eta|\gamma}{N_b r_0}\sigma_\delta^2\sigma_z \qquad (4.2)$$

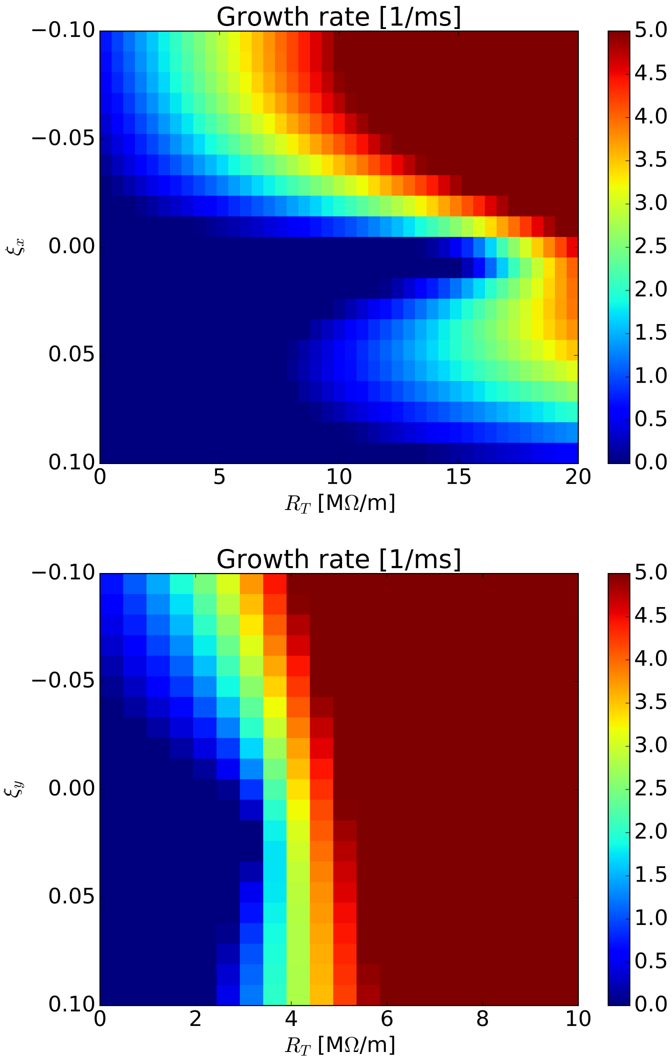

Figure 4.10: Growth rate in the horizontal (top) and vertical (bottom) planes for various values of chromaticity as a function of the BBR shunt impedance. Considering the effect of NEG coating.

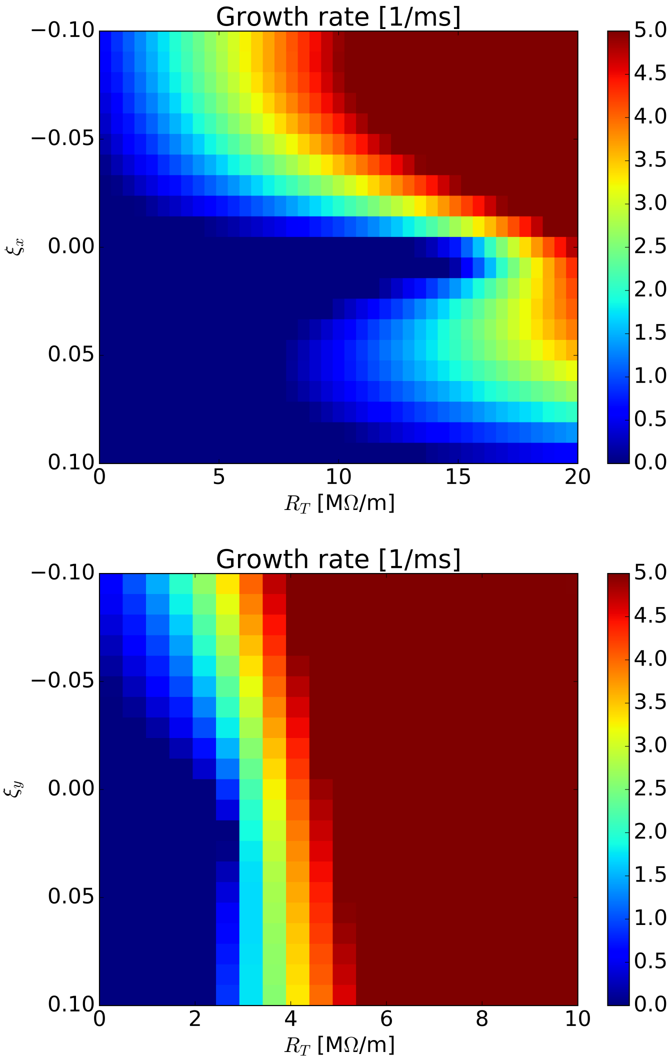

Figure 4.11: Growth rate in the horizontal (top) and vertical (bottom) planes for various values of chromaticity as a function of the BBR shunt impedance. Considering the effect of a-C coating.

where Z_0 is the vacuum impedance. Considering the DRs parameters from Table 4.1 and plugging them into the above formula, we obtain the expected threshold of microwave instability to be at around 0.056 Ω.

Instead, to determine whether we have bunch lengthening or shortening, we have to resort on the Haissinski equation. The sign of the second order term in the Taylor expansion of the second term in the exponential of the Eq. [25]:

$$\lambda(z) = \lambda_0 exp\left[-\frac{z^2}{2\sigma_z^2} - \frac{e^2}{m_e \gamma C \sigma_\delta^2 c^2 \eta}\int_0^z dz^{''}\int_{-\infty}^{\infty}\lambda\left(z^{'}\right)W_0^{'}\left(z^{''}-z^{'}\right)dz^{'}\right] \quad (4.3)$$

tells us that considering the spectrum of the CLIC DR bunch, the transition between the two regimes of bunch lengthening and shortening appears at around $\omega_r = 2\pi \times$ 32 GHz.

Bunch shape deformation has been studied for values of longitudinal shunt impedance from 0 to 0.1 Ω with a step of 0.01 Ω for a wide range of frequencies ω_r. Fig. 4.12 shows the bunch length behaviour as function of R_S for values of frequency from 18 to 23 GHz. The ”error bars” represent the rms amplitude of the bunch oscillation. The blue line indicates the expected microwave instability threshold. The transition from the bunch shortening to the bunch lengthening regime is determined by how much the bunch spectrum overlaps with the capacitive or the inductive part of the impedance respectively. The two different regimes are evident in Fig. 4.13, where the bunch length oscillation is shown for $\omega_r = 2\pi \times 18$ GHz and $\omega_r = 2\pi \times 23$ GHz, respectively. In the first case, increasing the impedance value the bunch tends to shorten, in the latter case it clearly becomes longer.

The simulated threshold occurs somewhere around $\omega_r = 2\pi \times 21$ GHz that is different from the predicted threshold with Haissinski equation of $\omega_r = 2\pi \times 32$ GHz. There is a discrepancy between the analytical and the numerical evaluations of the threshold between the bunch lengthening and shortening regime.

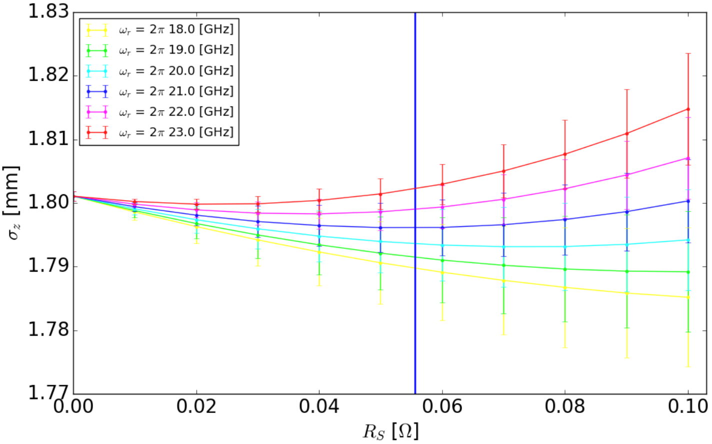

Figure 4.12: Bunch length as a function of the longitudinal impedance seen by the bunch for different values of the ω_r. The error bars represent the r.m.s. values of the bunch length oscillation.

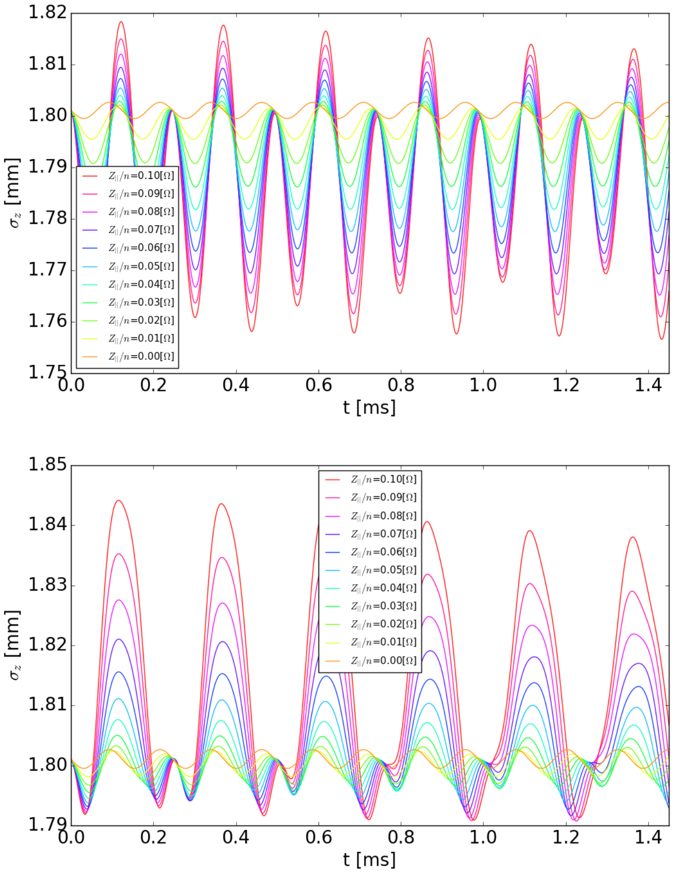

Figure 4.13: Bunch length (r.m.s.) evolution of a bunch subject to different impedances (different Rs as labelled) and $\omega_r = 2\pi \times 18$ GHz (top) or $\omega_r = 2\pi \times 23$ GHz (bottom).

4.3.2 Synchrotron radiation effects

The effects of synchrotron radiation have been implemented also in the longitudinal plane following the Eq. (2.36). Fig. (4.14) shows the synchrotron radiation effect on the longitudinal bunch centroid and bunch length (r.m.s.) evolution. The agreement between the expected values of damping time and equilibrium momentum spread (reported in Table 4.1) and the ones evaluated by simulating the beam passing through the machine with only the effect of synchrotron radiation is very good. Also in this case, the beam is kicked in order to highlight the damping effect of the synchrotron radiation. The energy lost each turn is 3.98 MeV, consistent with the expected value.

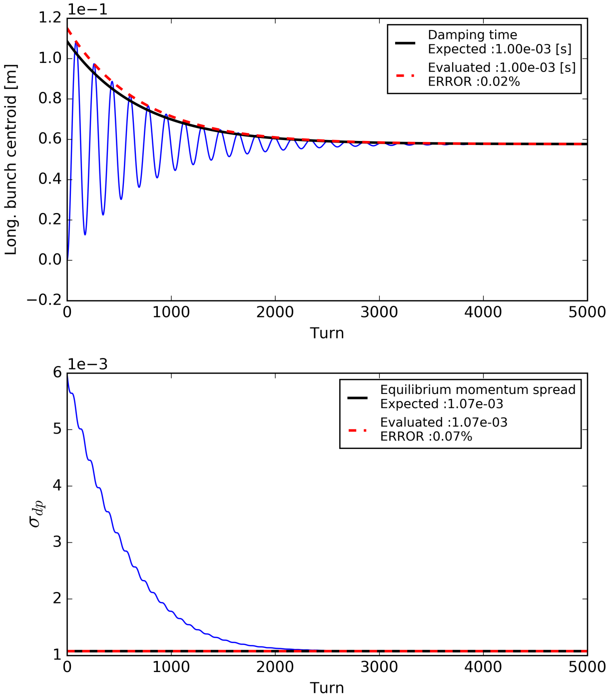

Figure 4.14: Longitudinal bunch centroid and bunch length (r.m.s.) evolution as a function of simulated turns. The synchrotron radiation effects are shown and compared with expected values.

The effect of the synchrotron radiation has been added to the simulation model with the BBR impedance. As in the case without synchrotron radiation effect, bunch shape deformation has been studied for values of longitudinal shunt impedance from 0 to 0.1 Ω with a step of 0.01 Ω for a wide range of frequencies ω_r. Fig. 4.15 shows the bunch length behaviour as function of R_S for values of frequency from 18 to 28 GHz. The simulated threshold between the bunch lengthening and shortening regime occurs somewhere around $\omega_r = 2\pi \times 24$ GHz that is different from the one simulated without synchrotron radiation effect of $\omega_r = 2\pi \times 21$ GHz (see Fig. 4.12). The two different regimes are evident in Fig. 4.16, where the bunch length oscillation is shown for the first and last case ($\omega_r = 2\pi \times 18$ GHz and $\omega_r = 2\pi \times 28$ GHz). The time scale is wider with respect to Fig. 4.13 in order to show the damping effect on the bunch length.

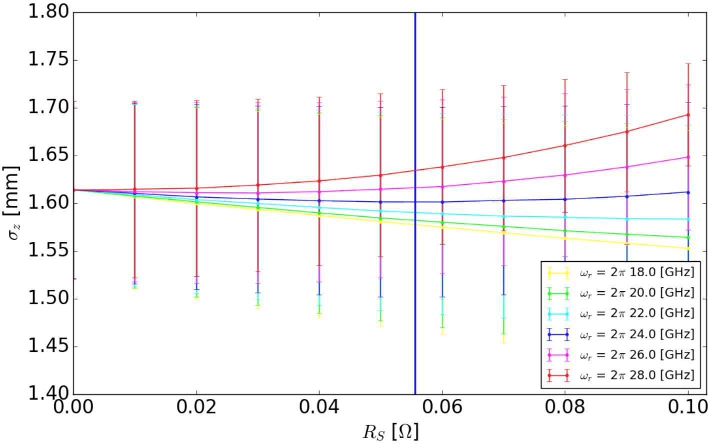

Figure 4.15: Bunch length as a function of the longitudinal impedance seen by the bunch for different values of the ω_r. Considering the synchrotron radiation effect. The error bars represent the r.m.s. values of the bunch length oscillation.

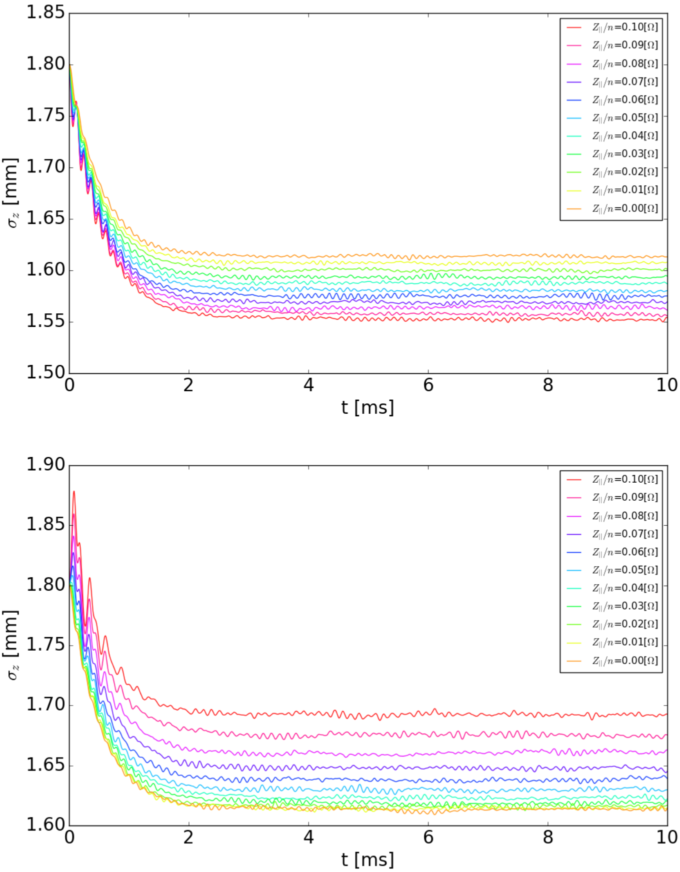

Figure 4.16: Bunch length (r.m.s.) evolution of a bunch subject to different impedances (different Rs as labelled) and $\omega_r = 2\pi \times 18$ GHz (top) or $\omega_r = 2\pi \times 28$ GHz (bottom). Considering the synchrotron radiation effect.

Conclusion and Outlook

The goal of this thesis has been to build a reliable impedance model of the CLIC Damping Rings. The main task was the study of the coating effect with emphasis on their electromagnetic characterization at high frequencies.

For a realistic evaluation of the resistive wall contribution, we developed a novel electromagnetic characterization system for time domain measurements that allows the assessment of the surface impedance of materials used for coatings in accelerator beam pipes in a fairly broad frequency window in the sub-THz range. Unlike frequency domain measurements, the developed method allows to evaluate the electromagnetic properties of the sample under test in a simple and handy way. The advantages of this setup, based on a tailored waveguide with a central coated slab, are mainly the possibility to characterize uniform samples and the reusability of the Device Under Test for different coating materials. The experimental analysis is based on an ad-hoc developed analytical method in order to evaluate the signal attenuation of the transmitted electromagnetic wave. This analytical model is robust as demonstrated by the agreement between the theoretical evaluation and the numerical solution, performed with Frequency Domain solver of CST Microwave Studio module. These time domain measurements allowed the conductivity estimation of the NEG coating. The two samples of the iron waveguide yield the same value within the error bar given by the best-fit procedure. The result of $\sigma_{\text{coat}} = (8.2 \pm 0.6) \times 10^5$ S/m agrees well with previous data obtained with the frequency domain approach. It is important to underline that the results obtained by using the copper and the stainless steel waveguides show the importance of the compliance with requested machining tolerances. The stainless steel waveguide does not allow proper measurements because of multiple unwanted reflection inside the device and in the copper waveguide, the discrepancy between the real geometry of the DUT and the one assumed in the analytical evaluation does not allow to provide a reliable evaluation of the NEG conductivity. Using the determined σ_{coat} we evaluated the real part of the surface impedance as a function of frequency for relatively large area samples, which is used for modelling the impedance in modern accelerators.

The value of the effective NEG conductivity has been implemented in the ImpedanceWake2D simulations in order to evaluate the resistive wall impedance for the wigglers, arcs and FODO cells simulated as two-layer structures made of

Stainless Steel and coated with 2 μm NEG. These simulations underlined the importance of performing material characterization at high frequencies as fundamental for the correct estimation of the contribution of coatings to the total impedance budget.

In order to assess the CLIC DRs impedance budget in the transverse plane, the entire ring impedance has been modeled using the contributions of broad-band resonator and the resistive wall of three different components (wigglers, arcs, other FODO elements). The radiation damping and the quantum excitation effects due to the synchrotron radiation emission have been implemented in the beam dynamics code and taken into account in the final evaluation of the impedance budget. The beam dynamics simulations, performed for different values of chromaticity, gave an estimated transverse impedance budget of the order of 3.0 MΩ/m limited by the vertical stability when the chromaticity $\xi_{x,y}$ is slightly positive between 0.01 and 0.05.

In the longitudinal plane, the effect of a BBR and of the synchrotron radiation has been studied. The threshold between the bunch lengthening and shortening regime is at around $\omega_r = 2\pi \times 24$ GHz.

The final impedance model should include also the effect of the devices such as the strip-line kickers, RF-cavities and devices for beam instrumentation and diagnostic. The impedance of such complex structures could not be evaluated because actual 3D codes would require billions of mesh-cells to simulate very small excitation, to determine short range wakes, necessary in the CLIC DRs regime. With the current simulation codes, the wake function calculation cannot be considered reliable even with the support of a computer cluster.

The full potential of the measurement method for evaluating the impedance of coatings developed in this thesis could not yet be exploited. To this end, a new agreement in the framework of the CERN-INFN collaboration is being established to continue this work. This will allow the signal generator upgrade by improving the spectral resolution and signal-to-noise ratio and a more accurate manufacturing of the guiding systems, in order to have the requested machine tolerances for all the devices. The next step will be the characterization of different coating materials, like amorphous carbon (a-C) or Laser Engineered Surface Structures (LESS) currently in use in the more recent accelerators and light sources.

List of Figures

List of Tables

Lists of Abbreviations

a-C Amorphous Carbon

BBR Broad Band Resonator

BDS Beam Delivery Section

CERN European Organization for Nuclear Research

CLIC Compact LInear Collider

DRs Damping Rings

DUT Device Under Test

EC Electron Cloud

EMC Electromagnetic Characterization

FCC Future Circular Collider

FD Frequency Domain

FFT Fast Fourier Transform

GeV Giga-electron-volt

ILC International Linear Collider

INFN Istituto Nazionale di Fisica Nucleare

IP Interaction Point

IW2D ImpedanceWake2D

LEP Large Electron-Positron Collider

LESS Laser Engineered Surface Structures

LHC Large Hadron Collider

NEG	Non Evaporable Getter
PDR	Pre-Damping Ring
RF	Radio Frequency
RW	Resistive Wall
SEY	Secondary Electron Yield
SPS	Super Proton Synchrotron
SR	Synchrotron Radiation
SSS	Short Straight Section
StSt	Stainless Steel
TDS	Time Domain Spectrometer
TE	Transverse Electric
TeV	Tera-electron-volt
TM	Transverse Magnetic
TMCI	Transverse Mode Coupling Instability
TPX	Polymethylpentene
VNA	Vector Network Analyzer
XRF	X-ray fluorescence

Bibliography

[1] L. Linssen, A. Miyamoto, M. Stanitzki, and H. Weerts, “Physics and Detectors at CLIC: CLIC Conceptual Design Report,” no. CERN-2012-003, 2012.

[2] T. K. Charles *et al.*, “The Compact Linear e^+e^- Collider (CLIC) - 2018 Summary Report,” 2018.

[3] M. Aicheler, P. Burrows, M. Draper, T. Garvey, P. Lebrun, K. Peach, N. Phinney, H. Schmickler, D. Schulte, and N. Toge, “A Multi-TeV Linear Collider Based on CLIC Technology: CLIC Conceptual Design Report,” Tech. Rep. CERN-2012-007. SLAC-R-985. KEK-Report-2012-1. PSI-12-01. JAI-2012-001, Geneva, 2012.

[4] J. de Blas *et al.*, “The CLIC Potential for New Physics,” 2018.

[5] C. Adolphsen, M. Barone, B. Barish, K. Buesser, P. Burrows, J. Carwardine, J. Clark, H. Mainaud Durand, G. Dugan, E. Elsen, *et al.*, “The International Linear Collider Technical Design Report - Volume 3.II: Accelerator Baseline Design,” 2013.

[6] L. Evans and S. Michizono, “The International Linear Collider Machine Staging Report 2017,” 2017.

[7] M. J. Boland *et al.*, “Updated baseline for a staged Compact Linear Collider,” 2016.

[8] H. Abramowicz *et al.*, “Higgs physics at the CLIC electron–positron linear collider,” *Eur. Phys. J.*, vol. C77, no. 7, p. 475, 2017.

[9] Y. Papaphilippou, “Conceptual design of the CLIC damping rings,” *ICFA Beam Dyn. Newslett.*, vol. 57, pp. 57–70, 2012.

[10] Y. Papaphilippou, “Status of the CLIC Damping Rings Design,” *ICFA Beam Dyn. Newslett.*, vol. 62, pp. 124–137, 2013.

[11] S. Y. Lee, *Accelerator physics; 3rd ed.* Singapore: World Scientific, 2012.

[12] K. Wille, *The physics of particle accelerators: an introduction*. Oxford: Oxford Univ. Press, 2000.

[13] E. J. N. Wilson, *An introduction to particle accelerators*. 2001.

[14] H. Wiedemann, *Particle accelerator physics; 4th ed.* Berlin: Springer, 2015.

[15] A. Wolski, “Low-emittance storage rings,” in *CAS - CERN Accelerator School: Advanced Accelerator Physics Course: Trondheim, Norway, August 18-29, 2013*, pp. 245–294, 2014.

[16] Riccardo Bartolini, “Comparison simulations-measurements of single bunch instabilities at diamond.” URL: `https://indico.cern.ch/event/277919/contributions/626941/attachments/506929/699857/RB_2014_01_17.pdf`, TWIICE Workshop 2014.

[17] L. Palumbo, V. G. Vaccaro, and M. Zobov, “Wake fields and impedance,” in *Advanced accelerator physics. Proceedings, 5th Course of the CERN Accelerator School, Rhodos, Greece, September 20-October 1, 1993. Vol. 1, 2*, pp. 331–390, 1994.

[18] C. Zannini, *Electromagnetic Simulation of CERN accelerator Components and Experimental Applications*. PhD thesis, CERN, 2013-03-11.

[19] K. Y. Ng, *Physics of intensity dependent beam instabilities*. 2006.

[20] L. Palumbo and V. G. Vaccaro, “Wake field: impedances and Green’s function,” 1987.

[21] V. G. Vaccaro, “Longitudinal instability of a coasting beam above transition, due to the action of lumped discontinuities,” Tech. Rep. CERN-ISR-RF-66-35. ISR-RF-66-35, CERN, Geneva, Nov 1966.

[22] A. M. Sessler and V. G. Vaccaro, *Longitudinal instabilities of azimuthally uniform beams in circular vacuum chambers with walls of arbitrary electrical properties*. Geneva: CERN, 1967.

[23] B. Zotter, “The Effective Coupling Impedance for Instabilities of Gaussian Bunches,” 1980.

[24] B. Zotter, “The Effective Coupling Impedance for Bunched Beam Instabilities,” 1978.

[25] A. W. Chao, *Physics of collective beam instabilities in high energy accelerators*. New York, NY: Wiley, 1993.

[26] F. Roncarolo, F. Caspers, T. Kroyer, E. Metral, N. Mounet, B. Salvant, and B. Zotter, “Comparison between laboratory measurements, simulations, and analytical predictions of the transverse wall impedance at low frequencies,” *Phys. Rev. ST Accel. Beams*, vol. 12, p. 084401, 2009.

[27] N. Mounet, *The LHC Transverse Coupled-Bunch Instability*. PhD thesis, Ecole Polytechnique, Lausanne, 2012-03-16.

[28] N. Mounet and E. Métral, “Impedances of two dimensional multilayer cylindrical and flat chambers in the non-ultrarelativistic case,” *Proceedings of HB2010*, pp. 353 – 357, 2010.

[29] K. Li, H. Bartosik, G. Iadarola, A. Oeftiger, A. Passarelli, A. Romano, G. Rumolo, M. Schenk, and S. Hegglin, “Code development for collective effects,” in *ICFA Advanced Beam Dynamics Workshop on High-Intensity and High-Brightness Hadron Beams (HB2016)*, 2016.

[30] G. Van Rossum *et al.*, “Python programming language.,” in *USENIX Annual Technical Conference*, vol. 41, p. 36, 2007.

[31] E. Métral, T. Argyropoulos, H. Bartosik, N. Biancacci, X. Buffat, J. F. E. Muller, W. Herr, G. Iadarola, A. Lasheen, K. Li, A. Oeftiger, T. Pieloni, D. Quartullo, G. Rumolo, B. Salvant, M. Schenk, E. Shaposhnikova, C. Tambasco, H. Timko, C. Zannini, A. Burov, D. Banfi, J. Barranco, N. Mounet, O. Boine-Frankenheim, U. Niedermayer, V. Kornilov, and S. White, “Beam instabilities in hadron synchrotrons,” *IEEE Transactions on Nuclear Science*, vol. 63, pp. 1001–1050, April 2016.

[32] M. Schenk, A. Grudiev, K. Li, and K. Papke, “Analysis of transverse beam stabilization with radio frequency quadrupoles,” *Phys. Rev. Accel. Beams*, vol. 20, p. 104402, Oct 2017.

[33] G. Rumolo and F. Zimmermann, “Practical user guide for HEADTAIL,” tech. rep., CERN-SL-Note-2002-036-AP, 2002.

[34] N.Mounet, “ImpedanceWake2D manual.” `http://impedance.web.cern.ch/impedance/Codes/ImpedanceWake2D/user_manual_todate.txt`.

[35] B. Zotter, “Longitudinal instabilities of charged particle beams inside cylindrical walls of finite thickness,” *Part. Accel.*, vol. 1, pp. 311–326, 1970.

[36] E. Keil and B. Zotter, “The impedance of layered vacuum chambers,” in *Particle accelerator. Proceedings, 6th European conference, EPAC’98, Stockholm, Sweden, June 22-26, 1998. Vol. 1-3*, pp. 963–965, 1998.

[37] B. W. Zotter, “New Results on the Impedance of Resistive Metal Walls of Finite Thickness,” Tech. Rep. CERN-AB-2005-043, CERN, Geneva, Aug 2005.

[38] N. Mounet and E. Métral, “Electromagnetic fields and beam coupling impedances in a multilayer flat chamber,” Dec 2010.

[39] M. Furman, “Electron Cloud Effects in Accelerators,” p. 8 p, Oct 2013. Comments: 8 pages, contribution to the Joint INFN-CERN-EuCARD-AccNet Workshop on Electron-Cloud Effects: ECLOUD’12; 5-9 Jun 2012, La Biodola, Isola d’Elba, Italy.

[40] G. Rumolo, F. Ruggiero, and F. Zimmermann, “Simulation of the electron-cloud build up and its consequences on heat load, beam stability, and diagnostics,” *Phys. Rev. ST Accel. Beams*, vol. 4, p. 012801, Jan 2001.

[41] R. Cimino, L. A. Gonzalez, R. Larciprete, A. Di Gaspare, G. Iadarola, and G. Rumolo, “Detailed investigation of the low energy secondary electron yield of technical Cu and its relevance for the LHC,” *Phys. Rev. ST Accel. Beams*, vol. 18, p. 051002, May 2015.

[42] C. Yin Vallgren, G. Arduini, J. Bauche, S. Calatroni, P. Chiggiato, K. Cornelis, P. C. Pinto, B. Henrist, E. Métral, H. Neupert, G. Rumolo, E. Shaposhnikova, and M. Taborelli, “Amorphous carbon coatings for the mitigation of electron cloud in the cern super proton synchrotron,” *Phys. Rev. ST Accel. Beams*, vol. 14, p. 071001, Jul 2011.

[43] M. Taborelli, P. Chiggiato, P. Costa Pinto, and P. Cruikshank, “Nine years of carbon coating development for the SPS upgrade: achievements and heritage.,” Tech. Rep. CERN-ACC-2016-0010, CERN, Geneva, Dec 2015.

[44] M. Palmer *et al.*, “Electron Cloud at Low Emittance in CesrTA,” 2010.

[45] C. Benvenuti, R. Calder, and O. Gröbner, “Vacuum for particle accelerators and storage rings,” *Vacuum*, vol. 37, pp. 699–707. 32 p, Dec 1987.

[46] C. Benvenuti, P. Chiggiato, F. Cicora, and V. Ruzinov, “Decreasing surface outgassing by thin film getter coatings,” *Vacuum*, vol. 50, no. 1-2, pp. 57–63, 1998.

[47] P. Costa Pinto, J. Ahlbäck, E. Al-Dmour, B. Bártová, M. Grabski, B. Holliger, S. Marques Dos Santos, V. Nistor, C. Pasquino, A. Sapountzis, M. Taborelli, and I. Wevers, "Development and Production of Non-evaporable Getter Coatings for MAX IV," no. CERN-ACC-2015-231, p. WEPHA019. 3 p, 2015.

[48] M. Migliorati, E. Belli, and M. Zobov, "Impact of the resistive wall impedance on beam dynamics in the future circular e^+e^- collider," *Phys. Rev. Accel. Beams*, vol. 21, p. 041001, Apr 2018.

[49] L.-F. Chen, C. Ong, C. Neo, V. Varadan, and V. K. Varadan, *Microwave electronics: measurement and materials characterization*. John Wiley & Sons, 2004.

[50] A. R. Von Hippel, *Dielectric materials and applications*, vol. 2. Artech House on Demand, 1954.

[51] A. Hernandez, E. Martin, J. Margineda, and J. M. Zamarro, "Resonant cavities for measuring the surface resistance of metals at x-band frequencies," *Journal of Physics E: Scientific Instruments*, vol. 19, no. 3, p. 222, 1986.

[52] M. W. Hyde, M. J. Havrilla, and P. E. Crittenden, "A novel method for determining the r-card sheet impedance using the transmission coefficient measured in free-space or waveguide systems," *IEEE Transactions on Instrumentation and Measurement*, vol. 58, pp. 2228–2233, July 2009.

[53] J. Booth, D. H. Wu, and S. M. Anlage, "A broadband method for the measurement of the surface impedance of thin films at microwave frequencies," *Review of scientific instruments*, vol. 65, no. 6, pp. 2082–2090, 1994.

[54] R. Wu and M. Qian, "A simplified power transmission method used for measuring the complex conductivity of superconducting thin films," *Review of scientific instruments*, vol. 68, no. 1, pp. 155–158, 1997.

[55] L. Angrisani, G. Cavallo, A. Liccardo, G. P. Papari, and A. Andreone, "Thz measurement systems," in *New Trends and Developments in Metrology* (L. Cocco, ed.), ch. 2, Rijeka: IntechOpen, 2016.

[56] G. P. Kniffin and L. M. Zurk, "Model-based material parameter estimation for terahertz reflection spectroscopy," *IEEE Transactions on Terahertz Science and Technology*, vol. 2, pp. 231–241, March 2012.

[57] M. Theuer and J. S. Melinger, "High resolution waveguide terahertz time-domain spectroscopy," *Journal of Infrared, Millimeter, and Terahertz Waves*, vol. 32, pp. 1267–1284, Nov 2011.

[58] M. Razanoelina, R. Kinjo, K. Takayama, I. Kawayama, H. Murakami, D. M. Mittleman, and M. Tonouchi, "Parallel-plate waveguide terahertz time domain spectroscopy for ultrathin conductive films," *Journal of Infrared, Millimeter, and Terahertz Waves*, vol. 36, pp. 1182–1194, Dec 2015.

[59] A. Khachatrian, J. S. Melinger, and S. B. Qadri, "Waveguide terahertz time-domain spectroscopy of ammonium nitrate polycrystalline films," *Journal of Applied Physics*, vol. 111, no. 9, p. 093103, 2012.

[60] E. Koukovini-Platia, G. Rumolo, and C. Zannini, "Electromagnetic characterization of nonevaporable getter properties between 220–330 and 500–750 GHz for the Compact Linear Collider damping rings," *Phys. Rev. Accel. Beams*, vol. 20, p. 011002, Jan 2017.

[61] E. Koukovini Platia, L. Rivkin, and G. Rumolo, *High Frequency Effects of Impedances and Coatings in the CLIC Damping Rings*. PhD thesis, 2015. presented 25 Sep 2015.

[62] "CST Dassault Systèmes Simulia." `http://www.cst.com`.

[63] J. F. Johansson and N. D. Whyborn, "The diagonal horn as a sub-millimeter wave antenna," *IEEE Transactions on Microwave Theory and Techniques*, vol. 40, pp. 795–800, May 1992.

[64] S. Silver, *Microwave antenna theory and design*. Electromagnetic waves, Stevenage: IET, 1983.

[65] C. S. Lee, S. W. Lee, and S. L. Chuang, "Plot of modal field distribution in rectangular and circular waveguides," *IEEE Transactions on Microwave Theory and Techniques*, vol. 33, pp. 271–274, Mar 1985.

[66] N. Marcuvitz, *Waveguide handbook*. IEE Electromag. Waves, London: Peregrinus, 1986.

[67] R. Mendis and D. M. Mittleman, "Comparison of the lowest-order transverse-electric (te1) and transverse-magnetic (tem) modes of the parallel-plate waveguide for terahertz pulse applications," *Opt. Express*, vol. 17, pp. 14839–14850, Aug 2009.

[68] G. Franceschetti, *Electromagnetics: Theory, Techniques, and Engineering Paradigms*. Springer Science and Business Media New York, Springer US, 1997.

[69] B. S. Guru and H. R. Hiziroglu, *Electromagnetic field theory fundamentals*. Cambridge university press, 2009. Eq. 9.64 pag. 444.

[70] A. Passarelli, H. Bartosik, G. Rumolo, V. G. Vaccaro, M. R. Masullo, C. Koral, G. P. Papari, A. Andreone, and O. Boine-Frankenheim, "Novel measurement technique for the electromagnetic characterization of coating materials in the sub-THz frequency range," *Phys. Rev. Accel. Beams*, vol. 21, p. 103101, Oct 2018.

[71] W. Withayachumnankul and M. Naftaly, "Fundamentals of measurement in terahertz time-domain spectroscopy," *Journal of Infrared, Millimeter, and Terahertz Waves*, vol. 35, pp. 610–637, Aug 2014.

[72] W. H. Press, S. A. Teukolsky, W. T. Vetterling, and B. P. Flannery, *Numerical recipes 3rd edition: The art of scientific computing*. Cambridge university press, 2007.

[73] E. Hammerstad and O. Jensen, "Accurate models for microstrip computer-aided design," in *1980 IEEE MTT-S International Microwave symposium Digest*, pp. 407–409, May 1980.

[74] A. E. Prodromides and F. Levy, *Non-Evaporable Getter Thin Film Coatings for Vacuum Applications*. PhD thesis, 2002. Presented on 1 Sep 2002, pp 95-96.

[75] A. Grudiev, "Conceptual Design of the CLIC Damping Ring RF System," *Conf. Proc.*, vol. C1205201, pp. 1870–1872, 2012.

[76] "CLIC DR collaboration page." `https://twiki.cern.ch/twiki/bin/view/CLIC/DampingRings`.

[77] B. Zotter, "Transverse mode coupling and Head-tail turbulence," 1982.

[78] G. Rumolo, "Beam Instabilities," no. arXiv:1601.05201, p. 21 p, 2014. Comments: 21 pages, contribution to the CAS - CERN Accelerator School: Advanced Accelerator Physics Course, Trondheim, Norway, 18-29 Aug 2013.

[79] R. Bartolini and F. Schmidt, "SUSSIX: A computer code for frequency analysis of nonlinear betatron motion," in *Nonlinear and stochastic beam dynamics in accelerators: A challenge to theoretical and computational physics. Proceedings, Workshop, Lueneburg, Germany, September 29-October 3, 1997*, pp. 390–394, 1997.

[80] R. Bartolini and F. Schmidt, “Normal form via tracking or beam data,” *Part. Accel.*, vol. 59, no. LHC-Project-Report-132, pp. 93–106, 1997.

[81] C. Yin Vallgren, *Low secondary electron yield carbon coatings for electron cloud mitigation in modern particle accelerators*. PhD thesis, Chalmers U. Tech., 2011.

[82] Y. Zhang, X. Ge, S. Wang, Y. Wang, W. Wei, and B. Zhang, “Production and Secondary Electron Yield Test of Amorphous Carbon Thin Film,” in *Proceedings, 9th International Particle Accelerator Conference (IPAC 2018): Vancouver, BC Canada*, p. THPML128, 2018.

[83] P. Manini, A. Bonucci, A. Conte, and S. Raimondi, “Deposition of non evaporable getter (NEG) films on vacuum chambers for high energy machines and synchrotron radiation sources,” *Conf. Proc.*, vol. C060626, pp. 1435–1437, 2006. [,1435(2006)].

[84] C. Garion and H. Kos, “Design of the CLIC Quadrupole Vacuum Chambers,” in *Particle accelerator. Proceedings, 23rd Conference, PAC’09, Vancouver, Canada, May 4-8, 2009*, p. MO6RFP007, 2010.

[85] F. Antoniou, *Optics design of Intrabeam Scattering dominated damping rings*. PhD thesis, CERN, 2012.

[86] D. Schoerling *et al.*, “Design and system integration of the superconducting wiggler magnets for the Compact Linear Collider damping rings,” *Phys. Rev. ST Accel. Beams*, vol. 15, p. 042401, 2012.

[87] D. Schoerling, *Superconducting wiggler magnets for beam-emittance damping rings*. PhD thesis, CERN, 2012.

[88] S. Papadopoulou, F. Antoniou, and Y. Papaphilippou, “Emittance reduction with variable bending magnet strengths: Analytical optics considerations,” 2018.

Andrea Passarelli

Education

2014 - Present	**Ph.D. student at the Institute for Theory of Electromagnetic Fields (TEMF)**, *Technical University Darmstadt (Darmstadt, Germany).* **Thesis title:** *Characterization of impedance and wakefields of accelerator devices in the short bunch limit and beam dynamics effects for the CLIC Damping Rings.*
2011- 2014	**Master's degree in Electronic Engineering**, *University of Naples Federico II (Naples, Italy).* **Thesis title:** *Simulation and experimental studies on electron cloud effects in particle accelerators.*
2004 - 2011	**Bachelor's degree in Electronic Engineering**, *University of Naples Federico II (Naples, Italy).* **Thesis title:** *”Progetto di un quadrupolo a radiofrequenza: simulazioni elettromagnetiche e studio della sorgente”(Design of a Radio Frequency Quadrupole: Electromagnetic Simulations and Study of the Source)*

Experience

Oct 2018 - Present	**Research Fellow at Physics Department - University of Naples Federico II**, *(Naples, Italy).*
Oct 2017 - May 2018	**Cooperation Associates with INFN-Sezione di Napoli at CERN**, *(Geneva, Switzerland).*
Oct 2014 - Sept 2017	**Doctoral student at CERN**, *(Geneva, Switzerland).* **Thesis directors:** *Prof. Dr. rer. nat. Oliver Boine-Frankenheim and Dr. Hannes Bartosik.*
Jul 2013 - Sept 2014	**Technical Student at CERN for Master thesis project**, *(Geneva, Switzerland).*
Jun 2010 - Dec 2011	**Intern Student at INFN-Sezione di Napoli**, (Naples, Italy).

Computer skills

Programs and Languages	**Python, Matlab, LabView, C++, CST - Microwave & Particle Studio**

Languages

English: Fluent

Italian: Mothertongue

French: Basic Knowledge

Publications

- A. Passarelli, H. Bartosik, G. Rumolo, V. G. Vaccaro, M. R. Masullo, C. Koral, G. P. Papari, A. Andreone, and O. Boine-Frankenheim, “Novel measurement technique for the electromagnetic characterization of coating materials in the sub-thz frequency range,” Phys. Rev. Accel. Beams, vol. 21, p. 103101, Oct 2018

- K. Li, H. Bartosik, G. Iadarola, A. Oeftiger, A. Passarelli, A. Romano, G. Rumolo, M. Schenk, and S. Hegglin, “Code development for collective effects,” in ICFA Advanced Beam Dynamics Workshop on High-Intensity and High-Brightness Hadron Beams (HB2016), 2016

- N. Biancacci, ..., A. Passarelli, et al., “Impedance Measurements and Simulations on the TCTP and TDI LHC Collimators,” in 7th International Particle Accelerator Conference, no. CERN-ACC-2016- 310, p. MOPOR010. 4 p, 2016

- B. Salvant, ..., A. Passarelli, et al., “Expected Impact of Hardware Changes on Impedance and Beam-induced Heating during Run 2,” in Chamonix 2014: LHC Performance Workshop, 2015

- A. Danisi, C. Zannini, A. Passarelli, A. Masi, R. Losito, and B. Salvant, “FEM Analysis of Beam-coupling Impedance and RF Contacts Criticality on the LHC UA9 Piezo Goniometer,” in 5th International Particle Accelerator Conference, no. CERN-ACC-2014-0192, p. 4 p, Jun 2014

Invited Talks

- “Electromagnetic characterization of coating materials in the sub-THz frequency range: a new methodology.” 104th Congresso Nazionale della Societ Italiana di Fisica, 17-21 September 2018 organized by Universit ́a della Calabria in Arcavacata di Rende, Italy

- “High-frequency impedance measurements of coated waveguides.” Asian Linear Collider Workshop, 28 May to 1 June 2018 in Fukuoka, Japan

- “High-frequency impedance measurements of coated wave-guides.” International Workshop on Future Linear Colliders, 23-27 October 2017 in Strasbourg, France

- “Instability studies in the CLIC damping rings including radiation damping.” Second Topical Workshop on Instabilities, Impedance and Collective Effects will, 8-10 February 2016 organized by John Adams Institute and Diamond Light Source in Abingdon, UK